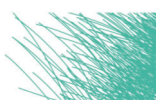
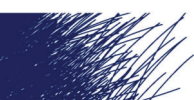


Fusing multiple signals of an electromagnetic induction sensor to characterize contrasting soil layers and buried features



Timothy Saey



Promoter: Prof. dr. ir. Marc Van Meirvenne
Department of Soil Management,
Faculty of Bioscience Engineering, Ghent University

Dean: Prof. dr. ir. Guido Van Huylenbroeck

Rector: Prof. dr. Paul Van Cauwenberge

Timothy Saey

FUSING MULTIPLE SIGNALS OF AN ELECTROMAGNETIC
INDUCTION SENSOR TO CHARACTERIZE CONTRASTING
SOIL LAYERS AND BURIED FEATURES

Thesis submitted in the fulfilment of the requirements for the degree of Doctor (PhD) in
Applied Biological Sciences: Land and Forestry Management

Dutch translation of the title:

DE FUSIE VAN MEERDERE SIGNALLEN VAN EEN
ELEKTROMAGNETISCHE INDUCTIE SENSOR VOOR DE
KARAKTERISERING VAN CONTRASTERENDE BODEMLAGEN
EN BEGRAVEN OBJECTEN

Illustrations of the cover:

Multi-signal integration provides a 3D-picture of a tidal channel in the coastal plain.

Citation:

Saey, T., 2011. Fusing multiple signals of an electromagnetic induction sensor to characterize contrasting soil layers and buried features. PhD thesis, Ghent University.

ISBN-number: 9789059894266

The author and the promoter give the authorization to consult and the copy parts of this work for personal use only. Every other use is subject to the copyright laws. Permission to reproduce any material contained in the work should be obtained from the author.

Dankwoord

Met bijzonder veel tevredenheid blik ik terug op mijn tijd op de vak- en onderzoeksgroep. Ik wil mijn promotor, Prof. Marc Van Meirvenne, hartelijk bedanken voor de kans die hij me gaf om in 2006 te komen werken op zijn FWO-onderzoeksproject. Vanaf het begin van het project heeft hij me steeds aangemoedigd om mijn nieuwe ideeën te ontwikkelen, te staven en de gevonden opvattingen te publiceren. Hij fungeerde meermaals als katalysator die ik en mijn collega's David en Hans nodig hadden om nieuwe inzichten te ontwikkelen en uit te bouwen. Daarenboven was hij steeds bereid om zijn ervaring en kennis te delen om ons, zonder al te veel omwegen, naar ons einddoel te leiden.

Daarbij mag ik ook mijn ORBit-collega's, waar ik 3.5 jaar intensief heb mee samengewerkt, niet uit het oog verliezen. Bedankt David en ook Philippe voor de vele overlegmomenten en de hulp bij het uitdenken van de experimenten; Hans en Valentijn voor de technische ondersteuning bij de uitvoering (sorry dat ik soms zo onhandig was) en de toffe momenten op het terrein; en Liesbet, Udaya, Eef, Islam, Meklit, Sam, Jo en Fun voor de steeds interessante en leuke sfeer tijdens onderzoeksgroep-activiteiten.

Ook mag ik de andere collega's van de vakgroep niet vergeten voor de aangename momenten op de vakgroep: Patrick, Matthieu, Maarten D.C., Maarten V., Jan V., Jeroen, Luc en Steven om hun interesse in allerlei sportdisciplines en -activiteiten met me te delen en voor de legendarische uitstapjes daarbuiten; en Georges, Donald, Wim, Stefaan, Ben, Annemie, Sofie, Tina, Thérèse, Jan R., Trees, Rik, Koen, Pieter, Yves, Nele, Liesbet, Sarah, Joost, Anita, David en Bram om ervoor te zorgen dat ik steeds graag naar mijn werkomgeving terugkwam! Verder wil ik ook al diegenen bedanken waar ik op de één of andere manier heb mogen mee samenwerken, onderzoeksmatig of commercieel: Jean als co-promotor van het project, Alexander en Harry in Hof ter Hille; Marc en Franky in Geluveld; Pieter, Johan, Wim en Filip in Rieme, Lieven,... De landbouwers Eddy Hooghe en Carlos de Cuyper verdienen een bijzondere vermelding, niet alleen waren zij steeds bereid hun velden ter beschikking te stellen voor prospectie, zij toonden zich steeds bereidwillig om mee te helpen aan het welslagen van het onderzoek. Ook alle andere landbouwers wiens velden ik heb mogen prospecteren: een dikke merci!

Voor de nodige ontspanning naast het onderzoek kon ik altijd rekenen op mijn vrienden in verschillende sportclubs, en in het bijzonder die van het SMO-triatlonteam. Door hen ben ik gebeten door de triatlonmicrobe als een gezonde uitlaatklep naast de werkactiviteiten! Ook de ex-studiegenoten en vrienden wil ik bedanken voor de leuke uitstapjes en gezellige avonden!

aDeDe wil ik bedanken voor de opportuniteit om mijzelf verder te ontplooiën in de geofysische detectiewereld, en voor de toffe en aanstekelijke samenwerking met mijn nieuwe collega's.

Ik prijs me zeer gelukkig met mijn familie, die altijd voor me klaarstonden en me door dik en dun gesteund hebben: Ma en Pa, bedankt voor de jarenlange zorgen, het gezelschap en de bergen eten die ik verslonden heb en Meme, Pepe en mijn broers die altijd aan mijn zijde stonden en de nodige afleiding bezorgden. Mijn lieve Ellen verdient een speciale vermelding: zij is diegene die me elke dag opnieuw gelukkig maakt. Dank om er steeds voor mij te zijn!

Table of contents

DANKWOORD	V
TABLE OF CONTENTS	VII
SAMENVATTING	10
SUMMARY	13
LIST OF FIGURES	16
LIST OF TABLES	20
CHAPTER 1 INTRODUCTION	
1.1 OVERVIEW	22
1.2 RESEARCH OBJECTIVES	25
1.3 STRUCTURE OF THE THESIS	27
CHAPTER 2 MATERIALS AND METHODS: PROXIMAL SOIL SENSING	
2.1 INTRODUCTION	29
2.2 GROUND PENETRATING RADAR, MAGNETOMETRY AND ELECTRICAL RESISTANCE	
2.2.1 GROUND PENETRATING RADAR	30
2.2.2 MAGNETOMETRY	31
2.2.3 ELECTRICAL RESISTANCE	32
2.3 ELECTROMAGNETIC INDUCTION	
2.3.1 PRINCIPLE	34
2.3.2 INSTRUMENT OUTPUT TO CONDUCTIVITY	36
2.3.3 PENETRATION DEPTH	37
2.3.4 ELECTRICAL CONDUCTIVITY	38
2.3.5 INSTRUMENTS	40
2.3.6 CUMULATIVE DEPTH RESPONSE	41
2.3.7 MOBILE MEASUREMENT EQUIPMENT	42
2.4 INTERPOLATION	43
2.5 GEOLOGY AND GEOMORPHOLOGY OF EAST- AND WEST-FLANDERS	47
CHAPTER 3 A PEDOTRANSFER FUNCTION TO EVALUATE THE SOIL PROFILE TEXTURAL HETEROGENEITY	
3.1 ABSTRACT	50
3.2 INTRODUCTION	51
3.3 SOIL TEXTURE DATABASE	52
3.4 SELECTION OF SOIL PROFILES WITH “PSEUDO-HOMOGENEOUS” TEXTURAL COMPOSITION	54
3.5 ECA MEASUREMENTS	55
3.6 PEDOTRANSFER FUNCTION	56

Table of contents

3.7	IDENTIFYING THE SOIL PROFILE TEXTURAL HETEROGENEITY WITH REFERENCE ECA_v VALUES	59
3.8	A REGIONAL ECA-REF MAP	61
3.9	CONCLUSIONS	63
CHAPTER 4	RECONSTRUCTING THE PALEOTOPOGRAPHY BENEATH THE LOESS COVER	
4.1	ABSTRACT	64
4.2	INTRODUCTION	65
4.3	GEOLOGY	66
4.4	STUDY SITE	67
4.5	ECA MAPPING	68
4.6	DEPTH OBSERVATIONS	70
4.7	FITTING	71
4.8	PALEOTOPOGRAPHY BENEATH THE LOESS COVER	73
4.9	CONCLUSIONS	76
CHAPTER 5	COMPARING THE EM38DD AND DUALEM-21S SENSORS FOR DEPTH-TO-CLAY MAPPING	
5.1	ABSTRACT	77
5.2	INTRODUCTION	78
5.3	STUDY SITE	79
5.4	ECA SURVEY	79
5.5	EM38DD	80
5.6	DUALEM-21S	83
5.7	RECONSTRUCTING THE PALEOTOPOGRAPHY	84
5.8	CONCLUSIONS	85
CHAPTER 6	MAPPING DEPTH-TO-CLAY USING FITTED MULTIPLE DEPTH RESPONSE CURVES	
6.1	ABSTRACT	86
6.2	INTRODUCTION	87
6.3	STUDY SITE	88
6.4	ECA SURVEY	89
6.5	DEPTH OBSERVATIONS	91
6.6	EC-PROBE MEASUREMENTS	91
6.7	FITTING DEPTH RESPONSE CURVES	92
6.8	DEPTH MODELLING	95
6.9	RESISTIVITY IMAGING	96
6.10	PALEOLANDSCAPE BENEATH THE LOESS COVER	98
6.11	CONCLUSIONS	100
CHAPTER 7	RECONSTRUCTING A HOLOCENE TIDAL CHANNEL IN A POLDER AREA	
7.1	ABSTRACT	101
7.2	INTRODUCTION	102

Table of contents

7.3	REGIONAL SETTING	103
7.4	ECA SURVEY	104
7.5	DEPTH OBSERVATIONS	111
7.6	PUNCTUAL ECA-MEASUREMENTS	111
7.7	DEPTH MODELLING	112
7.8	VALIDATION	113
7.9	RECONSTRUCTION OF THE TIDAL CHANNEL	114
7.10	CONCLUSIONS	115
CHAPTER 8	EC-DEPTH MODELLING WITH A MULTI-SIGNAL EMI SENSOR TO ACCENTUATE ARCHAEOLOGICAL FEATURES	
8.1	ABSTRACT	116
8.2	INTRODUCTION	117
8.3	SITE DESCRIPTION	118
8.4	HISTORICAL AND ARCHAEOLOGICAL SETTING	119
8.5	ECA SURVEY	120
8.6	EC-DEPTH MODELLING	122
8.7	VALIDATION	124
8.8	CONCLUSIONS	127
CHAPTER 9	COMBINING MULTIPLE SIGNALS TO PROSPECT LAND FOR METAL OBJECTS	
9.1	ABSTRACT	128
9.2	INTRODUCTION	130
9.3	METAL DETECTING	131
9.4	CALIBRATION AND VALIDATION SITES	132
9.5	ECA SURVEY	134
9.6	TRANSECTS	135
9.7	VALIDATION	137
9.8	CONCLUSIONS	142
CHAPTER 10	GENERAL CONCLUSIONS AND FUTURE RESEARCH	
10.1	GENERAL CONCLUSIONS	143
10.2	FUTURE RESEARCH	147
REFERENCES		149
CURRICULUM VITAE		160

Samenvatting

Conventionele technieken zoals boringen of opgravingen zijn dikwijls zeer arbeidsintensief en niet altijd geschikt voor het in kaart brengen van de verticale bodemheterogeniteit en voor het lokaliseren van begraven objecten of sporen. Daarenboven kan de continuïteit van deze fenomenen onmogelijk in kaart gebracht worden. Als alternatief werden proximale bodemsensoren ontwikkeld om vlug en efficiënt informatie te verkrijgen over de bovenste 2 m van de bodem. De toepassingen van deze bodemsensoren verschillen al naargelang de geofysische methode waarop ze gebaseerd zijn. In deze studie werden twee proximale bodemsensoren op basis van elektromagnetische inductie (EMI) onderzocht op hun potentieel om niet-invasief contrasterende lagen in kaart te brengen en begraven objecten en sporen te lokaliseren: de EM38DD en DUALEM-21S. Deze twee EMI sensoren meten zowel de geleidbaarheid als de magnetische eigenschappen van de bodem. Laagfrequente elektromagnetische golven worden uitgestuurd vanuit een zendspoel en ontvangen door een ontvangspoel. Voor elke spoelconfiguratie van een EMI sensor wordt de meetdiepte bepaald door zowel de afstand tussen zend- en ontvangspoel als door de oriëntatie van de ontvangspoel ten opzichte van de zendspoel. De twee gebruikte instrumenten bestaan beiden uit verschillende spoelconfiguraties en zijn daardoor dus in staat om simultaan verschillende bodemvolumes op te meten. De EM38DD sensor meet simultaan in twee verschillende spoelconfiguraties, de DUALEM-21S in vier.

In een eerste fase werd de schijnbare elektrische geleidbaarheid (EGs) van de EM38DD gerelateerd aan verschillende bodemtextuur-fracties. Door onderzoek op een bepaald aantal “pseudo-homogene” bodemprofielen werd aangetoond dat enkel de fijnste textuurfractie (klei) ($0-2\ \mu\text{m}$) kon gecorreleerd worden met de EGs metingen. Uiteindelijk kon met de ontwikkelde pedotransferfunctie een referentie EGs kaart van de toplaag opgesteld worden voor Oost-Vlaanderen. Door de verhouding van de waarde op de referentie EGs kaart en de geobserveerde EGs (tot een diepte van ongeveer 1.5 m), kon de heterogeniteit van elk profiel ingeschat worden. Ratio's dichtbij 1 indiceren quasi-homogene profielen; ratio's groter dan 1 impliceren de aanwezigheid van conductief materiaal dieper in de ondergrond en vice versa.

In een tweede fase werd de combinatie van de verschillende EGs signalen onderzocht om de diepte tussen contrasterende lagen of lagen met sterk verschillende geleidbaarheid in kaart te brengen. Daartoe werd in de Belgische leemstreek de diepte tot het Tertiair substraat onder het loesspakket gerelateerd aan de EGs gebruik makende van een theoretische diepterresponscurve. Met die relatie werden de gedetailleerde EGs metingen van het studiegebied op een niet-lineaire manier geconverteerd naar de dieptes van het Tertiair substraat. Met de hoogte van het huidig oppervlak werd de paleotopografie of de hoogte van

het Tertiair oppervlak berekend. Op dit oppervlak werden stroomlijnen gemodelleerd, die als vroegere erosiepatronen geïnterpreteerd kunnen worden. Deze methodologie werd vervolgens vergeleken met de combinatie van de vier simultane EGs metingen met de DUALEM-21S om de diepte tot het Tertiair substraat te modelleren. Hierbij werden theoretische benaderingen gebruikt voor de diepteresponscurves van de verschillende spoelconfiguraties. Uiteindelijk konden de dieptes even nauwkeurig ingeschat worden als wanneer calibratieboringen gebruikt werden.

Als alternatief van de theoretische diepteresponsfuncties werd een procedure opgesteld om deze empirisch te benaderen. De diepteresponscurves werden voor zowel de verticale als loodrechte spoelconfiguraties opgesteld door het simultaan fitten van de EGs-data aan de dieptes van de calibratieboringen. Uiteindelijk werd de dieptemodellering gevalideerd met behulp van elektrische resistiviteitsmetingen. Met deze methode kon het paleolandschap van een gebied van 39 ha gemodelleerd en driedimensioneel gevisualiseerd worden.

Wanneer bodemmateriaal met lage geleidbaarheid zich bevindt boven een hoog-conductief substraat, kon de diepte tussen de lagen heel nauwkeurig gemodelleerd worden. De omgekeerde situatie manifesteert zich echter in de kustvlakte: een kleiig, conductief pakket is daar gelokaliseerd bovenop zandig, resistief materiaal. Daarin werden in de loop der tijd verschillende getijdekanalen ingesneden, zo goed als onzichtbaar aan het oppervlak omdat deze dichtgeslibd zijn met kleiig materiaal. In een derde fase werd daarom aangetoond dat de diepte tussen de kleiige deklaag en het grove zand of tussen de klei in de geul en het zand even nauwkeurig gemodelleerd kon worden met behulp van enkele rechtstreekse conductiviteitsmetingen en een beperkt aantal boringen.

Op hetzelfde studiegebied werd een procedure vooropgesteld om archeologische anomalieën te versterken door combinatie van de simultane EGs metingen. De vier metingen werden gecombineerd om de conductiviteit te modelleren tussen vooraf gedefinieerde dieptes, met een versterking van de vage anomalieën veroorzaakt door archeologische sporen tot gevolg. Het contrast tussen de vage signaturen en de 'lege' achtergrond kon zo worden vergroot, wat de aanduiding en interpretatie van de sporen vergemakkelijkt. Hierdoor kunnen archeologische opgravingen gericht worden uitgevoerd, wat een aanzienlijke daling van de kostprijs met zich meebrengt. Daarenboven kan de continuïteit van de sporen ingeschat worden, wat de interpretatie vereenvoudigt.

In een vijfde onderzoeksfase werden verschillende EGs metingen gecombineerd om metalen objecten in een WO I slagveld aan te duiden, vermits elke spoelconfiguratie een sterke, afwijkende respons vertoont boven metalen objecten in de ondergrond. De signatuur van de anomalieën verschilt naargelang de spoelafstand en -oriëntatie. Om een eenduidig signaal te verkrijgen boven de begraven metalen objecten werden de metingen gefilterd en gecombineerd. Vooreerst werd de graduele trend afgetrokken van de ruwe EGs metingen om

enkel de lokale verstoringen zichtbaar te maken. De specifieke combinatie van de vier metingen versterkte het contrast tussen anomalieën en de achtergrond aanzienlijk. Zowel de diepte als de massa van de begraven objecten blijken de gecombineerde waarde substantieel te beïnvloeden. Finaal werd een eenduidige respons van de metalen objecten verkregen tot een diepte van ongeveer 1 m. Opgravingsresultaten bevestigden dat de procedure bruikbaar was voor het lokaliseren van metalen objecten, zoals niet-geëxplodeerde obussen, in de bovenste meter van de bodem.

Om te besluiten bewees dit onderzoek het potentieel van multi-signaal EMI sensoren. De fusie van de verschillende simultane signalen vertoonde een duidelijke meerwaarde ten opzichte van de som van elk signaal afzonderlijk om contrasterende lagen in kaart te brengen en begraven objecten en sporen aan te duiden. Dit omwille van de gelijktijdige scans op verschillende dieptes, gevoeligheid voor verschillen in kleigehalte en voor metalen objecten en mogelijkheden tot combinatie van de complementaire en aanvullende metingen.

Summary

Quantification of the small-scale vertical soil heterogeneity and the location of buried features is very labour-intensive using the conventional techniques of soil augering and excavation. Apart from this, the continuity of these phenomena cannot be mapped accurately. Proximal soil sensors were developed to obtain quick and continuous estimations of the soil constitution nearby the surface (< 2 m). The application of these instruments differs according to the geophysical method on which they are based.

In this study, two proximal soil sensing instruments were investigated on their potential to map contrasting soil layers and to locate buried features non-invasively: the EM38DD and DUALEM-21S. Both electromagnetic induction sensors measure the conductivity and magnetic properties of the soil. Low-frequency electromagnetic waves are transmitted from a first coil and received by a second coil. Despite the fixed frequency, both the distance in-between and the orientation of transmitting and receiving coils determine the depth of investigation. Both instruments consist of multiple coils, measuring simultaneously within different depth intervals. The EM38DD sensor measures simultaneously in two coil configurations, the DUALEM-21S in four. The goal of this research was to evaluate the potency of fusing the multiple signals to map contrasting soil layers and to locate buried features.

In a first phase, the apparent electrical conductivity (ECa) of the EM38DD was statistically compared with the whole range of soil textural fractions. From investigation on a substantial amount of “pseudo-homogeneous” profiles, only the finest textural fraction ($0-2\ \mu\text{m}$) proved to influence the ECa substantially. Pedotransferfunctions were established linking the clay fraction to the ECa. A reference ECa map was obtained as a direct conversion from the topsoil clay content. The ratio of the reference (topsoil) ECa map on the observed ECa (until a depth of approximately 1.5 m), provides a raw quantification of the soil profile heterogeneity. If this ratio is near to one, the profile is quasi-homogeneous; a ratio exceeding one indicates the presence of more conductive material deeper in the soil profile, and *vice versa*.

In a second phase, multiple ECa signals were combined to quantify the depth between contrasting layers (with different conductivity). On a study site in the Belgian loess belt, the depth of the Tertiary substrate beneath the loess cover was calibrated to the ECa using a theoretical depth response function. Given this relationship, the ECa map was non-linearly converted in a depth-to-clay map of the entire study site. Given the elevation of the current surface, the paleotopography or the elevation of the Tertiary surface was reconstructed. On this surface, flow lines were modelled, representing past erosion processes. This methodology was compared with the combination of the four simultaneous ECa measurements from the

DUALEM-21S to model the depth-to-clay at the same study site non-invasively. Assuming the depth responses of the four different coil configurations described by theoretical approximations of the Maxwell's equations, the depths were accurately modelled without calibration augerings.

As an alternative for these theoretical response functions, a procedure was proposed to establish empirical depth response curves for different coil configurations. The depth response curves were fitted both for the vertical and perpendicular coil configurations, employing both calibration observations and direct conductivity measurements of both layers. The predictions were validated with geo-electrical imaging. Finally, the paleolandscape of an area of 39 ha in the Belgian loess belt was modelled and visualized three-dimensionally.

With low-conductive material situated above high-conductive material, the depth in-between the contrasting layers could be accurately modelled. In the coastal plain, a clayey conductive layer was located above sandy, resistive material. Different tidal channels manifest into the coastal plain, invisible at the surface because filled with sedimented clayey material. In a third phase, the depth between the clayey pack and coarse sand or between the clay in the tidal channel and the sand was accurately modelled at a study site in the Belgian coastal plain. The current of a tidal channel could be visualized three-dimensionally.

On the same study site, a procedure was proposed to highlight different archaeological anomalies based on combinations of the simultaneous ECa measurements with the DUALEM-21S instrument. The four measurements were combined to model the conductivities within specific depth intervals, showing a more distinct variability across archaeological features. Vague archaeological anomalies could be amplified by applying the developed methodology, guiding excavation activities more efficiently, hereby reducing the labour efforts and costs.

In a fifth phase, the combination of multiple ECa measurements was investigated to delineate metal objects on a WW I battlefield. Each coil configuration proved to respond strongly on metal objects in the soil. However, the magnitude and sign of the metal anomalies differed according to the instruments coil distance and orientation. The four simultaneous measurements were subtracted with their gradual trend to obtain the local anomalies. The combination amplified the signal response to metal, influenced by both depth and mass of the buried objects. Finally, a clear response for buried metal was obtained to a depth of about 1.2 m. Excavation results confirmed the procedure appropriate to locate metal objects, like unexploded WW I shells, in the top 1.2 m of a soil.

To conclude, this research showed the potential of fusing multiple simultaneous signals from the coil configurations of the electromagnetic induction instruments for mapping contrasting soil layers and locating buried features. Multi-coil electromagnetic induction sensors prove to offer more information than other sensors due to their investigation at different depths,

sensitivity for small variations in clay content and for metal objects and possibilities for combining the separate measurements. The integration of the multiple signals provides a large added value compared to the single signals.

List of figures

Fig. 1.1.	Schematic overview of the thesis.	28
Fig. 2.1.	Basic principles of Magnetometry (left), GPR (middle) and Electrical Resistivity (ER) (right) (Simpson, 2009).	31
Fig. 2.2.	EC-probe with indication of its components: current electrodes ((1) and (4)), measuring electrodes ((2) and (3)), power source (6) and resistivity meter (7).	33
Fig. 2.3.	Basic elements of an electromagnetic wave with electric (E) and magnetic (H) components (WHO, 1998).	34
Fig. 2.4.	Basic principle of electromagnetic induction sensing.	35
Fig. 2.5.	Amplitude of the primary and secondary field, oscillating in time.	36
Fig. 2.6.	Transmitter and receiver dipole orientations and coil spacings of the EM38DD (a) and DUALEM-21S (b).	40
Fig. 2.7.	Cumulative response as a function of the depth z for the EM38DD and DUALEM-21S instruments.	41
Fig. 2.8.	EM38DD (a) and Mobile ECa _v -measurement equipment (b); 1: Sled with EM38DD, 2: All Terrain Vehicle, 3: Trimble AgGPS332 and field computer, 4: GPS antenna, 5: Lightbar Guidance System.	42
Fig. 2.9.	An experimental variogram (points) fitted by a theoretical variogram model (line)	45
Fig. 2.10.	Localization of the Lovendegem, Koksijde, Geluveld and Heestert study sites in the provinces of West- and East-Flanders and the agricultural regions of Flanders (coordinates are according to the Belgian metric Lambert 72 projection).	49
Fig. 3.1.	Localization of the study area in Belgium.	52
Fig. 3.2.	Soil texture map of East-Flanders classified according to the USDA soil textural triangle (Van Meirvenne and Van Cleemput, 2005) (the city of Ghent was blanked).	53
Fig. 3.3.	Localization of the 88 soil profiles with 'pseudo-homogeneous' textural composition and 17 soil profiles with heterogeneous textural composition inside East-Flanders.	54
Fig. 3.4.	The 88 measurements of ECa _v of the 'pseudo-homogeneous' soil profiles and the profile weighted clay contents, $Fr_{0-2,w}$, with the fitted regression $ECa_v = 16.2 + 1.314 \cdot Fr_{0-2,w}$ (full line) and its 95 % confidence interval (dashed curves).	59

Fig. 3.5.	$Fr_{0.2}$ as a function of the depth below the surface for the 17 soil profiles with heterogeneous textural composition classified on the base of their $ECa_{obs} \cdot (ECa_{ref})^{-1}$ ratio: 5 profiles have a ratio larger than 2 (a) 6 profiles have a ratio between 1 and 2 (b) and 6 profiles have a ratio smaller than 1.	61
Fig. 3.6.	ECa_{ref} of the province of East-Flanders, Belgium.	62
Fig. 4.1.	Localization of the study site in the Belgian loess belt.	67
Fig. 4.2.	ECa_{v_field1} as a function of ECa_{v_field2} (72 data points at the boundary of both fields).	69
Fig. 4.3.	Map of interpolated ECa_v ($mS\ m^{-1}$) with transects ABCD and EF.	69
Fig. 4.4.	ECa_v and ECa_h measurements and thickness of the loess along the 225 m transect ABCD (a) and the build-up of the three layers encountered along this transect (b).	71
Fig. 4.5.	z_{clay} as a function of ECa_v along study transects ABCD and EF with fitted McNeill-curve.	73
Fig. 4.6.	Validation of predicted depth to the Tertiary clay (z_{clay}^*) using 24 observed depths (z_{clay}).	74
Fig. 4.7.	Current soil surface (a), paleotopography beneath the loess cover represented as elevation above sea level with indications of simulated flow lines (b), and paleotopography represented as depth below soil surface (c).	75
Fig. 5.1.	Interpolated ECa_v ($mS\ m^{-1}$) with localization of calibration points on transects ABCD and EF (a) and interpolated ECa_h ($mS\ m^{-1}$) with localization of validation points (b).	81
Fig. 5.2.	Scatterplot of predicted interface depth (z_{clay}^*) versus the observed depth (z_{clay}) for both EMI-procedures ($n = 24$).	83
Fig. 5.3.	Elevation of the current soil surface (a), z_{clay}^* predicted by the EM38DD procedure (b), and z_{clay}^* predicted by the DUALEM-21S procedure (c).	85
Fig. 6.1.	Localization of the study area in the Belgian loess belt and topographic map with indication of the boundaries (coordinates are according to the Belgian metric Lambert 72 projection).	88
Fig. 6.2.	Kriged apparent electrical conductivity map (converted to a reference temperature of 25°C) in the 1 m – vertical coil configuration ($ECa_{v,1}$) with localization of transects AB, BC, DEFG and HI and the 30 m by 30 m grid. The border of the test area is denoted with a black frame.	90
Fig. 6.3.	Fitted cumulative depth response curves (and expressed as depth-to-clay (z_{clay}) – apparent electrical conductivity (ECa) relationship) (a) for the perpendicular coil configurations and (b) the vertical coil configurations of the DUALEM-21S, each with their corresponding z_{clay} - ECa observations.	95

Fig. 6.4.	2D-inverted transects with 1D-inverted depths of the interface between the loess and clay (black line) and the corresponding modelled conductivities of the loess (EC_{loess}) and clay (EC_{clay}) for transects AB and BC.	97
Fig. 6.5.	Scatterplot of the predicted clay depth (z_{clay}^*) versus the observed depth (z_{clay}) with validation indices.	98
Fig. 6.6.	(a) The elevation of the current surface with modelled flow patterns and (b) the elevation of the paleolandscape before the deposition of the loess cover with modelled flow patterns and (c) 3D-surface of the modelled depth-to-clay (z_{clay}^*).	99
Fig. 7.1.	Localization of the study site on the topographic map.	103
Fig. 7.2.	Measured apparent electrical conductivity map in the 1.1 m - perpendicular coil configuration ($E_{Ca_{p,1.1}}$) (a), in the 2.1 m - perpendicular coil configuration ($E_{Ca_{p,2.1}}$) (b), in the 1 m - vertical coil configuration ($E_{Ca_{v,1}}$) (c) and in the 2 m - vertical coil configuration ($E_{Ca_{v,2}}$) (d), with localization of the study site 1 (black box right) and study site 2 (black box left).	108
Fig. 7.3.	Variograms of the apparent electrical conductivity in the 1.1 m - perpendicular coil configuration (a), in the 2.1 m - perpendicular coil configuration (b), in the 1 m - vertical coil configuration (c) and in the 2 m - vertical coil configuration (d).	110
Fig. 7.4.	Interpolated apparent electrical conductivity (E_{Ca}) map in the 1.1 m - perpendicular coil configuration with localization of transect AB (a), in the 2.1 m - perpendicular coil configuration with 20 points in a 50 by 50 m grid (b), in the 1 m - vertical coil configuration with localization of transect CD (c) and in the 2 m - vertical coil configuration (d) (all in $mS\ m^{-1}$).	110
Fig. 7.5.	Build-up of the three-layered soil along transect AB.	111
Fig. 7.6.	Scatterplot of the predicted interface depth (z_{sand}^*) vs. the observed depth (z_{sand}).	113
Fig. 7.7.	The elevation of the current surface (a) and the elevation of the tidal channel (b).	114
Fig. 8.1.	Topographic map with indication of the boundaries of study and excavation sites (see arrow).	118
Fig. 8.2.	Measured apparent electrical conductivity map (converted to a reference temperature of 25°C) in the 1.1 m - perpendicular coil configuration ($E_{Ca_{p,1.1}}$) (a), in the 2.1 m - perpendicular coil configuration ($E_{Ca_{p,2.1}}$) (b), in the 1 m - vertical coil configuration ($E_{Ca_{v,1}}$) (c) and in the 2 m - vertical coil configuration ($E_{Ca_{v,2}}$) (d), with localization of the excavated site (white line).	121

List of Figures

Fig. 8.3.	Measured apparent electrical conductivity map in the 1 m - vertical coil configuration ($E_{Ca_{v,1}}$) with indication of the excavated archaeological features.	122
Fig. 8.4.	Modelled conductivity map between 0 and 0.5 m (EC^*_1) (a), between 0.5 and 1.0 m (EC^*_2) (b) and deeper than 1.0 m (EC^*_3).	124
Fig. 8.5.	Measured apparent electrical conductivities (E_{Ca} 's) and modelled conductivity between 0.5 and 1.0 m (EC^*_2) along transects AB and CD.	125
Fig. 8.6.	Rasterized map of the excavated archaeological features (zone 1: features absent; zone 2: features present).	126
Fig. 9.1.	Localization of the Lovendegem and Geluveld study sites in Belgium.	132
Fig. 9.2.	Situation of the metal bars with different m buried at different z in the soil.	133
Fig. 9.3.	$\Delta E_{Ca_{p,1,1}}$ with indication of m and z of the metal bars in the soil (a), $\Delta E_{Ca_{p,2,1}}$ (b), $\Delta E_{Ca_{v,1}}$ (c) and $\Delta E_{Ca_{v,2}}$ with delineation of transects AB and DC (d) at the Lovendegem calibration site (right of the 2 transects, metal bars were buried in a vertical position, not relevant for this research).	134
Fig. 9.4.	ΔE_{Ca} values along transect AB (a) and along transect DC (b).	136
Fig. 9.5.	FEMP values along transect AB (a) and along transect DC (b).	136
Fig. 9.6.	m as a function of the FEMP of the metal bars along transect AB (a) and z as a function of $\ln(\text{FEMP})$ along transect DC (b).	137
Fig. 9.7.	$E_{Ca_{p,1,1}}$ (a), $E_{Ca_{p,2,1}}$ (b), $E_{Ca_{v,1}}$ (c) and $E_{Ca_{v,2}}$ (d) measurements with the DUALEM-21S instrument at the Geluveld study site.	138
Fig. 9.8.	FEMP map at the Geluveld study site with indication of a detail window.	139
Fig. 9.9.	m of the metal objects at the detail window on Fig. 8.8 assuming $z = 0.4$ m (a) and z assuming $m = 11.4$ kg (b).	141

List of Tables

Table 2.1.	Indicative resistivity and conductivity values of different soil types (Bevan, 1983).	40
Table 3.1.	Descriptive statistics of profile weighted textural fractions ($Fr_{-,w}$) determined with the vertical response curve (Eq. 3.1) for the 88 soil profiles with ‘pseudo-homogeneous’ textural composition and the recently observed ECa's and SOM (m : mean, s^2 : variance).	56
Table 3.2.	Pearson correlation coefficients between the two ECa's and the profile weighted textural fractions ($Fr_{-,w}$) and SOM content.	57
Table 3.3.	Fitting parameters the regression model for ECa_v (Eq. 3.4) obtained with the stepwise multiple linear regression analysis (s : standard error; t : Student's-t-test of significance, p : probability level).	58
Table 3.4	Fitting parameters the regression model for ECa_h (Eq. 3.5) obtained by the stepwise multiple linear regression analysis (s : standard error; t : Student's-t-test of significance, p : probability level).	58
Table 3.5	Comparison between ECa-obs and ECa-ref and their ratio of 17 soil profiles with heterogeneous textural composition.	60
Table 4.1	Average textural composition of the Quaternary loess and Tertiary substrate based on samples taken along transect ABCD (n : number of samples, m : mean, s : standard deviation).	68
Table 4.2	Descriptive statistics (m : mean, min: minimum, max: maximum, s : standard deviation) of ECa_v , and ECa_h for the two fields (field 1 contained 5509 measurement points, field 2 contained 1814 measurement points).	68
Table 4.3	Parameters of the Gaussian variogram model for ECa_v , Z , $Z - z_{clay}^*$ and z_{clay}^* (C_0 : nugget variance; C_1 : sill and a : range).	70
Table 5.1	Descriptive statistics of ECa for the different coil configurations of the EMI sensors EM38DD and DUALEM-21S (n : number of observations, m : mean, s^2 : variance and CV: coefficient of variation).	80
Table 5.2	Variogram parameters for the variables ECa_v ($mS\ m^{-1}$), ECa_h ($mS\ m^{-1}$), Z (m), z_{clay}^* (m) modelled with the EM38DD measurements together with 56 calibration observations and z_{clay}^* (m) modelled with the DUALEM-21S measurements (C_0 : nugget variance; $C_0 + C_1$: sill and a : range of Gaussian variogram models).	80

List of Tables

Table 5.3	Descriptive statistics of EC_{loess}^* ($mS\ m^{-1}$), EC_{clay}^* ($mS\ m^{-1}$) and z_{clay}^* (m) modelled with the DUALEM-21S measurements (m : mean, s^2 : variance and CV: coefficient of variation).	84
Table 6.1	Descriptive statistics (m : mean, min: minimum, max: maximum, s : standard deviation) of $E_{Ca_{p,1,1}}$, $E_{Ca_{p,2,1}}$, $E_{Ca_{v,1}}$ and $E_{Ca_{v,2}}$ for the 209 400 measurements in the study area (in $mS\ m^{-1}$ after conversion to a reference temperature of 25°C).	89
Table 6.2	Parameters of the variogram model for $E_{Ca_{v,1}}$, elevation of the current surface (Z) and z_{clay}^* (C_0 : nugget variance; $C_0 + C_1$: sill and a : range).	90
Table 6.3	Descriptive statistics (n : number, m : mean, min: minimum, max: maximum, s : standard deviation) of z_{clay} at the test field.	91
Table 7.1.	Descriptive statistics (m : mean, min: minimum, max: maximum, s : standard deviation) of $E_{Ca_{p,1,1}}$, $E_{Ca_{p,2,1}}$, $E_{Ca_{v,1}}$ and $E_{Ca_{v,2}}$ for the study site (39326 measurement points).	109
Table 8.1.	Descriptive statistics (m : mean, min: minimum, max: maximum, s : standard deviation) of $E_{Ca_{p,1,1}}$, $E_{Ca_{p,2,1}}$, $E_{Ca_{v,1}}$ and $E_{Ca_{v,2}}$ for the 20280 measurements on the 3.5 ha study site (in $mS\ m^{-1}$ after conversion to a reference temperature of 25°C).	120
Table 8.2.	Descriptive statistics (m : mean in $mS\ m^{-1}$ after conversion to a reference temperature of 25°C), CV: coefficient of variation in % and RD: relative difference in %) of $E_{Ca_{p,1,1}}$, $E_{Ca_{p,2,1}}$, $E_{Ca_{v,1}}$ and $E_{Ca_{v,2}}$ measurements and modelled EC_2^* stratified according to the two zones of the validation image.	127
Table 9.1.	Inventory of the metal objects in the subsoil at the 20 locations with metal predicted in the subsoil (p1 – p20) (in bold: shell remains, in italic: schrapnel) with their accompanied FEMP value (m : mass).	140

Chapter 1

Introduction

1.1 Overview

The need for detailed soil information for local decision making often arises from concerns with (i) the accuracy of the published soil information mapping, classification, and interpretation and with (ii) situations where the published information is too general for decisions about a specific area (McKenzie et al., 2008). Remote sensing imagery of a large variety of spaceborne and airborne sensors provides a huge amount of data about our earth surface for global and detailed analysis, change detection and monitoring. The limitations for image-based remote sensing applications are mainly due to sensor attributes, such as restricted spectral range, coarse spatial resolution, slow turnaround time, and inadequate repeat coverage (Moran et al., 1997) besides their multiple advantages (cheap and rapid, covering large areas, data from inaccessible regions, ...). For site-specific crop management and archaeological prospection, detailed estimates of soil properties and accurate localization of buried features are required. Moreover, soil properties should have a clear expression in the top centimeters of the soil to observe them with remote sensing. Proximal soil sensors were developed to quantify mechanical, physical and chemical soil properties with a high spatial resolution. Proximal soil sensing deals with the measurement of soil properties at close range or in contact with the soil. The increasing interest in proximal soil sensing manifest in the recent formation (july 2008) of a working group on 'Proximal Soil Sensing' under the auspices of both the 'Pedometrics Commission' and the 'Soil Physics Commission' of the 'Internation Union of Soil Sciences' (IUSS). Nowadays, a number of geophysical techniques are available, or currently being researched. It is important that the appropriate technique will be used for a given type of application. If the physical principles upon which a method is based are understood, then it is less likely that the technique will be misapplied or the resulting data misinterpreted. Generally, it is better to use methods that are sensitive to different physical properties and are able to complement each other providing an integrated approach for the characterization of the underground. Among all proximal soil sensing methods, the electromagnetic (EMI) techniques must have the broadest range of different instrumental systems of any, matched by the remarkable range of applications to which these methods are being applied (Reynolds, 1997). One of the main advantages of the EMI methods is that the process of induction does not require direct contact with the ground. Consequently,

the speed with which EMI surveys can be made is much higher (Moghadas et al., 2010). Different EMI instruments are currently being applied and investigated. These instruments provide apparent electrical conductivity (ECa) measurements of the soil. The ECa is the integration of the conductivities of the different entities in the measured soil volume. Initially, soil ECa was determined to quantify the soil salinity (Triantafilis et al., 2000). In non-saline conditions, differences in ECa were attributed to variation in soil physical properties, such as particle size distribution, moisture content and organic matter (Carroll and Oliver, 2005). When a GPS receiver and a data logger are used to record the position of each measurement, a map can be generated and processed along with other layers of spatially variable information (Adamchuk et al., 2004).

In 2001, the dual-dipole EM38 or the EM38DD soil sensor was developed by Geonics Ltd (Ontario, Canada), which provides two simultaneous measurements: ECa or apparent magnetic susceptibility (MSa) with two different depth extents. Due to its rich information output, this instrument showed potential for a variety of applications.

Vitharana (2008) aimed at delineating management classes with the EM38DD to implement site-specific soil management. Therefore, he mapped the within-field variation of relatively stable soil properties like soil textural fractions, pH, organic carbon and depth to subsurface compacted soil layers.

Cockx (2010) investigated the use of this proximal soil sensor to inventory and characterize soil properties at a high resolution. The investigation proved that soil ECa data from the EM38DD is a valuable source of ancillary information to improve soil inventories. Cockx et al. (2006) were the first to evaluate the dual dipole character of the EM38DD to obtain complementary information about soil profile heterogeneity: homogeneous soil profiles have similar ECa patterns while differing ECa patterns indicate a contrasting layer in the subsoil.

From this research, the awareness grew that combining the multiple EMI signals could improve the understanding of underground features. Therefore, the department of Soil Management decided to buy the DUALEM-21S (DUALEM Inc., Milton, Canada) sensor in 2006, providing 8 signals simultaneously. The department of Soil Management from the Ghent University was worldwide the first buyer of this sensor.

This instrument was used by Simpson (2009) to evaluate the combination of the multiple signals for geoarchaeological prospection. He recognized the potential of the MSa signal of both EM38DD and DUALEM-21S instruments, hereby highlighting local anomalies caused by antropogenic disturbances of the natural soil volume. With one EMI sensor, dual measurement of ECa and MSa or the complementary information about the natural soil variation and antropogenic disturbances enhances the insight on the physical nature of buried structures. Moreover, he emphasized the possibilities for depth sounding by combining the multiple signals and the sensibility to metal of the DUALEM-21S measurements. In order to

obtain good results, he insisted on a well-defined survey strategy and a data processing performed with great care.

During the last century, most European countries conducted nationwide surveys resulting in soil maps published on scales between 1/20,000 (e.g. Belgium) and 1/100,000 (e.g. Denmark), mostly with the aim to support agricultural development (Vitharana et al., 2008a). At present, many countries possess coverage of soil maps, with the main units expressed as differences in soil texture. Commonly, cartographic units on traditional soil maps depict a type of soil defined by a representative soil profile (Cosandey et al., 2003). Because soil sampling of profile horizons is labour-intensive, most soil studies focus on the topsoil only (Kerry and Oliver, 2007; Garten Jr. et al., 2007). However, the spatial variability of subsoil horizons is governed by pedogenic processes, while the topsoil variability of arable land is predominantly influenced by tillage homogenization (Sinegani et al., 2005). Therefore, the subsoil is often much more heterogeneous than the topsoil, both laterally and vertically. To investigate this vertical heterogeneity, the ECa of the EM38 was calibrated to the depth of the interface between the contrasting layers (Boll et al., 1996; Sudduth et al., 2003; Cockx et al., 2006; Cockx et al., 2007). These studies employ the ECa signal from one particular coil configuration. Because the depth of investigation is controlled by both coil spacing and coil orientation, simultaneous measurements attributed to multiple coil spacings or coil orientations provide more information in depth. The DUALEM-21S has multiple coil spacings and coil orientations, providing measurements with different depth sensitivity. The combination of these multiple signals shows potential for detailed inventories of the field-scale soil stratigraphy.

In archaeology, the integration of the multiple signals with specific depth sensitivity has the potential to detect more archaeological features than individual signals. Most archaeological features have a limited vertical depth extent, making them difficult to differentiate within a single ECa measurement. They are frequently masked by a high textural variability or by antropogenic disturbances. Combining and filtering the multiple signals could focus on enhancing the contrast between subtle anomalies caused by small archaeological features and the background values.

Electromagnetic induction surveys have been successful in detecting subsurface ferrous and non-ferrous metallic objects. Mostly, time-domain EMI instruments are used for unexploded ordnance (UXO) detection (Pasion and Oldenburg, 2001). They are able to measure at different times, hereby situating and characterizing the metallic object within some particular limits. Frequency-domain EMI sensors could also be used to indicate the presence of UXO (Huang et al., 2007), for example buried shells on historical battlefields. Frequency-domain EMI sensors measure the secondary field at one time, but the simultaneous (ECa) signals

could improve significantly the possibilities for signal processing to attempt an accurate localization and identification of the buried metal objects.

1.2 Research objectives

In order to implement site-specific crop management, to get more insight about the quaternary-geomorphology and to prospect for archaeological features or unexploded shells, quantification of the depth between contrasting underground layers or features is indispensable. The general aim was therefore to investigate the use of multiple signals of the EM38DD and DUALEM-21S EMI instruments to map the depth of the interface between contrasting soil layers and to locate different buried features. This should increase the time- and cost-effectiveness and decrease the required labour efforts for pedological, geomorphological and archaeological prospection and metal detection.

To reach the general aim, the following research questions were put forward:

- (i) *Which soil textural fractions influence the soil electrical conductivity to identify heterogeneous soil profiles?*

Different soil textural fractions prove to affect the measured soil ECa. The vertical heterogeneity or interface between contrasting layers can only be detected when the conductivity of the bordering soil layers differs substantially. Therefore, the first objective was to investigate which soil textural fractions influence the detectability of the different soil entities significantly.

- (ii) *Could one signal serve to model the depth between two contrasting layers accurately?*

In the past, the output of an EMI sensor was often a single measurement of ECa. This ECa measurement could be calibrated to observations of the depth of the interface between two contrasting layers. Finally, the entire ECa map was transformed into a map of the depth to the interface. Due to the lack of theoretical background, the errors on the modelling point out to be substantial. Therefore, the second objective was to evaluate theoretical approximations while fitting the sensor data to the depth observations, to achieve a more precise depth modelling.

- (iii) *Does combining multiple EMI measurements increase the accuracy and decrease the efforts for modelling the depth?*

The new EMI sensors measure simultaneously in multiple coil configurations with corresponding depth sensitivity. This enlarges the possibilities to perform depth sounding considerably. Depth sounding diminishes the labour efforts because calibration observations become redundant. Therefore, the objective was to develop a

multi-signal approach to model the depth of the interface between two contrasting layers non-invasively.

- (iv) *Is it possible to develop depth response curves for the different coil configurations?*

Most methodologies to model the depth between two contrasting layers use theoretical approximations for the depth sensitivity functions. Because the approximations are defined within delimited boundaries, the aim was to establish empirical sensitivity functions for each coil configuration and evaluate them on their potential to model the depth of the interface.

- (v) *Is it possible to model the depth of the interface when the upper material has a much higher conductivity than the lower layers?*

Most depth inversions are generally done to model the depth between low conductive material on the top and high conductive material in the subsoil. Callegary et al. (2007) stated that under more electrically conductive conditions (much higher conductivity at the top), the theoretical approximations for the depth sensitivity do not hold, providing a large error on the modelling predictions. Conductive topsoil is assumed to attenuate the transmitted electromagnetic signal. Therefore, the goal was to model accurately the depth of the interface between high conductive topsoil and low conductive subsoil fusing the multiple signals of the DUALEM-21S instrument.

- (vi) *Can archaeological features be accentuated by fusing the multiple signals?*

Archaeological features are regularly present as subtle anomalies in the geophysical data, difficult to distinguish from the natural background. They manifest as very small, weak distortions of the natural soil material and are likely to be eroded or covered by sediments. Therefore, the purpose was to establish a multi-signal approach to enforce the contrast between the subtle anomalies and the natural background.

- (vii) *Does the multi-signal approach improve metal delineation and estimation of mass and depth?*

Buried metal has a distinct influence on the EMI measurements, but the response and depth sensitivity reveals to be different for the different coil configurations and for the natural background. Therefore, the objective was to develop a procedure to combine the multiple signals of the DUALEM-21S to achieve a clear response from the buried metal objects. The developed procedure should recognize buried metal objects in historical battlefields (potentially unexploded shells), and estimate their mass and depth, with the final aim to discern the possible risks associated with excavation practices.

1.3 Structure of the thesis

The thesis is divided in nine chapters (Fig. 1.1). Chapter 2 focuses on the EMI proximal soil sensing, with the description of the theoretical principles, the instruments, mobile configuration and the geology and geomorphology of the study sites. Chapter 3 deals with the investigation of the main textural fractions affecting the ECa measurements for the identification of heterogeneous soil profiles. A procedure was proposed to characterize the type of heterogeneity. Chapter 4 describes a methodology to calibrate observations of the depth between contrasting layers to the ECa, using a theoretical depth sensitivity function. This was done on a study site with a high conductive substratum. In Chapter 5, a non-invasive procedure was proposed to model the depth between contrasting layers by integrating the multiple signals of the DUALEM-21S instrument. The accuracy of the predictions was compared with the procedure of using both EM38DD measurements and calibration observations. Chapter 6 presents the development of depth sensitivity functions for multiple coil configurations. The depth modellings were validated using geo-electrical imaging. Chapter 7 accentuates the influence of the inverse layeredness (compared to the previous chapters) on the accuracy of the depth calculations. The established multi-signal approach was applied to quantify the vertical extent of a tidal channel. Chapter 8 proposes a multi-signal methodology to accentuate subtle archaeological anomalies with the aim to guide excavations more efficiently. In chapter 9, a procedure was developed to filter and fuse the multiple signals of the DUALEM-21S instrument to highlight and delineate anomalies caused by buried metal objects. Moreover, depth and mass predictions were evaluated on a WW I battlefield.

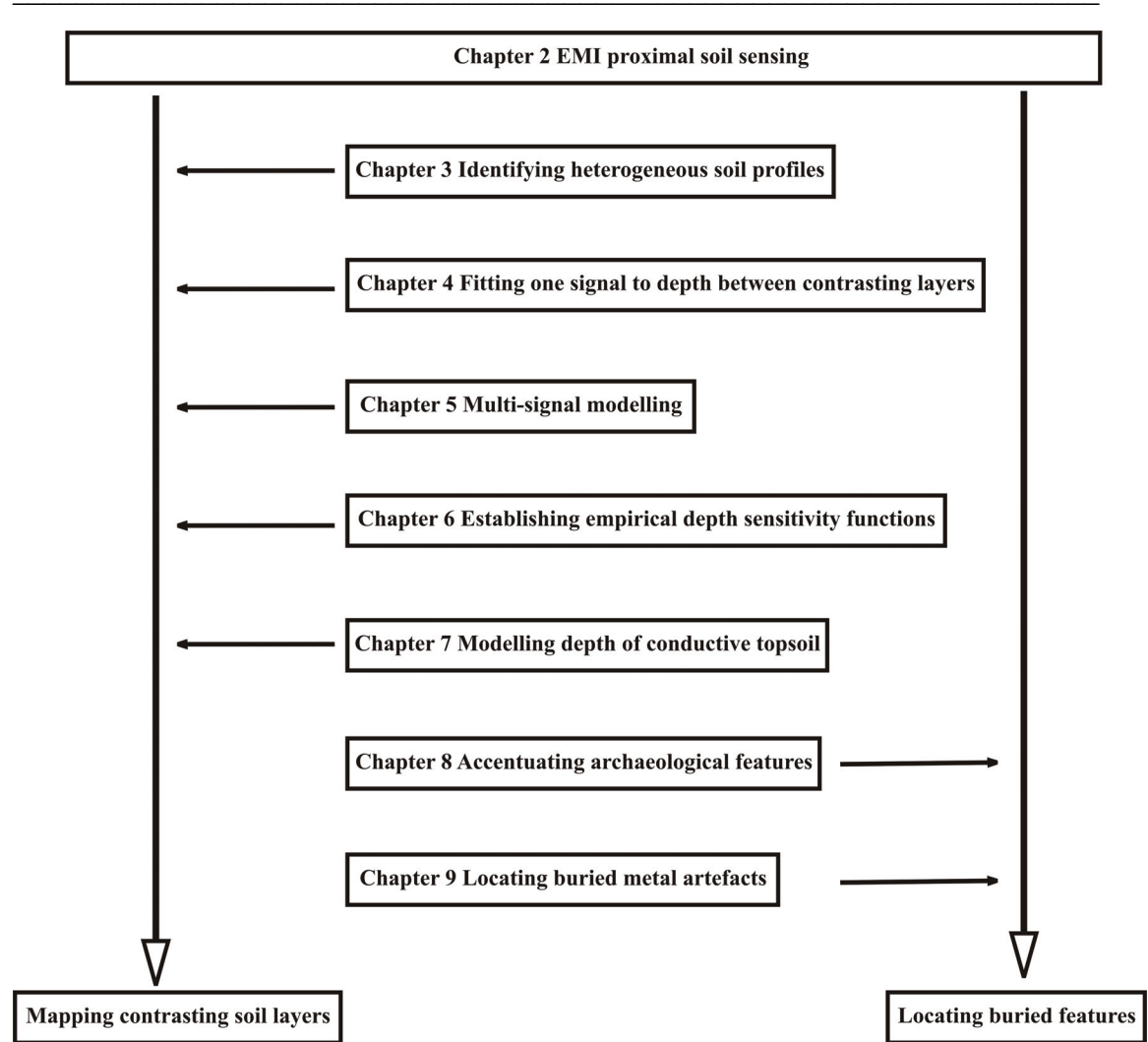


Fig. 1.1. Schematic overview of the thesis.

Chapter 2

Materials and methods: Proximal soil sensing

2.1 Introduction

Proximal soil sensing is defined as the use of field-based sensors to collect soil information from close by (within 2 m), or within, the soil body (Viscarra-Rossel et al., 2010). Soil can be defined as the loose top layer of the Earth's surface, consisting of rock and mineral particles mixed with decayed organic matter (humus) and capable of retaining water, providing nutrients for plants, and supporting a wide range of biotic communities. Soil can be influenced by human activity indicated by a concentration of phosphorus, organic matter, debris, or artifacts. The different soil and sediment components are physically mixed through cultivation, deforestation or construction. Generally, a soil consists of layers (or horizons), developed through the natural weathering of geological and archaeological surfaces, which differ chemically, physically, or biologically. Sequences of related soil horizons make up the soil profile.

The type of proximal soil sensor can be defined according to the geophysical method used, and the invasiveness of the soil. Geophysical methods respond to the physical properties of the subsurface media (rocks, sediments, water, voids ...) and can be classified into two distinct types: passive and active methods. Passive methods are those that detect variations within the natural fields associated with the Earth, such as the gravitational and magnetic fields; active methods generate signals that are transmitted into the ground, which then modify those signals in ways that are characteristic of the materials through which they travel (Witten, 2006). The altered signals are measured by appropriate detectors whose output can be displayed and ultimately interpreted. Invasive proximal soil sensors are in direct sensor-to-soil contact while non-invasive instruments measure the soil properties above the surface.

Different proximal soil sensing techniques can be distinguished: Ground Penetrating Radar, Magnetometry, Resistivity, Electromagnetic induction (EMI)... Development of proximal soil sensors was primarily done for improving the efficiency of crop production and raising the understanding of soil variability. Most proximal soil sensing techniques respond to a combination of different soil properties, making the interpretation of the measurements complicated. They may either measure the soil property directly or indirectly, by finding a

proxy that is easier and cheaper to measure and developing a pedotransfer function. Generally, the measured soil properties are not as accurate per individual measurement as conventional laboratory analysis. However, it facilitates the generation of larger amounts of spatial data using cheaper, simpler and less laborious techniques, which, as an ensemble, may be highly informative (Viscarra-Rossel et al., 2010). The large amount of measurements involves the accurate quantification of the horizontal spatial variability, allowing to describe a large amount of underground phenomena. It must be recognized that there is no universal geophysical method that will perform best for all applications and at all sites. Each method had strengths and weaknesses and exploits different physical principles and material properties of buried objects. A feature that is ‘invisible’ to one technique may be obvious in another. Different techniques can complement each other to come to an unambiguous understanding and identification of a buried feature (Witten, 2006). In this study, EMI was the main (active and non-invasive) technique used for mapping the depth between contrasting layers and for locating buried features. The other main techniques for proximal soil sensing are described briefly.

2.2 Ground Penetrating Radar, Magnetometry and Electrical Resistance

2.2.1 Ground Penetrating Radar

The Ground Penetrating Radar (GPR) transmits electromagnetic waves with a high frequency in the range of 10 MHz – 1.5 GHz (Fig. 2.1). They require a close contact between the transmitter antenna and the soil. The electromagnetic waves are transmitted by an antenna and penetrate in the soil with a speed determined by the dielectric properties of the soil, especially the dielectric permittivity (Lunt, 2004). The waves propagate through the soil and are reflected at discontinuities in dielectric properties or attenuated by absorption. The absorption losses are mainly due to the clay and moisture content of the soil. The reflected waves are received by the antenna and both the strength and the travel time of the wave are recorded. When the velocity of the wave through the soil is known, the depth of the discontinuity can be deduced from the travel time of the wave (Moorman, 1990). GPR can also be used to determine the soil moisture content. With low clay and moisture content of the soil, the penetration depth of the ground penetrating radar is mainly determined by the antenna frequency: the higher the frequency, the lower the penetration depth. GPR can be limited by the size and depth of features of interest. Attenuation of the radar wave is mainly controlled by the electrical conductivity of the host. If the conductivity is too high, sufficiently high

frequencies to resolve a given feature may not penetrate to the necessary depth, as frequently the case in clayey soils (Witten, 2006).

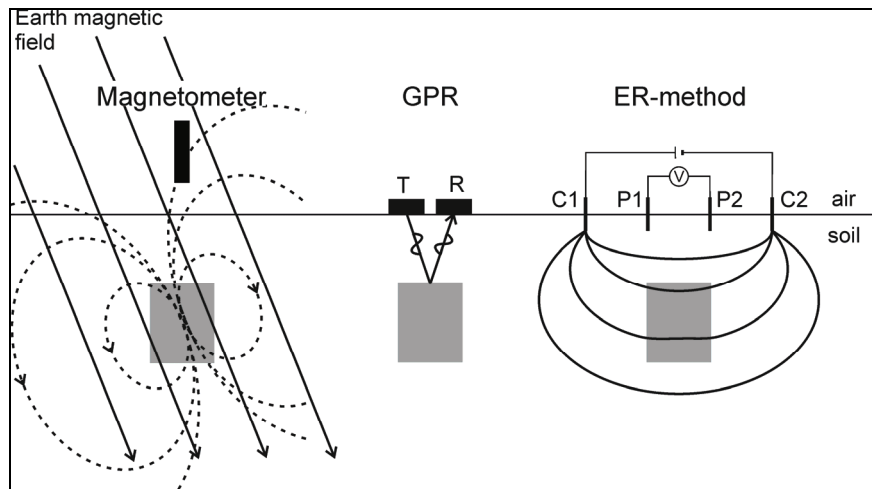


Fig. 2.1. Basic principles of Magnetometry (left), Ground Penetrating Radar (GPR) (middle) and Electrical Resistivity (ER) (right) (Simpson, 2009).

2.2.2 Magnetometry

Magnetometry uses the earth magnetic field as an energy source, so it is a passive method. The magnetic field of the earth is homogeneous with regard to the field strength and the direction of the field strength. If a magnetic feature on or above the ground surface is brought into this homogeneous field, the own field of the object is superposing the local magnetic field of the earth, hence creating a distortion (Fig. 2.1). However, the local magnetic field of the earth has a diurnal variation, influenced by the magnetic field of the sun (Reynolds, 1997). Therefore, magnetometers are mostly placed in gradiometer configuration. A gradiometer measures the difference (pseudogradient) in total magnetic field strength between two identical magnetometers separated by a small difference. The magnetic field gradient is expressed in units of nT m^{-1} . As gradiometers measure the vertical magnetic gradient, noise effects from long-wavelength features are suppressed and anomalies from shallow sources are emphasized. Different types of magnetometers exist, from which the most common are the fluxgate and caesium vapor (Witten, 2006). Fluxgate magnetometers measure the vertical component of the magnetic field and can provide measurements accurate to about 1 nT. Caesium vapor magnetometers measure the total magnitude of the magnetic field and are much more sensitive than the fluxgate instruments (0.01 nT). The basis for magnetic prospecting is the presence of weakly magnetized iron oxides in the soil. Therefore, it is generally related to anthropogenic activity and frequently used in archaeological prospecting (Gaffney and Gater, 2003).

Magnetometry has two important complications: (i) the Earth's field is dipolar, which means that a single anomaly can have the form of a positive peak only, a negative peak only, or a positive and negative peak; (ii) remanent magnetization plays an important role in the measurements. Generally, the remanent magnetic component in the observed magnetic field is neglected, possibly biasing the interpretations.

2.2.3 Electrical Resistance

Measurements with electrical resistance (ER) methods imply the insertion of electrodes into the soil, measuring the earth resistance to the flow of charge through the soil. In his conventional configuration, the ER system consists of four coulter electrodes, from which two electrodes are the current transmitters and two the receiving electrodes (Fig. 2.1). The flow of charge is introduced at the soil surface and the difference in current potential due to the resistance of the soil is measured. The ratio of the measured potential difference and the current strength is equal to the earth resistivity according to Ohm's law (Gaffney and Gater, 2003). Mostly, the apparent electrical resistivity is measured. This is the resistivity that the soil would have if perfectly homogeneous with a uniform resistivity value. The depth of investigation of the electrode array is a function of the electrode spacing: the greater the spacing between the current electrodes, the deeper the flow of charge will penetrate into the soil. Mostly, multiple electrodes are used so multiple depths can be scanned simultaneously. A drawback is that the electrodes need a close contact with the soil. This is difficult to achieve in dry soils or soils with a lot of stony material.

Generally, the purpose of electrical resistance surveys is to determine the resistivity distribution of the sounding soil volume. Potential difference patterns provide information on the form of subsurface heterogeneities and of their electrical properties. The greater the electrical contrast between the soil matrix and heterogeneity, the easier is the detection (Samouëlian et al., 2005).

In this study, we used both a standard EC-probe set for direct soil conductivity measurements and the ABEM Terrameter and Lund electrode selector system (ABEM instrument AB, Sundbyberg, Sweden) for resistivity imaging. The EC-probe set consists of an EC-probe and an earth resistivity meter (Eijkelkamp Agrisearch Equipment, Giesbeek, The Netherlands). Measurement of the soil resistivity using four electrodes is based on the Wenner-method, described by Rhoades and Van Schilfgaarde (1976). Fig. 2.2 gives a schematic overview of the instrument. The power source (6) generates an alternating current between the two current electrodes (1 and 4) thereby creating an electric field. Its strength depends on the strength of the current and the distance between the four electrodes (all 25 mm separated). Resistivity of the soil causes decreased voltage between the current electrodes. The earth resistivity meter

(7) measures a potential difference between the measuring electrodes (2 and 3). The ratio between the registered potential difference and the strength of the current equals the resistivity. The EC-probe measures in situ the electrical resistivity of a limited (elliptic) soil volume of 80 cm³ of soil around the probe. A temperature sensor is used to convert the measurements to a reference temperature. This sensor can be used only for a limited number of punctual measurements, because of the labour efforts involved. Moreover, these act as calibration measurements for the proximal soil sensing data.

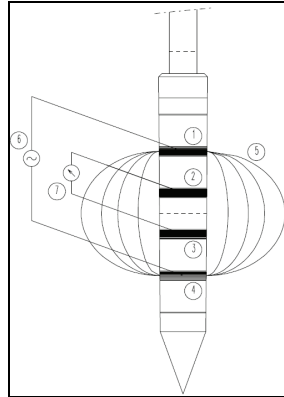


Fig. 2.2. EC-probe with indication of its components: current electrodes ((1) and (4)), measuring electrodes ((2) and (3)), power source (6) and resistivity meter (7).

The ABEM Terrameter and Lund electrode selector system was applied to map the interface between contrasting layers. With this multi-electrode resistivity system, 64 electrodes were arranged in a straight line with a constant spacing of 1 m and connected to a multi-core cable. A controller system selected the combination of four active electrodes for each measurement of the resistivity data. The data can be interpreted to determine a two-dimensional resistivity model for the subsurface which produces a pseudosection that agrees with the actual measurements. The distance for the electrode configuration midpoint can be plotted against the electrode separation for each measured data point, reflecting the measurement depth. The corresponding apparent resistivity along the vertical section allows geological boundaries to be identified, by characterizing the ground in terms of the thickness of individual layers together with their respective apparent resistivity values along the vertical profile (Batte et al., 2008).

2.3 Electromagnetic induction

2.3.1 Principle

Electromagnetic methods can be classified as either (i) time-domain or (ii) frequency-domain systems. Frequency-domain uses either one or more frequencies whereas time-domain makes measurements as a function of time. Electromagnetic methods use the response of the ground to the propagation of incident alternating electromagnetic waves which are made up of two orthogonal vector components: an electric intensity (**E**) and a magnetizing force (**H**), in a plane perpendicular to the direction of travel (Fig. 2.3) (Frischknecht et al., 1991).

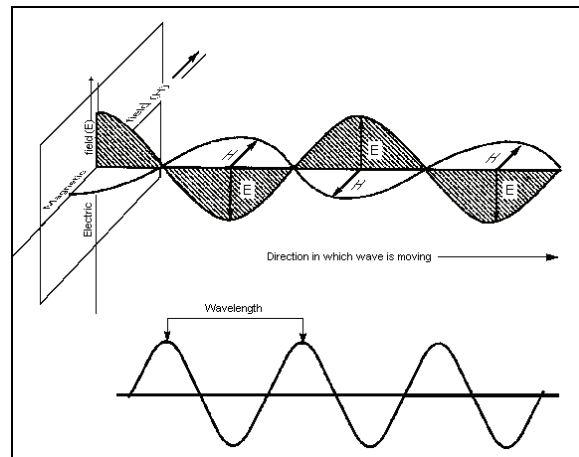


Fig. 2.3. Basic elements of an electromagnetic wave with electric (**E**) and magnetic (**H**) components (WHO, 1998)

Maxwell's four equations describe these electric and magnetic fields arising from varying distributions of electric charges and currents, and how those fields change in time. Two of the Maxwell equations are particularly important to understand the principle of electromagnetic induction sensors: the Ampère's law with Maxwell's correction and the Faraday's law:

The Ampère's law with Maxwell's correction states that magnetic fields can be generated in two ways: by electrical current (Ampère's law) and by changing electric fields (Maxwell's correction). In the case of static electric field, the magnetic field around a closed loop is proportional to the flow of charge passing through the loop. It also means that a changing magnetic field creates an electric field, and a changing electric field creates a magnetic field. The differential form of this equation can be written as:

$$\nabla \times \mathbf{H} = \sigma \cdot \mathbf{E} + \varepsilon \cdot \frac{d\mathbf{E}}{dt} \quad [2.1]$$

with σ the conductivity and ε the permittivity of the medium.

Faraday's law describes how a changing magnetic field can create ('induce') an electric field, proportional to the time rate of change of the magnetic flux threading the circuit. Any change in the magnetic environment of a coil of wire will cause a voltage to be induced in the coil. The change can be produced by changing the magnetic field strength or moving the coil into or out of the magnetic field for example. The differential form of Faraday's law can be described as:

$$\nabla \times \mathbf{E} = -\mu \frac{d\mathbf{H}}{dt} \quad [2.2]$$

with μ the magnetic susceptibility of the medium.

Frequency-domain electromagnetic induction sensors exist of both transmitter and receiver coils. According to Ampère's law with Maxwell's correction, a time-varying magnetic field (\mathbf{H}_p) arises when an alternating charge flows through the transmitter coil. This primary electromagnetic field propagates above and below the ground (Fig. 2.4). According to Faraday's law, this field creates eddy (alternating) currents in the electrically conductive soil or in an object embedded in the soil. The currents induced in an object in the ground are a function of the time rate of change of the primary field at the object and the objects size, shape, conductivity and magnetic susceptibility and of the conductivity and permittivity of the surrounding soil. These time-varying currents then induce their own (secondary) magnetic field which is detected by a receiver coil (\mathbf{H}_s). This coil also detects the primary field traveling through the air, so the overall response is the resultant effect of both the primary and induced fields. Both fields induce currents in the coil, from which the current can be measured. The magnitude of the induced voltage is directly proportional to the rate of change of the magnetic field.

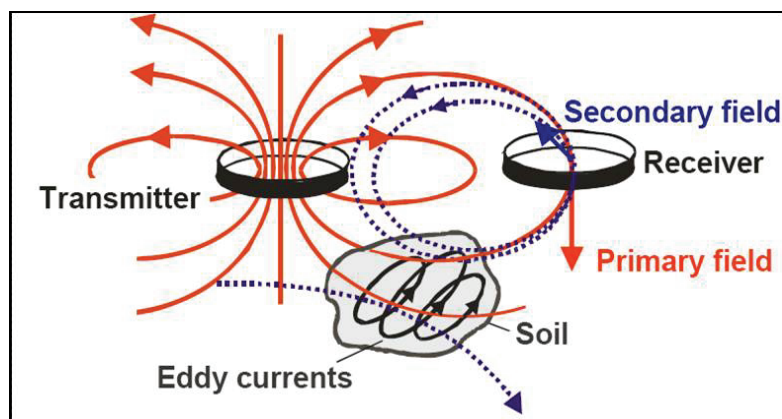


Fig. 2.4. Basic principle of electromagnetic induction sensing.

With frequency-domain EMI sensing, the applied alternating voltage has the form of a sine wave with an angular wave frequency of ω ($= 2\pi f$) and an amplitude which varies as a

function of time. Eddy currents take a finite time to generate, arising from the induced voltage. Therefore, the difference in time between the primary and secondary magnetic field at the receiver coil is described by a phase lag and amplitude, depending on the electrical properties of the subsurface materials (Reynolds, 1997). The proximal soil EMI instruments are developed to measure two components of the secondary field, obtained by Fourier transformation during signal processing. The in-phase and quadrature-phase components are shown on the vector diagram in Fig. 2.5. The in-phase response is a proxy of the amplitude of the secondary field measured when the primary field is at its maximum; the quadrature-phase response reflects the amplitude of the secondary field when the primary field is 0. The amplitude and phase of the secondary magnetic field will differ from those of the primary field as a result of soil properties, spacing of the coils and their orientation, frequency of the instrument and distance from the soil surface. (Hendrickx and Kachanoski, 2002)

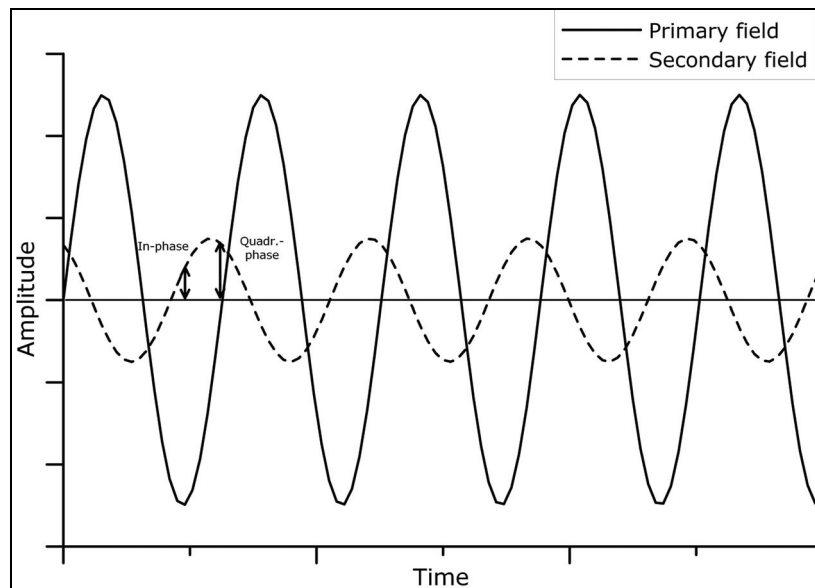


Fig. 2.5. Amplitude of the primary and secondary field, oscillating in time.

2.3.2 Instrument output to conductivity

Frequency-domain EMI instruments measure a depth-weighted average of the soil electrical conductivity: the apparent electrical conductivity (ECa). EMI instruments operating at very low induction numbers (β) are sometimes called terrain conductivity meters (Spies and Frischknecht, 1991). Low induction numbers imply the charge flowing in any loop of the magnetic field to be completely independent of the charge that passes in any other loop since they are not magnetically coupled (McNeill, 1980b). The induction number is the ratio of the intercoil separation s to the skin depth δ . This skin depth is defined as the distance at which the propagating magnetic field strength has been attenuated to e^{-1} (or 37 %) of the strength at

the surface. The skin depth varies inversely with conductivity and magnetic susceptibility of the soil and frequency of the instrument (McNeill, 1980b).

$$\delta = \sqrt{\frac{2}{\omega\mu\sigma}} \quad [2.3]$$

Within the restriction of a small β , the instrument output $\left(\frac{H_p}{H_s}\right)_{\text{quadrature-phase}}$ is proportional to the ECa or σ :

$$\left(\frac{H_p}{H_s}\right)_{\text{quadrature-phase}} = \left(\frac{s}{\delta}\right)^2 \quad [2.4]$$

Eqs. (2.3) and (2.4) can be combined to obtain σ as a function of the instrument output:

$$\sigma = \frac{2}{\omega\mu s^2} \cdot \left(\frac{H_p}{H_s}\right)_{\text{quadrature-phase}} \quad [2.5]$$

The in-phase response can be related to the magnetic susceptibility of the soil at low β .

The most common type of instrument uses separated transmitter and receiver coils. Different configurations exist: the vertical, horizontal and perpendicular coil configurations. The quadrature component is proportional to the conductivity and the output of the instruments is calibrated to show the ECa rather than the quadrature component. Most of the instruments measure the in-phase component, primarily depending on the magnetic susceptibility of the earth. In conductivity mapping, the specific instrument or spacing and the configuration are chosen to maximize the response from the depth that is of greatest interest. Measurements at two or more combinations of spacings or orientations enlarge the information output of the instruments (Dualem inc., 2007). The principle method of calibrating low induction number instruments is by raising them to a suitable height above the earth. Only the primary magnetic field will then be measured and nulled.

2.3.3 Penetration depth

With Frequency Domain Electromagnetic Induction (FDEM) sensors, three main factors determine the penetration depth: (i) the frequency from the continuously oscillating electromagnetic field, (ii) the distance in-between the transmitter and receiver coils and (iii) the orientation of the transmitter and receiver coils. The relative response to the primary magnetic field created by the EMI instruments varies with depth and is therefore expressed as a depth response function (Morris, 2009).

McNeill (1980b) defined the depth response functions of EMI instruments in homogeneous soils by asymptotic approximations of Maxwell's equations. The ECa measurements for the vertical, horizontal and perpendicular coil configurations can be represented as:

$$ECa_v = \sum_{i=1}^N EC_i (R_v(x_i) - R_v(x_{i-1})) \quad [2.6]$$

$$ECa_h = \sum_{i=1}^N EC_i (R_h(x_i) - R_h(x_{i-1})) \quad [2.7]$$

$$ECa_p = \sum_{i=1}^N EC_i (R_p(x_i) - R_p(x_{i-1})) \quad [2.8]$$

with x_i the normalized depth expressed as ratio of the depth z_i or the depth of the interface between layers i and $i+1$ to the intercoil spacing s , EC_i is the value of the average electrical conductivity (EC) of layer i , $R_v(x_i)$, $R_h(x_i)$ and $R_p(x_i)$ are the values of the cumulative response at normalized depths x_i or at the interface between layers i and $i+1$ for the vertical, horizontal and perpendicular coil configurations. These cumulative response functions are given by McNeill (1980b) and Wait (1962):

$$R_v(x_i) = 1 - \left(4 \cdot \frac{z_i^2}{s^2} + 1\right)^{-0.5} \quad [2.9]$$

$$R_h(x_i) = 1 - \left(4 \cdot \frac{z_i^2}{s^2} + 1\right)^{0.5} + 2 \cdot \frac{z_i}{s} \quad [2.10]$$

$$R_p(x_i) = 2 \frac{z_i^2}{s^2} \left(4 \frac{z_i^2}{s^2} + 1\right)^{-0.5} \quad [2.11]$$

An increase in penetration depth can be obtained by increasing s . The larger the intercoil spacing, the deeper the magnetic field penetrates into the soil.

2.3.4 Electrical conductivity

Proximal bulk apparent electrical conductivity sensors can be used to produce high spatial resolution maps that integrate conductivity variation in the soil profile by a depth-response function. For meaningful interpretation, the conductivity data must either be inverted to approximate profile conductivity or directly calibrated to profile properties (Myers et al., 2010). Thus, the quadrature component of proximal EMI sensors provide the apparent or 'depth weighted' electrical conductivity.

If a potential difference ΔV exists between two electrodes connected with a conducting wire, and a charge with strength I passes through it, then Ohm's Law states (Corwin and Lesch, 2003):

$$R = \frac{\Delta V}{I} \quad [2.12]$$

With R the electrical resistance of the wire, depending on its cross-sectional area A and its length l . The electrical resistivity ρ has the units ohm m^{-1} and is therefore independent of the dimensions of the material:

$$\rho = R \frac{A}{l} \quad [2.13]$$

Electrical conductivity, as the inverse of electrical resistivity, is a measure of how well a rock passes electric charges. There are three ways in which electric charges can be conducted through a rock (Reynolds, 1997):

- (i) Electrolytic conduction occurs by the relatively slow movement of ions within an electrolyte and depends upon the type of ion, ionic concentration and mobility.
- (ii) Electronic conduction is the process by which metals, for example, allow electrons to move rapidly, so carrying the charge.
- (iii) Dielectric conduction occurs in very weakly conducting materials when an external alternating current is applied, causing atomic electrons to be shifted slightly with respect to their nuclei.

In most soils, conduction occurs by pore fluids acting as electrolytes with the particles contributing very little to the overall conductivity. Soil creates a flow of charge in varying levels; the higher the conductivity of a given soil, the higher the flow of charge through it. Conductivity of soil varies with moisture and temperature, and the conductivity of a given soil varies throughout the year. The electrical resistivity can be defined as the inverse of the conductivity σ . Generally, σ is expressed in S m^{-1} , but the range of values commonly measured in soils is better expressed in mS m^{-1} (Samouëlian et al., 2005).

Most soil and rock materials are electrical insulators of very high resistivity. In general the conductivity is electrolytic and takes place through the moisture-filled pores and passages which are contained within the insulating matrix. The conductivity is therefore defined for both rocks and soils (Table 2.1) by:

- (i) the porosity: shape and size of pores and size and shape of interconnecting passages;
- (ii) the moisture content: the extent to which the pores are filled by water;
- (iii) concentration of dissolved electrolytes in the contained moisture;
- (iv) temperature;
- (v) amount and composition of colloids.

Table 2.1. Indicative resistivity and conductivity values of different soil types (Bevan, 1983).

Soil	Resistivity (Ohm m)	Conductivity (mS m ⁻¹)
Sand, gravel	1000 – 10000	0.1 – 1
Silty sand	200 – 1000	1 – 5
Loam	80 – 200	5 – 25
Silt	40 – 80	12.5 – 25
Clay	10 – 40	25 – 100
Saline soil	5 – 10	100 – 200

E_{Ca} in sufficiently moist soils is primarily related to the salts contained in the soil water occupying the larger pores. The solid phase contributes also to the E_{Ca}, primarily via the exchangeable cations associated with clay minerals. A third pathway exists through soil particles in direct and continuous contact with one another. (Rhoades et al., 1989).

To conclude, the measurement of E_{Ca} by EMI techniques is complicated by the influence of several soil properties aside from soil salinity, including soil texture, organic matter content, bulk density, water content and temperature. For this reason, it is necessary to determine the dominant soil properties influencing the E_{Ca} measurements at each site to interpret what information is being conveyed by an E_{Ca} map (Corwin and Lesch, 2003).

2.3.5 Instruments

Two EMI proximal soil sensing instruments were used in this thesis: the EM38DD and the DUALEM-21S. The EM38DD consists of two coupled EM38 sensors oriented perpendicular to each other. Each EM38 sensor has a transmitter and a receiver coil, 1 m apart. The sensor in the horizontal orientation has both transmitter and receiver coils parallel to the earth's surface while in the vertical orientation both coils are perpendicular to the surface.

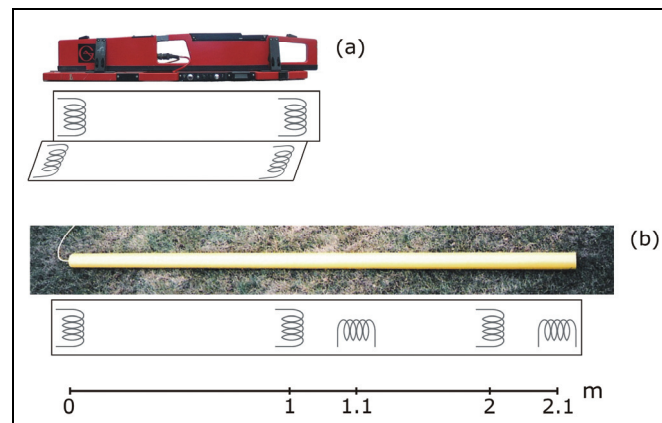


Fig. 2.6. Transmitter and receiver dipole orientations and coil spacings of the EM38DD (a) and DUALEM-21S (b).

The DUALEM-21S sensor consists of a 2.41 m long tube. This sensor has one transmitter and four receiver coils at different spacing (Fig. 2.6). The transmitter coil is located at one end, the receiver coils are at 1, 1.1, 2 and 2.1 m spaced from the transmitter coil. The 1 and 2 m transmitter-receiver pairs form a vertical dipole mode, while the 1.1 and 2.1 m pairs form a perpendicular dipole mode. So the EM38DD and the DUALEM-21S EMI sensors differ in orientation and distances between the transmitter-receiver coils. Due to the various coil orientations and transmitter-receiver spacings, the DUALEM-21S instrument has a large potential to perform depth sounding.

2.3.6 Cumulative depth response

For the EM38DD and the DUALEM-21S, the cumulative response of a layered medium up to a depth z (m) below the sensor was given by Eqs. (2.9), (2.10) and (2.11). Based on the different spacings between the DUALEM-21S transmitter and receiver coils, four different cumulative depth response profiles were established. Fig. 2.7 shows the cumulative response relative to an increase in z of the two coil configurations (vertical (R_v) and horizontal (R_h)) of the EM38DD and the four coil configurations (1 m vertical ($R_{v,1}$), 1.1 m perpendicular ($R_{p,1.1}$), 2 m vertical ($R_{v,2}$) and 2.1 m perpendicular ($R_{p,2.1}$)) of the DUALEM-21S. Due to the non-linear shape of the cumulative response curves, the depth of exploration (DOE) can be arbitrarily defined as the depth where 70 % of the response is obtained from the soil volume above this depth. This DOE increases from the DUALEM_{p,1.1} (0.54 m) coil configuration over the EM38_h (0.76 m), DUALEM_{p,2.1} (1.03 m) and EM38_v or DUALEM_{v,1} (1.55 m) to the DUALEM_{v,2} configuration (3.18 m) (Fig. 2.7).

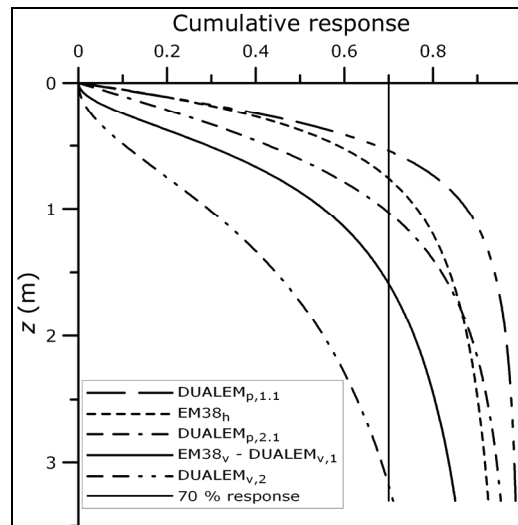


Fig. 2.7. Cumulative response as a function of the depth z for the EM38DD and DUALEM-21S instruments.

2.3.7 Mobile measurement equipment

Mounting EMI proximal soil sensors in a mobile configuration enables the surveyer to obtain a large number of measurements within a small time. Both EM38DD and DUALEM-21S sensors were mounted on a rugged, non-metallic polyethylene sled pulled by an all terrain vehicle (ATV), surveying speed is limited to 6-10 km h⁻¹ (Fig. 2.8). Due to the sled construction, the DUALEM-21S instrument was located 0.16 m above the soil surface. The ECa measurements were recorded at 8-10 Hz on a field computer. A Trimble AgGPS332 (Trimble Inc, Colorado, USA), with OmniSTAR differential correction (OmniSTAR Inc., Texas, USA) was used to georeference the ECa measurements with a pass-to-pass accuracy of approximately 0.10 m. An Allegro field computer (Juniper Systems Inc., Utah, USA) acts as a hardware unit to connect the EMI instrument and the GPS receiver through two serial ports. The HGIS software (Starpal Inc., Colorado, USA) onto the rugged field computer merges the ECa measurements and the GPS coordinates (NMEA-GGA format, 1 Hz) into one file. Generally, measurements were taken along parallel lines separated with a predefined, fixed distance in-between (from 0.3 to 4 m). Driving was supported by a Trimble Lightbar Guidance System ensuring straight driving lines to obtain measurements in an approximate grid sampling configuration or even a full coverage of the area. Additionally, at each ECa measurement point, the soil surface elevation was acquired with the Trimble AgGPS332 (accuracy ± 0.30 m).

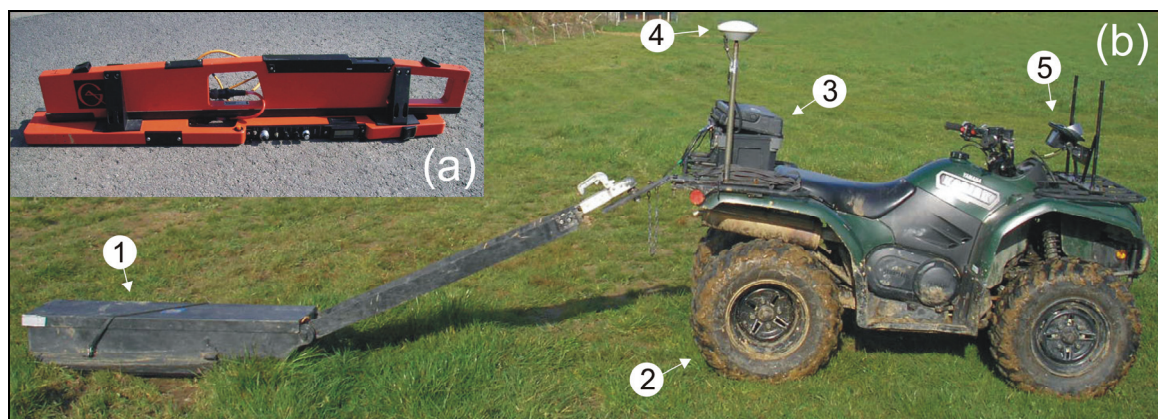


Fig. 2.8. EM38DD (a) and Mobile ECa -measurement equipment (b); 1: Sled with EM38DD, 2: All Terrain Vehicle, 3: Trimble AgGPS332 and field computer, 4: GPS antenna, 5: Lightbar Guidance System.

Calibration of the EMI instruments is different for the two systems: the EM38DD sensor needs to be calibrated manually, according to the instructions of the manufacturer. The DUALEM-21S instrument is programmed to perform an automatic calibration at the start of

each new survey. However, changes in air temperature, humidity and atmospheric electricity can put a systematic shift on the ECa measurements. Therefore, all measurement need to be set to the same reference and corrected for drift during the measurements.

Generally, the following guidelines were followed in carrying out the EMI based-surveys (adapted from Corwin and Lesch (2003)):

- (i) Define the survey's objective;
- (ii) Establish the site boundaries;
- (iii) Record the site metadata;
- (iv) Select the GPS coordinate system;
- (v) Establish the measurement intensity (distance in-between the tracks);
- (vi) Georeference the site boundaries and significant physical geographic features with GPS;
- (vii) Measure with the EMI instrument (with sporadic measurements of soil temperature) at the predetermined spatial intensity and record associated metadata;
- (viii) Statistically analyze the ECa data using an appropriate statistical sampling design to establish 'ground truthing' (soil sampling) locations;
- (ix) Establish site locations, sample depth increments, number of sites with duplicates or replicates and associated metadata;
- (x) Analyse the physico-chemical properties of interest as defined by the project's objective;
- (xi) Conduct a sensitivity analysis to establish dominant soil property(ies) influencing the ECa;
- (xii) Formulate a spatial linear regression model that relates the dominant soil property(ies) to the ECa;
- (xiii) Create maps with the spatial distribution of soil properties.

2.4 Interpolation

With our mobile measurement equipment, sensor measurements and DGPS-positions were simultaneously recorded. Although a Lightbar Guidance System was used to ensure driving on straight parallel lines with a fixed distance in-between, the measurements are not located on a fixed grid. Therefore, the measurements need to be interpolated. Nearly all the methods of interpolation or prediction can be seen as methods that predict the value at the unknown position as the weighted average of all the measurements within a circular or rectangular area around the unknown position.

If the location of the i^{th} measurement of N within the search area is \mathbf{x}_i with sensor measurements of $z(\mathbf{x}_i)$ and \mathbf{x}_0 the location of the unknown value $z^*(\mathbf{x}_0)$, then the unknown value is calculated as:

$$z^*(\mathbf{x}_0) = \sum_{i=1}^N w_i \cdot z(\mathbf{x}_i) \quad [2.14]$$

with w_i the weights summing to 1.

Most interpolation methods differ in the way the weights are attributed to the measurements. Mostly, ‘inverse distance to a power’ and ‘ordinary point kriging’ are used as interpolation techniques for dense proximal sensor-data.

The weights of the ‘inverse distance to a power’ method are determined by the distance h between \mathbf{x}_0 and \mathbf{x}_i and a user-defined power p :

$$w_i = \frac{h_i^{-p}}{\sum_{i=1}^N h_i^{-p}} \quad [2.15]$$

This implies that the closer the measurements are to the location of the unknown value, the more weight this measurement will give in the estimated value, or the relative weights diminish rapidly as the distance increases, and so the interpolation is sensibly local. In many instances, the measurements are not uniformly spaced around the locations to interpolate, with several in a particular direction and fewer in others. This situation produces a spatial bias of the estimate, as the clustered points carry an artificially large weight. This can be problematic with our sensor measurements, because we have a lot more measurements in the line than between the lines. With kriging interpolation, less weight is given to clustered measurements than for evenly distributed measurements. Implementing this also implies that observations close to each other are correlated. This is certainly the case. In a lot of situations, values at two places near to one another are similar, whereas those at more widely separated places are less so, or observations are correlated to some degree in relationship with the distance between the observations. Therefore, quantification of the spatial variation should be done when interpolating the measured sensor data.

Kriging makes the best use of existing knowledge by taking account of the way that a property varies in space through the variogram model, which is used to assign weights to the neighbouring measurement points. The variogram models are expressed by a semivariance γ , which quantifies the degree of spatial relationship or spatial correlation between two observations. It is the variance per point when the points are considered in pairs. The semivariance γ measures the average dissimilarity between N pairs of measurements separated by a distance \mathbf{h} and can be calculated based on a series of observations $z(\mathbf{x}_i)$ (Webster and Oliver, 2007):

$$\gamma(\mathbf{h}) = \frac{1}{2N(\mathbf{h})} \sum_{i=1}^{N(\mathbf{h})} [z(\mathbf{x}_i + \mathbf{h}) - z(\mathbf{x}_i)]^2 \quad [2.16]$$

When plotting these values for an increasing lag distance, a model of the spatial structure can be achieved. Generally, pairs of observations closer together should show a smaller semivariance than pairs further away. A plot of the calculated $\gamma(\mathbf{h})$ against the \mathbf{h} reveals the experimental variogram to which a theoretical model is fitted (Fig. 2.9).

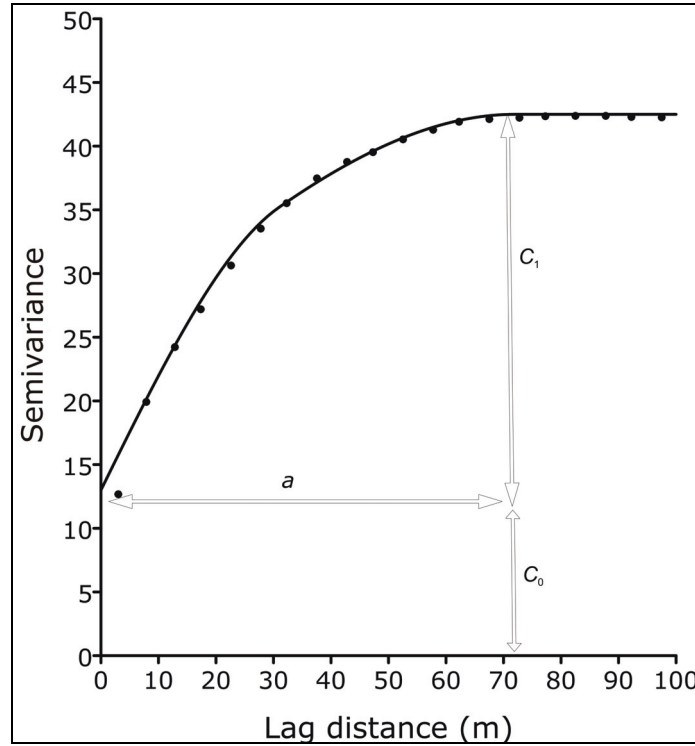


Fig. 2.9. An experimental variogram (points) fitted by a theoretical variogram model (line)

Typically, the semivariance increases from low lag distances to high lag distances, reflecting the dissimilarity increasing with increasing distances. The steeper the slope of the variogram model, the more the dissimilarity with increasing distance. Fig. 2.9 shows that the slope of the variogram model decreases, indicating that the dissimilarity decreases with increasing distance between the measurements. With large distances, the semivariance values remain constant, i.e. no correlation exists between the measurements. The variogram models are described by three parameters as a quantification of the spatial variance: the nugget variance (C_0), the sill variance ($C_0 + C_1$) and the range (a). The value at lag distance zero is sometimes >0 , this is called the nugget variance or random noise on the measurements. This is the variance at distances smaller than the smallest sampling lag or the unexplained variation. The value of the maximum semivariance is called the sill variance; it is the upper bound at which the variogram remains after its initial increase. This sill variance is equal to the sampling variance or the semivariance at zero autocorrelation. The range is the lag distance at which the

autocorrelation becomes zero or where the variogram reaches its sill. It is the limit of the spatial dependence (Webster and Oliver, 2007).

The applied variogram models in this study are the Spherical, Exponential, and Gaussian models. These models are bounded in the sense that they reach their sill at a particular range (Spherical) or asymptotically (Exponential and Gaussian) (for all models: $\gamma(0) = 0$) :

(i) Spherical model:

$$\gamma(h) = \begin{cases} C_0 + C_1 \left\{ \frac{3h}{2a} - \frac{1}{2} \left(\frac{h}{a} \right)^3 \right\} & \text{if } 0 < h \leq a \\ C_0 + C_1 & \text{if } h > a \end{cases} \quad [2.17]$$

(ii) Exponential model:

$$\gamma(h) = C_0 + C_1 \left\{ 1 - \exp\left(\frac{-3h}{a}\right) \right\} \quad \forall \quad 0 < h \quad [2.18]$$

(iii) Gaussian model:

$$\gamma(h) = C_0 + C_1 \left\{ 1 - \exp\left(\frac{-h^2}{a^2}\right) \right\} \quad \forall \quad 0 < h \quad [2.19]$$

In this study, ordinary point kriging (OK) was used as interpolation method. OK provides estimates of a variable at any unsampled location using a linear combination of observations within a predefined neighbourhood around this location (Goovaerts, 1997). OK involves the solving of a set of equations to obtain the weights w_i :

$$\sum_{i=1}^N w_i \gamma(\mathbf{x}_j - \mathbf{x}_i) + \psi = \gamma(\mathbf{x}_j - \mathbf{x}_0) \quad [2.20]$$

$$\sum_{i=1}^N w_i = 1 \quad [2.21]$$

with $\gamma(\mathbf{x}_j - \mathbf{x}_i)$ is the semivariance between the sampling locations \mathbf{x}_j and \mathbf{x}_i and $\gamma(\mathbf{x}_j - \mathbf{x}_0)$ is the semivariance between sampling location \mathbf{x}_j and the unsampled location \mathbf{x}_0 , obtained from the fitted variogram. The quantity ψ is the Lagrange multiplier introduced to minimize the ordinary kriging variance under the constraint of unbiasedness.

When the kriging equations are solved to obtain the weights w_i , the largest weight is in principle given to the measurements nearest to the point to be interpolated. The weights also

depend on the configuration of the sampling. The factors affecting the weights can be summarized as follows:

- (i) Near points carry more weight than distant ones. Their relative proportions depend on the positions of the sampling points and on the variogram: the larger the nugget variance, the smaller the weights of the measurements nearest to the unknown point.
- (ii) The relative weights of points also depend on the size of the circular or rectangular area around the unknown position from which the measurements are used with the interpolation: as the area increases, the weights of the nearest points decrease and those of the more distant points increase, until the weights become nearly equal.
- (iii) Clustered points carry fewer weights individually than isolated ones at the same distance.
- (iv) Measurement points can be screened by ones lying between them and the unknown position.

With the ‘Variogram Estimation and Spatial Prediction with Error’ (VESPER) program, theoretical variogram models were fit to the experimental global variograms before interpolating the data with OK (Minasny et al., 2005).

2.5 Geology and geomorphology of East- and West-Flanders

All study sites are situated in the western region of Flanders, in the provinces of West- and East-Flanders. The present soil landscapes of Flanders are mainly resulting from the geological processes which occurred during the Cenozoic (Tertiary and Quaternary periods).

During the early Eocene (55.0 Ma – 48.6 Ma), the western part Flanders was flooded by a calm sea. During this period, clayey and sandy layers were deposited. This 100 m thick glauconitic clay layer is called ‘Ypresian clay’. These clayey layers surface in the southern parts of West- and East-Flanders (Goossens, 1984; Maréchal, 1992).

The Quaternary period (2.6 Ma – present) was characterized by a succession of colder and warmer periods, called glacial and interglacial stages. During these glacial stages, the ice caps above the Arctic and Antarctic increased substantially in volume. During the second last glacial stage (Saalian, 238 000 – 128 000 year BP), the ice cap extended to Amsterdam (The Netherlands). Large volumes of water were withdrawn from the ocean for the ice caps to form, leading to drastic decreases of the sea level (up to 130 m below the present sea level). Due to this, the North Sea was dry. The rivers of Flanders, which all drained perpendicularly in the North Sea, eroded their own valleys. A large, oblong valley developed, with a 10 to 20

km wide east- west axis, called the ‘Flemish valley’. At the end of this glacial stage (130 000 years BP), the ice caps melted and the sea level rose. This caused the penetration of the sea in the Flemish valley and the subsequent sedimentation of sand and thin clayey layers of a few meter. During the last glacial stage (Weichselian, 116 000 – 11 500 year BP), the erosion process restarted due to the renewed development of ice caps and the consequent lowering of the sea level. The rivers, loaded with the eroded material, obstructed their own river-bed. 10 000 years BP, the rivers found a new way to mouth into the North Sea through the Lower-Scheldt via Antwerp.

During the glacial periods, high pressure areas developed above the extended ice caps. The resulting winds had free reign in the at that time dry North Sea, blowing away big volumes of fine soil particles. The finest (silty) particles carried the furthest (niveo-eolic), leading in the deposition of calcareous silt in the loess belt creating the silty region of Flanders (with a thickness up to 20 m) (Fig. 2.10). The largest particles were transported by saltation and sedimented closer to the North Sea, covering the Flemish valley to form the sand region of Flanders (thickness max 30 m). Particles of intermediate size were deposited in the sandy loam region (Ameryckx et al., 1995). It was assumed that the height was the main obstruction for the deposition of wind-blown material in the southern part of Belgium. The Weichselian cover shows a large variation in thickness. This cover is usually thin or even absent extent on steep slopes and convex relief forms and has a large vertical extent in river valleys (Flemish valley) and flat plateaus (silty region) (Maréchal, 1992).

The Belgian coastal plain is a polder area about 15-20 km wide with an extension in the western part of the plain along the river IJzer. The plain was created by embankment following post-glacial sea-level rise and is situated behind a belt of aeolian sand dunes (Baeteman, 1999; 2008; Baeteman and Declercq, 2002). Its particular microrelief results from both natural and man-induced processes. Sea-level rise at the onset of the Holocene initiated peat formation and sediment accumulation behind the coastal barrier. A decrease in sea-level rise starting around 7500 year BP caused increasing sedimentation in the newly formed tidal basin. As sea-level rise continued to drop ca. 5500-5000 year BP, the thickest peat layers accumulated, lasting until about 1500 year BP (Baeteman, 1991; 2008). Throughout the evolution of the coastal plain, tidal channels were formed in the peat layers and the underlying sediments, which in their turn were filled up by sandy and, in more recent systems, clayey sediments. Radiocarbon dating showed that these tidal channels were active until the 7th century (Ervynck et al., 1999).

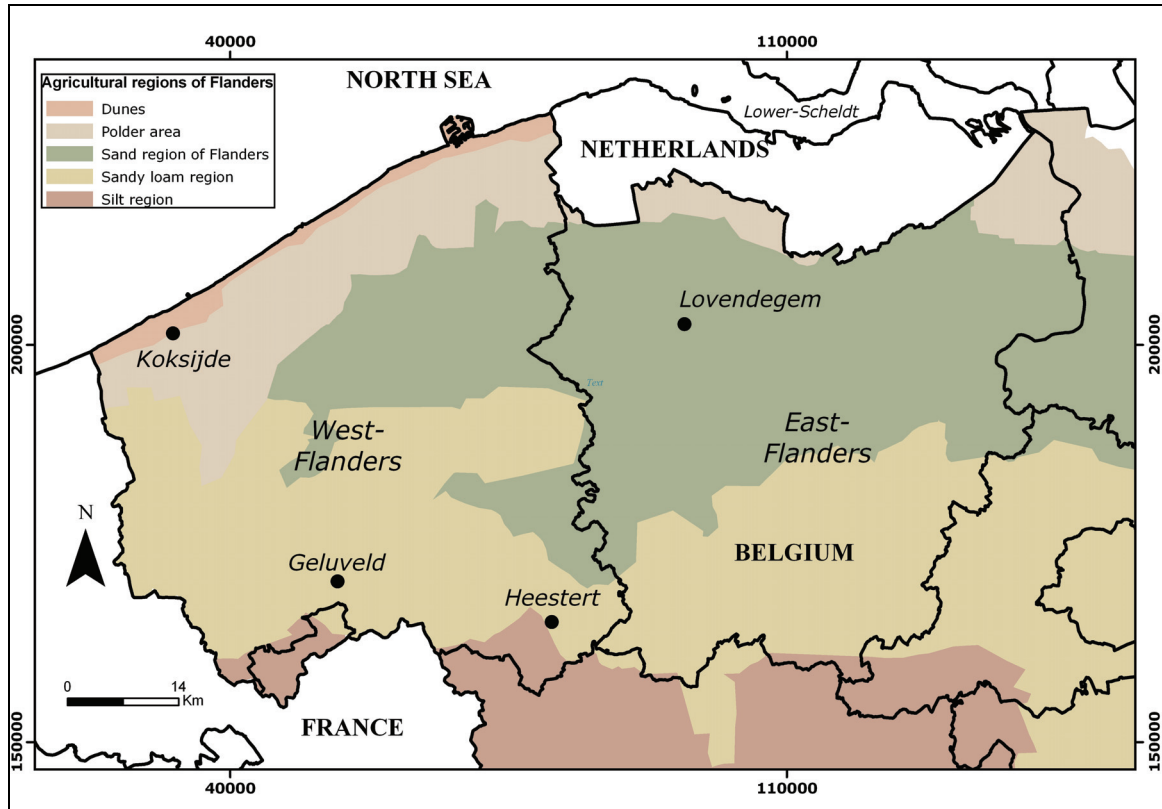


Fig. 2.10. Localization of the Lovendegem, Koksijde, Geluveld and Heestert study sites in the provinces of West- and East-Flanders and the agricultural regions of Flanders (coordinates are according to the Belgian metric Lambert 72 projection).

Chapter 3

A pedotransfer function to evaluate the soil profile textural heterogeneity¹

3.1 Abstract

Since soil texture is difficult to quantify, its determination is often restricted to the topsoil. To improve its mapping accuracy, observations of the apparent electrical conductivity (ECa) obtained from proximal soil sensors are increasingly being used due to its close relationship with soil texture under non-saline conditions. However, a single ECa measurement does not allow an unambiguous interpretation of both the topsoil texture and its vertical distribution, because of its bulk support over the entire profile. Therefore we selected 88 soil profiles with ‘pseudo-homogeneous’ textural composition from a database containing 1500 profiles with nine textural fractions and the organic matter content analysed for every horizon. These profiles were revisited and the ECa was measured with an EM38DD sensor. With these data we obtained the following pedotransfer function (PTF): $ECa_v = 16.2 + 1.314 \cdot Fr_{0-2,w}$, with $R^2 = 0.81$. This function allows converting a topsoil clay percentage into a reference ECa value measured with the vertical coil orientation (ECa_v), assuming standard temperature and moisture conditions and a dominance of mica clay minerals. The ratio between the observed ECa_v and this reference ECa_v value is a measure of the soil profile textural heterogeneity: if this ratio is near to one, the profile is quasi-homogeneous; a ratio exceeding one indicates the presence of more conductive material deeper in the soil profile, and *vice versa*. To explore this idea we considered an intensively surveyed area of 3000 km² in Belgium with a wide soil textural variation. Based on our PTF, a regional-scale topsoil clay map was converted into a reference ECa_v map which was found to be a valuable aid in evaluating the soil profile textural heterogeneity by field measured ECa_v data.

¹Modified from: Saey, T., Van Meirvenne, M., Vermeersch, H., Ameloot, N., Cockx, L., 2009. A pedotransfer function to evaluate soil profile heterogeneity using proximally sensed apparent electrical conductivity. *Geoderma*, 150: 389-395.

3.2 Introduction

The ability to characterize soil by its electrical properties has been studied intensively, originally to characterize mainly soil salinity under laboratory conditions (Richards et al., 1954). But also in non-saline soils, in-situ measurements of the apparent electrical conductivity were found to be highly informative, mainly with respect to investigating variations in clay and soil organic matter (SOM) contents (Corwin and Lesch, 2005; McCutcheon et al., 2006). The advantage of measuring ECa is the ability to operate with mobile and non-destructive proximal soil sensors based on electromagnetic induction (EMI) or electrical resistance (like the Veris 2000XA, Veris Tech., Salina, Kansas, USA). Both measurement principles integrate the response of a soil volume down to an effective depth, which typically extends to 1.2 – 1.6 m for agricultural purposes, depending on the inter-coil or inter-electrode distance (McNeill, 1980b, Sudduth et al., 2003).

The availability of mobile proximal soil sensors in combination with GPS referencing offers the opportunity to complement the limited density of direct soil samples, on which soil properties are analyzed in the laboratory, with high-resolution measurements reaching a density of one observation per m². Such a wealth of secondary information has triggered research about the creation of pedotransfer functions (PTF's) linking ECa with clay and/or SOM concentrations. Several studies report on such PTF's, mostly using a depth-weighted combination of soil properties (Domsch and Giebel, 2004; Sudduth et al., 2005). For EMI sensors this depth-weighting is based on the depth-sensitivity curve of McNeill (1980b).

At present, many countries possess coverage of soil maps, often with soil texture as a key variable, complemented with detailed soil databases. Institutions, like the European Commission or the UN-Food and Agriculture Organization, have contributed further in pooling and standardizing such databases (Nemes et al., 1999; Henderson et al., 2005). However, soil sampling of profile horizons is labour-intensive and therefore most soil studies focus on the topsoil only (Kerry and Oliver, 2007; Garten Jr. et al., 2007). It is our experience that the subsoil is often much more heterogeneous than the topsoil, both laterally and vertically, especially in arable land where the topsoil is regularly being mixed by tillage (Vitharana et al., 2006).

Our idea was to use the available and mapped topsoil properties and convert them by a PTF into reference ECa (ECa-ref) values assuming homogeneous soil textural conditions down to the measurement depth of ECa. These ECa-ref values could then be used to evaluate observed ECa (ECa-obs) values. Strong deviations in soil texture are likely to indicate a violation of the homogeneous profile assumption. In such a situation there is either a textural discontinuity (as

observed by e.g. Saey et al., 2008) or man-induced soil structure and/or texture mixing disturbances. Given the rapidly increasing coverage of ECa-measured land (some western countries have extensive programmes of ECa measurements to support precision agriculture), the availability of ECa-ref values would allow a more absolute evaluation of ECa-obs and could be used to direct additional sampling and verification activities more efficiently by targeting deviations in expected ECa values.

The goals of this study were: (1) to establish a PTF between topsoil properties of soil profiles with ‘pseudo-homogeneous’ textural composition and ECa, resulting in ECa-ref values; (2) to evaluate the ratio of ECa-obs to ECa-ref as a measure of the degree of soil profile textural heterogeneity; and (3) to apply this idea to a regional soil texture map to create a regional-scale map of ECa-ref values. As a case study the province of East-Flanders in Belgium was used because this area has a wide variability of topsoil texture which has been mapped quantitatively.

3.3 Soil texture database

The study was conducted over an area covering 3000 km² located in the north of Belgium: the province of East-Flanders (Fig. 3.1). Van Meirvenne and Van Cleemput (2005) found that within this province a large textural variability exists: 11 of the 12 textural classes of the USDA texture triangle are found (only the class 'sandy clay' is absent, Fig. 3.2).

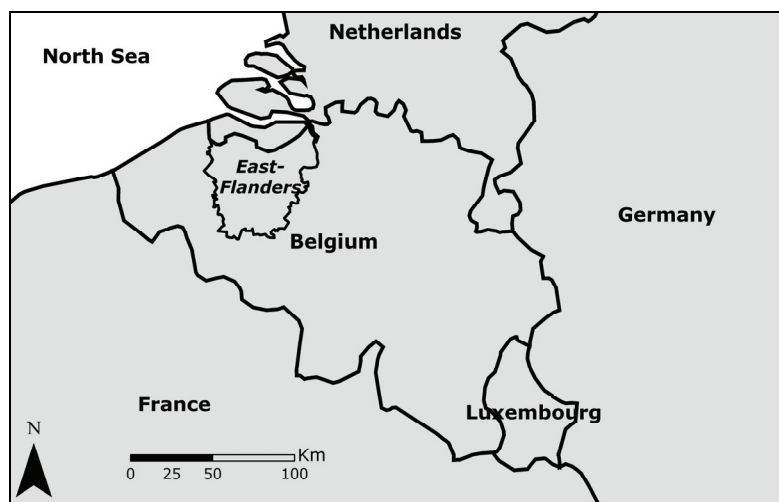


Fig. 3.1 Localization of the study area in Belgium.

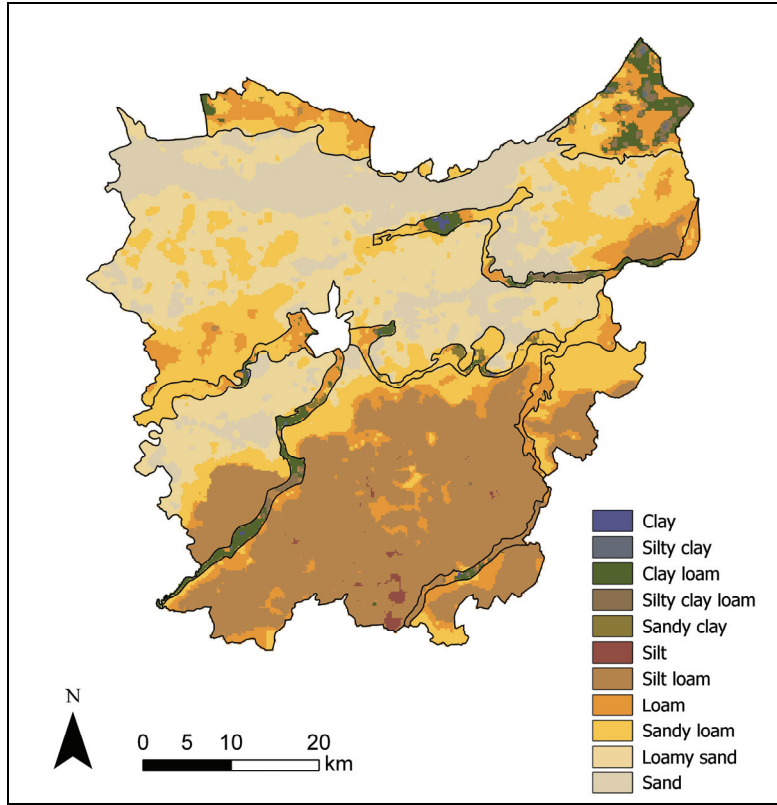


Fig. 3.2 Soil texture map of East-Flanders classified according to the USDA soil textural triangle (Van Meirvenne and Van Cleemput, 2005) (the city of Ghent was blanked).

During the Belgian soil survey, which was conducted between 1947 and 1973, 4887 topsoil (0 - 30 cm) locations were sampled and additionally 1500 soil profiles were dug down to 1.5 m and sampled per horizon within this area. All samples were analysed for soil texture using the conventional sieve-and-pipette method and split into nine fractions: 0-2 μm (Fr_{0-2}), 2-10 μm (Fr_{2-10}), 10-20 μm (Fr_{10-20}), 20-50 μm (Fr_{20-50}), 50-100 μm (Fr_{50-100}), 100-200 μm ($\text{Fr}_{100-200}$), 200-500 μm ($\text{Fr}_{200-500}$), 500-1000 μm ($\text{Fr}_{500-1000}$) and 1000-2000 μm ($\text{Fr}_{1000-2000}$). Also the soil organic matter (SOM) content was determined by the Walkley and Black method.

The ECa equivalent texture for the entire soil profile was obtained by weighting each horizon with the EM38 depth response curve according to the horizon boundaries. For example, the weighted clay content, $\text{Fr}_{0-2,w}$, over the total soil profile was obtained from:

$$\text{Fr}_{0-2,w} = \frac{\text{Fr}_{0-2,H_1} \cdot (R(z_1)) + \text{Fr}_{0-2,H_2} (R(z_2) - R(z_1)) + \dots + \text{Fr}_{0-2,H_n} (R(z_n = z_{\text{lower boundary}}) - R(z_{n-1}))}{R(z_n = z_{\text{lower boundary}})} \quad [3.1]$$

with z_i the depth of the lower boundary of horizon H_i ($i = 1, 2, \dots, n$), z_n the depth of the lower boundary of the deepest horizon of which textural data are available, Fr_{0-2,H_i} the clay content of horizon H_i and $R(z_i)$ the cumulative EM38 response from the soil above z_i . To relate $\text{Fr}_{0-2,w}$ to the apparent electrical conductivity measured with the sensor in the vertical orientation

(E_{Ca_v}), the vertical cumulative response function $R_v(z)$ (Eq. (2.9)) was used in Eq. (3.1). Similarly for the apparent electrical conductivity measured with the sensor in the horizontal orientation (E_{Ca_h}), Eq. (2.10) was used.

The lower boundary of the soil profile descriptions was mostly 1.5 m. However, the response of the measured ECa signal still has a contribution of the soil volume below 1.5 m. This is 32 % for the vertical and 16 % for the horizontal coil orientations, respectively (Fig. 2.7). Therefore, the relative response of each soil horizon between the depths z_1 and z_2 was calculated by dividing its response ($R(z_2) - R(z_1)$) by the total response from the top 1.5 m ($R(1.5 \text{ m})$) (representing 68 % and 84 % of the total ECa response, respectively).

3.4 Selection of soil profiles with ‘pseudo-homogeneous’ textural composition

To investigate the relationship between ECa and the soil textural composition, homogeneous soil profiles are required. Since texturally homogeneous soil profiles are extremely rare, we used a selection criterion to find profiles with ‘pseudo-homogeneous’ textural composition: the deviation in clay content (Fr_{0-2}) between the top- and subsoil horizons was set to be less than 10%. Out of the available 1500 profiles, only 88 met this criterion and Figure 3.3 shows their locations. Somewhat to our surprise these profiles were distributed over the entire province, which indicated a good level of aerial representation.

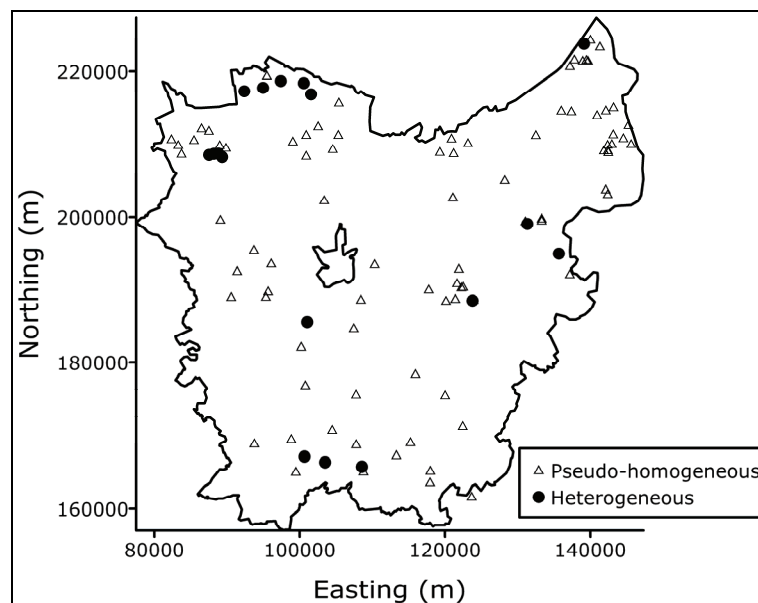


Fig. 3.3 Localization of the 88 soil profiles with ‘pseudo-homogeneous’ textural composition and 17 soil profiles with heterogeneous textural composition inside East-Flanders.

All of the 88 soil profiles with ‘pseudo-homogeneous’ textural composition were revisited and a pooled soil sample was taken by taking three samples from the top- and subsoil within a 2.5 m radius in respect to the reported coordinates of the National Soil Survey. These samples were air-dried to analyze the SOM content. The 88 locations were also classified into pasture or arable to account for the influence of recent land use on the SOM. This distinction was made because we expected clearly different SOM concentrations between them (no other land uses were visited).

Five profiles were selected to represent the different soil regions of the province. Their topsoil samples were analysed for the cation exchange capacity (CEC) by the ammonium-acetate method (Schollenberger and Simon, 1945). The CEC values ranged between 15.8 and 35.9 cmol(+) kg⁻¹ clay, with an average of 21.8 cmol(+) kg⁻¹ clay. These moderate CEC values all indicated by a dominance of mica (illite) clay minerals, typically having a CEC between 15 and 40 cmol(+) kg⁻¹ (Hillel, 1998).

3.5 ECa measurements

At each of the 88 revisited soil profiles with ‘pseudo-homogeneous’ textural composition, ECa was measured with an EM38DD soil sensor. To avoid instrument drift (Robinson et al., 2004) a precise calibration procedure was performed at each of these 88 locations. Six ECa measurements were taken by the manually operated EM38DD sensor within a small area of 2.5 m radius, both in the vertical and in the horizontal orientation. The mean of these six ECa_v and ECa_h measurements was attributed to the central coordinates of this location.

Since measurements were conducted under different field conditions, both ECa values were standardized to a temperature of 25°C, using the following temperature standardization equation (Slavich and Petterson, 1990):

$$ECa_{25} = ECa \cdot \left(0.447 + 1.4034 \cdot \exp\left(-\frac{T}{26.815}\right) \right) \quad [3.2]$$

with ECa₂₅ the standardized ECa at a temperature of 25°C and T the soil temperature in degrees Celsius measured at a depth of 20 cm at each location. The temperature standardization coefficients were considered to be insensitive to the exact depth of soil temperature measurements, as reported by Sheets and Hendrickx (1995).

To minimize the influence of strongly varying soil water content on the conductivity measurements, soil water tension was measured with mobile field tensiometers (Feldtensiometer, Umwelt Geräte Technik Müncheberg, Germany). At each of the 88 locations, three tensiometers were inserted to the depths 0.3, 0.6 and 0.9 m below the soil surface. Only when a near to or higher than field capacity moisture tension was observed,

E_{Ca} measurements were taken. Lower moisture contents were assumed to influence the E_{Ca} measurements substantially.

Table 3.1 provides the descriptive statistics of the particle size fractions of the 88 soil profiles with ‘pseudo-homogeneous’ textural composition as taken from the soil database weighted by the vertical response curve (hence the subscript ‘w’). Most textural fractions showed a large spread, except the very coarse sand fractions (> 500 µm) which contained rarely a few grains. The weighted clay fraction ranged from 0.2 to 56.5 % with a coefficient of variation (CV) of 94 %, which is quite large. The fraction with the largest CV (127 %) was the 200-500 µm fraction. The texture class which corresponded to the mean values of the three major textural fractions was loam (according to the USDA soil texture triangle), indicating the central positions of these mean values. The corresponding E_{Ca} measurements and SOM measurements showed also a large variation, although less than the textural fractions. The E_{Ca} values ranged from very low (5-9 mS m⁻¹) to values close to 100 mS m⁻¹. Their distributions had a CV between 62 and 68 % with the mean E_{Ca_v} value being slightly larger than the mean E_{Ca_h}. The SOM contents indicate rather moderate SOM contents, without the presence of e.g. boggy or peaty conditions.

Table 3.1 Descriptive statistics of profile weighted textural fractions (Fr.-.,_w) determined with the vertical response curve (Eq. 3.1) for the 88 soil profiles with ‘pseudo-homogeneous’ textural composition and the recently observed E_{Ca}’s and SOM (*m*: mean, *s*²: variance).

		min	max	<i>m</i>	<i>s</i> ²
E _{Ca_v}	(mS m ⁻¹)	9	106	39	581
E _{Ca_h}	(mS m ⁻¹)	5	97	32	487
Fr _{0-2,w}	(%)	0.2	56.5	17.5	272.0
Fr _{2-10,w}	(%)	0.0	19.0	5.6	22.9
Fr _{10-20,w}	(%)	0.0	15.5	6.5	23.3
Fr _{20-50,w}	(%)	1.1	64.4	25.4	305.5
Fr _{50-100,w}	(%)	1.6	44.1	18.3	97.6
Fr _{100-200,w}	(%)	0.2	70.3	22.7	575.2
Fr _{200-500,w}	(%)	0.1	23.1	4.0	26.0
Fr _{500-1000,w}	(%)	0.0	1.0	0.1	0.0
Fr _{1000-2000,w}	(%)	0.0	0.5	0.0	0.0
SOM (0 m - 0.3 m)	(%)	0.4	13.8	3.8	8.1

3.6 Pedotransfer function

The Pearson correlation coefficients between the E_{Ca} measurements and the weighted textural fractions and top SOM content are given in Table 3.2. A continuous sequence was found starting with the largest positive correlation with Fr_{0-2,w} (*r* = .899 with E_{Ca_v}), over weak

correlations with the silt fractions ($r = .199$ for $Fr_{20-50,w}$ with Ea_v) to a moderately large negative correlation with the sand fractions ($r = -.714$ for $Fr_{100-200,w}$ with Ea_v). As mentioned before the very coarse sand fractions were not found in all samples. Obviously, the compositional nature of soil textural fractions (they sum to 100 %) is linked to this observation: the more clay, the less silt and sand. So all these fractions can not be considered as independent variables. Aggregations of two or more fractions ($Fr_{0-10,w}$ and $Fr_{0-20,w}$) did not improve the correlation compared to the $Fr_{0-2,w}$ fraction. The SOM had a moderately strong correlation (0.652 with Ea_v). Similar results were found with Ea_h .

Table 3.2 Pearson correlation coefficients between the two Ea 's and the profile weighted textural fractions ($Fr_{-,w}$) and SOM content.

	<i>n</i>	Ea_v	Ea_h
$Fr_{0-2,w}$	88	.899**	.919**
$Fr_{2-10,w}$	88	.830**	.866**
$Fr_{10-20,w}$	88	.648**	.661**
$Fr_{20-50,w}$	88	.199	.135
$Fr_{50-100,w}$	88	-.500**	-.561**
$Fr_{100-200,w}$	88	-.714**	-.694**
$Fr_{200-500,w}$	88	-.644**	-.627**
$Fr_{500-1000,w}$	69	-.235*	-.233
$Fr_{1000-2000,w}$	12	-.230	.092
$Fr_{0-10,w}$	88	.894**	.917**
$Fr_{0-20,w}$	88	.881**	.901**
SOM (0 m - 0.3 m)	88	.652**	.702**

* Significant at 5 % level of significance

** Significant at 1 % level of significance

A multiple linear regression analysis was conducted using S-PLUS (Insightful Corporation, Seattle, USA) to identify the best linear combination of predictors (weighted textural fractions and top SOM) that correlate maximally with the predicted variable, i.e. Ea_v . We used a stepwise removing procedure where the least influencing predictor variable was removed in turn. However, the compositional nature of the textural fractions violates the assumption of independent variances and covariances which could result in a bias (Duffera et al., 2007). Therefore we decided to exclude the sand fractions ($> 50 \mu m$) from the multiple linear regression analysis (Vitharana et al., 2008b). So our starting model contained the following variables:

$$Ea_v = \beta_0 + \beta_1 \cdot Fr_{0-2,w} + \beta_2 \cdot Fr_{2-10,w} + \beta_3 \cdot Fr_{10-20,w} + \beta_4 \cdot Fr_{20-50,w} + \beta_5 \cdot SOM + \varepsilon$$

[3.3]

with β_i the coefficient of the i^{th} predictor variable ($i = 1, \dots, 5$) and ε the difference between the predicted and observed value of ECa_v . A similar analysis was conducted for ECa_h .

The 88 soil profiles were split in two classes: the arable fields (53 profiles) and the pasture fields (35 profiles) to account for the effect of land use on the SOM content.

For ECa_v both land use types resulted in only one significant predictor variable: $\text{Fr}_{0-2,w}$. Therefore both land use classes were pooled. This resulted in the PTF for ECa_v :

$$\text{ECa}_v = 16.2 + 1.314 \cdot \text{Fr}_{0-2,w} \quad [3.4]$$

with a R^2 of 0.81 and a residual standard error of 10.6 mS m^{-1} . Table 3.3 provides some of the fitting parameters of this model.

Table 3.3 Fitting parameters the regression model for ECa_v (Eq. 3.4) obtained with the stepwise multiple linear regression analysis (s : standard error; t : Student's- t -test of significance, p : probability level).

	Value	s	t -Statistic	p -Value
Intercept	16.2	1.7	9.814	0.0000
$\text{Fr}_{0-2,w}$	1.314	0.069	19.091	0.0000

For ECa_h besides $\text{Fr}_{0-2,w}$ also the land use specific SOM was identified as a significant variable:

$$\text{ECa}_h = 7.2 + 1.098 \cdot \text{Fr}_{0-2,w} + 1.494 \cdot I_1 \cdot \text{SOM} + 1.339 \cdot (1 - I_1) \cdot \text{SOM} \quad [3.5]$$

where:

$$I_1 = \begin{cases} 1 & \text{if landuse} = \text{arable} \\ 0 & \text{if landuse} = \text{pasture} \end{cases}$$

with a R^2 of 0.86 and a residual standard error of 8.4 mS m^{-1} . The fitting parameters are given in Table 3.4.

Table 3.4 Fitting parameters the regression model for ECa_h (Eq. 3.5) obtained by the stepwise multiple linear regression analysis (s : standard error; t : Student's- t -test of significance, p : probability level).

	Value	s	t -Statistic	p -Value
Intercept	7.2	1.8	3.886	0.0002
$\text{Fr}_{0-2,w}$	1.098	0.075	14.724	0.0000
SOM if arable	1.494	0.755	1.980	0.0510
SOM if pasture	1.339	0.430	3.113	0.0025

So for both ECa variables, the $\text{Fr}_{0-2,w}$ was found to be the most important variable explaining 81 % of the variability of the ECa_v signal (Fig. 3.4). Due to its stronger response to the topsoil (recall Fig. 2.7), the prediction of ECa_h requires, besides $\text{Fr}_{0-2,w}$ also knowledge of the topsoil

SOM content (and land use type). Both variables succeed in explaining 86 % of the variation in ECa_h . However, to evaluate the soil profile textural heterogeneity or between the top- (0 m – 0.3 m) and subsoil (0.3 m – 1.5 m), we focussed on ECa_v . Moreover this variable is independent from land use.

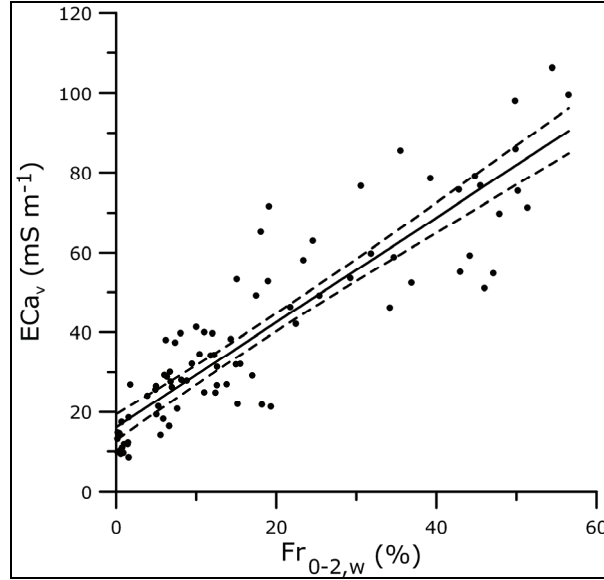


Fig. 3.4 The 88 measurements of ECa_v of the 'pseudo-homogeneous' soil profiles and the profile weighted clay contents, $Fr_{0-2,w}$, with the fitted regression $ECa_v = 16.2 + 1.314 \cdot Fr_{0-2,w}$ (full line) and its 95 % confidence interval (dashed curves).

3.7 Identifying the soil profile textural heterogeneity with reference ECa_v values

Eq. 3.4 can be used to convert topsoil Fr_{0-2} measurements into reference ECa_v values (ECa_{ref}), assuming the soil texture to be homogeneous over the entire profile. These values can then be compared with measured ECa_v values (ECa_{obs}) to evaluate the soil profile heterogeneity in terms of soil texture.

To evaluate the value of our PTF, we selected 17 soil profiles with subsoil Fr_{0-2} values differing more than 10 % from the topsoil Fr_{0-2} from our database of East-Flanders. Their locations are indicated on Fig. 3.3. At these 17 locations, the ECa_v was measured in the same way as at the 88 soil profiles with 'pseudo-homogeneous' textural composition. These ECa_{obs} values are given in Table 3.5 together with the ECa_{ref} values obtained from their topsoil Fr_{0-2} which was input in Eq. 3.4. Eleven ECa_{obs} values exceeded the ECa_{ref} and six were smaller. We propose to use the ECa ratio, defined as $ECa_{obs} \cdot (ECa_{ref})^{-1}$, as a measure of the soil profile textural heterogeneity (Table 3.5). An ECa ratio of 1 would theoretically imply a

perfectly homogeneous profile, a value exceeding one would indicate a subsoil with more conductive material (e.g. more clay), whereas an ECa ratio smaller than one would indicate the inverse. Moreover, the magnitude of the ECa ratio could indicate the degree of soil profile textural heterogeneity, as the Fr_{0-2} profiles given in Fig. 3.5 show. The 17 heterogeneous profiles were grouped into three classes according to their ECa ratio. Fig. 3.5(a) shows the Fr_{0-2} analysed in the five profiles with an ECa ratio > 2.0 . These high ratios were associated with a very strong abrupt increase in Fr_{0-2} of at least 40 % within the top 1.2 m compared to the topsoil. These profiles contained a textural discontinuity. The six profiles in Fig. 3.5(b) had an ECa ratio between 1.0 and 2.0, which were caused by either a continuous gradual increase of Fr_{0-2} with increasing soil depth or a strong increase below 1.2 m or one subsoil horizon of limited thickness with a moderate increase in Fr_{0-2} within 1.2 m. The seven profiles of Fig. 3.5(c) had an ECa ratio smaller than 1. In all profiles the Fr_{0-2} remained stable to some depth below which it decreased. Clearly the ECa ratio was influenced by both the magnitude of change and the depth profile of Fr_{0-2} . Nevertheless the 17 examples showed the potential of the ECa ratio to evaluate the soil profile textural heterogeneity of a location with a single topsoil Fr_{0-2} determination and a few ECa_v measurements.

Table 3.5 Comparison between ECa-obs and ECa-ref and their ratio of 17 soil profiles with heterogeneous textural composition.

ECa-obs (mS m ⁻¹)	ECa-ref (mS m ⁻¹)	ECa ratio -
69.4	22.1	3.14
58.5	19.2	3.04
57.7	21.3	2.71
43.5	20.3	2.15
63.8	31.5	2.03
66.9	35.9	1.86
76.6	44.0	1.74
31.8	22.5	1.42
85.1	62.3	1.37
51.7	39.3	1.32
91.5	70.0	1.31
35.4	36.9	0.96
37.4	43.5	0.86
29.3	35.0	0.84
34.0	41.5	0.82
42.2	53.8	0.77
28.6	53.8	0.53

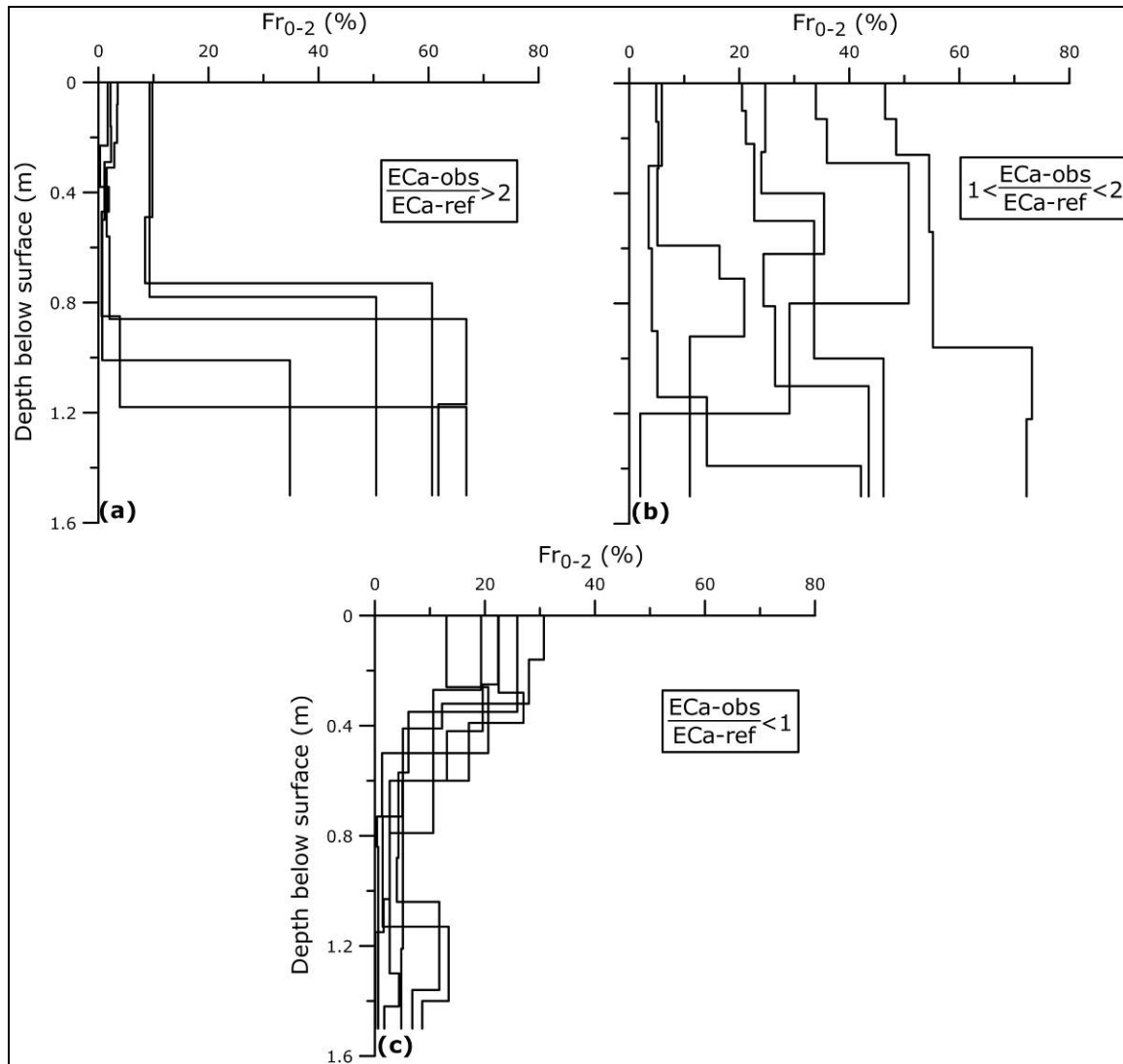


Fig. 3.5 Fr₀₋₂ as a function of the depth below the surface for the 17 soil profiles with heterogeneous textural composition classified on the base of their $ECa-obs \cdot (ECa-ref)^{-1}$ ratio: 5 profiles have a ratio larger than 2 (a) 6 profiles have a ratio between 1 and 2 (b) and 6 profiles have a ration smaller than 1.

3.8 A regional ECa-ref map

Van Meirvenne and Van Cleemput (2005) used 4887 topsoil samples to map the Fr₀₋₂, Fr₂₋₅₀ and Fr₅₀₋₂₀₀₀ fractions of the province of East-Flanders, Belgium, using stratified compositional block kriging with variogram stratification (Boucneau et al., 1998). The seven strata used were taken from a generalized 1/100,000 soil texture map and represented the major soilscares of the province. Compositional kriging was used to ensure that the three textural fractions summed to 100 % within each interpolated block. This was done by simultaneously minimizing the sum of the prediction error variances taking the unbiasedness, non-negativity and constant sum constraints into account into the kriging system (Walvoort

and De Gruijter, 2001). The block size was 250 m by 250 m. Fig. 3.2 shows these results classified according to the USDA soil textural triangle.

We converted the topsoil Fr_{0-2} data into an ECa-ref map (Fig. 3.6) by applying our PTF (Eq. 3.4). A large spread in ECa-ref values was found due to the large differences in topsoil Fr_{0-2} across the study area. High ECa-ref values ($> 45 \text{ mS m}^{-1}$) were attributed to the two polder areas in the north, the alluvial rims of rivers and where Tertiary clayey sediments surface (visible as locally increased values in south-eastern part). In the silty and sandy loam areas (central to southern parts), moderate ECa-ref values ($25 - 45 \text{ mS m}^{-1}$) were mapped, while low ECa-ref values ($< 25 \text{ mS m}^{-1}$) were associated with the fine and medium sand areas covering most of the northern half of the province.

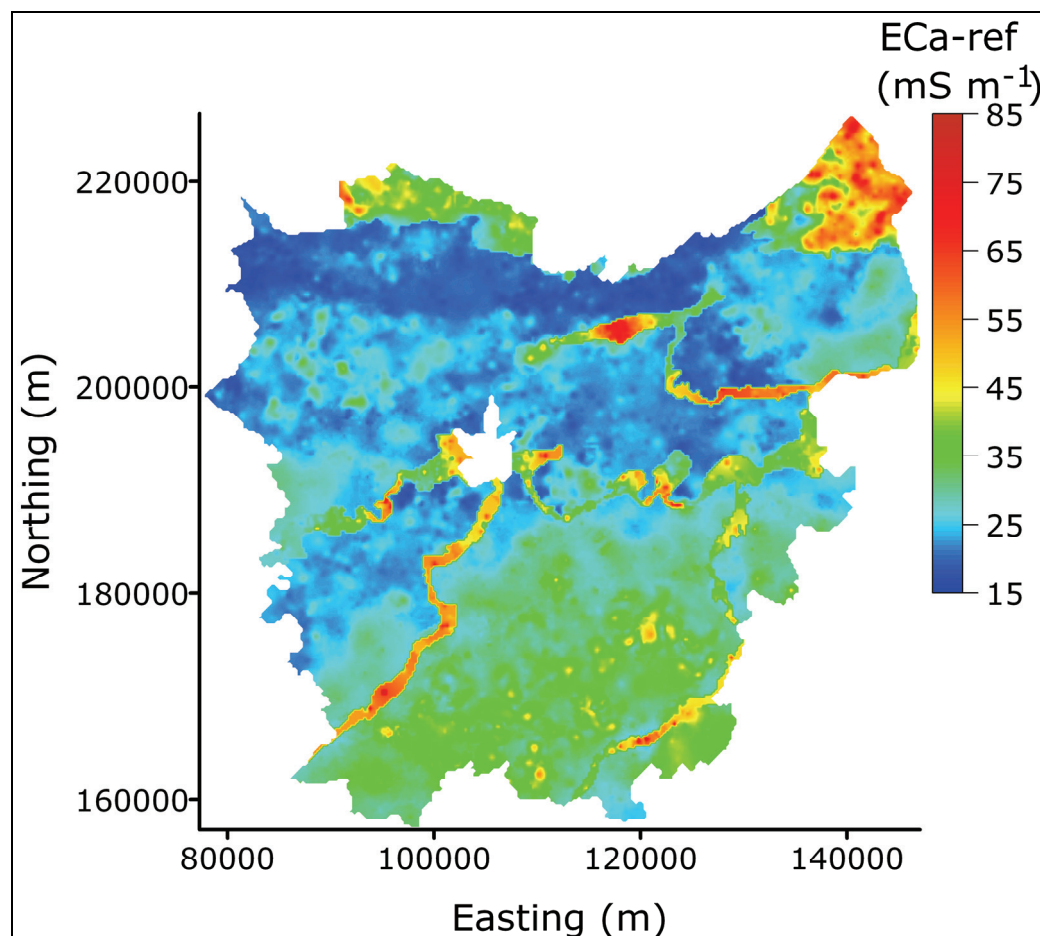


Fig. 3.6 ECa-ref of the province of East-Flanders, Belgium.

We found this map to be a valuable aid in evaluating field-measured ECa values, which are increasingly becoming available. By using the ECa ratio a measure of the soil profile textural heterogeneity compared to the topsoil texture is provided.

3.9 Conclusions

We concluded that:

1. Out of the nine textural fractions considered, as well as some combinations thereof, and the SOM content, Fr_{0-2} is the variable which is most strongly related to both E_{Ca_v} and E_{Ca_h} .
2. A multiple regression analyses indicated that E_{Ca_v} was best predicted by Fr_{0-2} , while E_{Ca_h} was best predicted by a combination of Fr_{0-2} , the topsoil SOM content and the land use type. Therefore E_{Ca_v} is found to be more suitable to evaluate the soil profile textural heterogeneity because the Fr_{0-2} fraction was routinely determined during soil surveys and can be considered to be reasonably stable over time, independent from land use.
3. A PTF is proposed to relate E_{Ca_v} and the Fr_{0-2} fraction:

$$E_{Ca_v} = 16.2 + 1.314 \cdot Fr_{0-2,w}$$

with $R^2 = 0.809$ and a residual standard error of 10.6 mS m^{-1} .

4. This PTF allows to obtain reference E_{Ca_v} values at a temperature of 25°C and at field capacity moisture conditions from a determination of the topsoil Fr_{0-2} content assuming that the clay mineralogy is dominantly mica (with a CEC between 15 and $40 \text{ cmol}(+) \text{ kg}^{-1}$ clay).
5. The E_{Ca-ref} values can be combined with measured E_{Ca} values into an E_{Ca} -ratio which can be used as an indication of the soil profile heterogeneity, either due to a textural variability or due to a man-induced disturbance. This E_{Ca} ratio is influenced by both the magnitude of change and the depth profile of Fr_{0-2} . This shows the potential of evaluating the soil profile textural heterogeneity of a location with a single topsoil Fr_{0-2} determination and a few E_{Ca_v} measurements.
6. The E_{Ca-ref} values can be mapped by converting existing soil texture maps using our PTF. These maps provide a guide in evaluating field measured E_{Ca_v} values in respect to the soil profile textural heterogeneity, but their value depends on the quality of the soil textural inventory and is subject to the model uncertainty of our PTF.

We provided a study case where these findings were used to create a reference E_{Ca} map showing realistic E_{Ca-ref} values with a range which was far beyond the standard error of the PTF model. This map was found to be valuable in supporting the evaluation of E_{Ca_v} field surveys, which are increasingly becoming available.

Chapter 4

Reconstructing the paleotopography beneath the loess cover¹

4.1 Abstract

During the last glacial period (Weichselian), wind-blown loess was deposited over the undulating landscape of central Belgium, which had been formed in surfacing Tertiary marine sediments. Since valleys were filled up with a thicker loess layer than hill tops, the present topography is much smoother. This smoothing was enhanced by subsequent erosion processes. Reconstructing the paleolandscape at a detailed scale is almost impossible by conventional procedures based on soil augerings. Therefore, the use of the electromagnetic induction sensor, EM38DD, was evaluated as an alternative for mapping the depth to the Tertiary clay substrate. On our 2.7 ha study site, located in the loess belt of central Belgium, a strong non-linear relationship ($R^2 = 0.86$) was found between the apparent electrical conductivity, measured by the vertical dipole orientation of the EM38DD (ECa_v) and the depth to a Tertiary clay substrate. These predictions were validated by independent observations of the depth to the Tertiary clay and a correlation coefficient of 0.83, with an average error of 0.22 m, was found. So, our dense ECa measurements (2 by 2 m resolution) allowed us to build a three-dimensional surface of the depth to the Tertiary substrate, reconstructing the paleotopography beneath the loess cover. This paleotopography revealed distinct erosion patterns on the surface of the Tertiary clay. The continuity of these was confirmed by an analysis of surface flow patterns conducted on the reconstructed paleotopography. The non-invasive, time- and cost-effective electromagnetic induction sensor was found to offer new perspectives to reconstruct and analyse in detail the Quaternary paleotopography beneath the loess cover.

¹Modified from: Saey, T., Simpson, D., Vitharana, U., Vermeersch, H., Vermang, J., Van Meirvenne, M., 2008. Reconstructing the paleotopography beneath the loess cover with the aid of an electromagnetic induction sensor. *Catena*, 74: 58-64.

4.2 Introduction

The loess belt of Central Europe extends from the Atlantic coast, through central Belgium, to Eastern Europe. During the last glacial period (Weichselian), the periglacial undulating landscape of central Belgium had been formed in surfacing Tertiary marine sands and clays. This paleolandscape was covered by niveo-aeolian loess, with a thickness ranging from only a few decimeters on hill tops up to several tens of meters in valleys (Gillijns et al., 2005). As a consequence, the paleotopography was strongly smoothed and since slope processes have modified the thickness of the loess layer further, the paleotopography cannot be reconstructed on the basis of the present topography. The world's major loess deposits have correctly been linked to glacial processes or to cold weathering processes (Iriondo and Kröhling, 2007). Yet, a precise and accurate representation of landforms and niveo-aeolian loess sediments offers fundamental information about Pleistocene periglacial environments (Smith et al., 2006).

Geomorphological mapping, particularly at large scales (1:10,000 or greater) is one of the most important techniques in Quaternary research with the aim at analyzing glacial landscapes, including those resulting from the passage of the last ice sheets and particularly from more recent phases of glacier activity (Lowe and Walker, 1997). However, traditional geomorphological mapping needs to adapt to challenges for greater precision and objectivity within a GIS environment (Gustavsson et al., 2006). Leverington et al. (2002) digitally reconstructed late Quaternary landscapes by using a GIS method that subtracted interpolated isobase values from modern elevations. These maps served for the reconstruction of the Quaternary landscape on a large scale and with a limited accuracy. Therefore, quantifications of the subtle changes in paleotopography could not be made.

The extent to which conventional invasive methods can be employed for the quantification of the small-scale soil variability is often limited by the availability of expertise and the expense and labour associated with obtaining soil samples by augering (Stroh et al., 2001). Non-invasive geophysical methods (like seismic, geo-electric and electromagnetic) have proven to be effective for investigating the stratigraphy over relatively large depths (20-80 m) (Bersezio et al., 2007; Sass, 2007; Sloan et al., 2007). While geophysical investigations focus on the exploration of natural resources, hydrogeology or engineering purposes, knowledge about the applicability in shallow (< 3 m) subsurface exploration for geomorphologic purposes is still incomplete (Sass, 2007). To investigate the soil constitution over shallower depths, soil-adapted geophysical sensors, like the EM38DD, have proved their functioning (Boll et al., 1996; Sudduth et al., 2003; Cockx et al., 2006; Cockx et al., 2007).

With the low-frequency EM38DD sensor, high-resolution ECa measurements can be achieved in a cost- and labour-effective way. Soil ECa relates to a number of soil properties, including soil porosity, soil moisture content, concentration of dissolved electrolytes in the soil water, soil temperature and the amount and composition of colloids (McNeill, 1980a). In non-saline soils, like at the study site, ECa reflects mainly differences in clay and moisture content (Domsch and Giebel, 2004; McBratney et al., 2005). This makes the ECa measurements appropriate to account for differences in depth-to-clay layers (Doolittle et al., 1994; Sudduth et al., 2003; Cockx et al., 2007) based on the conductivity contrasts between topsoil and subsoil material.

The objective of this study was to evaluate a methodology for mapping the paleotopography at shallow depths (< 3 m) beneath the loess cover using the EM38DD electromagnetic induction (EMI) sensor. Therefore, a relationship between the paleotopography and the apparent electrical conductivity (ECa), measured by the EM38DD sensor, had to be found and validated. As a test case, a study site of 2.7 ha in central Belgium was used where the paleolandscape prior to the deposition of the loess cover was formed in Tertiary marine clay.

4.3 Geology

The Belgian loess belt, which is part of the large European loess belt, is characterized by a gentle rolling landscape, where Tertiary marine sandy and clayey deposits were covered by a Quaternary loess layer (Vanwalleghem et al., 2005). Generally, the thickness of the loess cover varies with the position in the landscape. Thin loess deposits (sometimes as thin as a few decimetres) can be found on the ridges, while in depressions thick loess deposits (of several tens of meters) can occur. The main sedimentation phase of the Quaternary loess was in the Weichselian glacial stage of the Late Pleistocene (80 ka - 10 ka) (Lowe and Walker, 1997).

The Tertiary material located directly below the Quaternary loess is composed of a range of marine depositions dating from the Early Eocene (55.0 Ma – 48.6 Ma), generally with a clayey or sandy constitution. Within the study area this layer belongs to the clayey variant of the Ypresian (Maréchal and Laga, 1988).

4.4 Study site

The research site was located in Heestert (southeast of the province of West-Flanders, Belgium), situated in the Belgian loess belt (Fig. 4.1). It was situated on a southeast facing hillside with an average slope of 7 % and an elevation ranging between 30 to 40 m above sea level (a.s.l.). The site consisted of two neighbouring fields. Field 1 was a 2 ha arable parcel (with central coordinates: 50°47'58"N, 3°24'41"E), with a sugar beet (*Beta vulgaris* L.) - winter wheat (*Triticum aestivum* L.) rotation. This field was used to calibrate and validate the relationship between *ECa* and the depth to the Tertiary substrate, observed after soil augering. Field 2 was a permanent pasture of 0.7 ha, located next to the eastern boundary of field 1 (with central coordinates: 50°47'01"N, 3°24'46"E). This field was added to reconstruct the paleotopography beyond the boundaries of the calibration field.

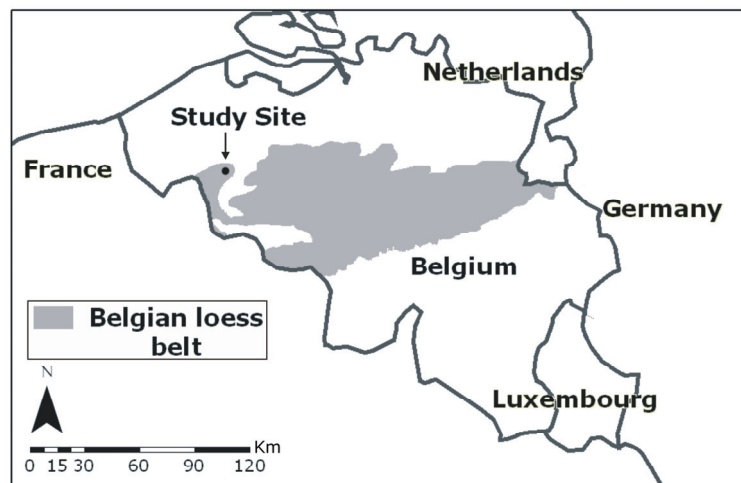


Fig. 4.1 Localization of the study site in the Belgian loess belt.

On the national soil map (scale 1:20 000) one dominant soil series (uLdc) is indicated for both fields. These symbols represent: a shallow (< 75 cm) clay substrate (u), a silt loam topsoil texture (L), moderately wet conditions (d) with a strongly degraded textural B-horizon (c). In the southern part of field 1 the shallow clay substrate was not indicated. This soil type corresponds to a Luvisol (WRB), which is characterized by an argic horizon ranging from 0.3-0.35 m up to 1.3-1.4 m in depth. Initially, the deposited loess was calcareous, but with time it decalcified, mostly down to a depth of 2-2.5 m (Hubert, 1976).

Across the study site, soil samples were taken from the Quaternary loess and the Tertiary clay substrate and analyzed for their textural composition according to the conventional sieve-pipette method. The mean clay-silt-sand fractions (with boundaries 2-50-2000 μm ,

respectively) of both the 23 Quaternary and the 17 Tertiary samples are given in Table 4.1, together with their standard deviations. On average, the loess layer has a larger sand content (32.0 %) and a lower clay content (19.1 %) than the Tertiary material (6.5 % sand and 40.2 % clay). Both layers show a relatively limited variability in soil texture, but the Tertiary clay layer is more homogeneous than the loess. These differences illustrate the relative easiness for an experienced soil scientist to distinguish between both layers in the field.

Table 4.1 Average textural composition of the Quaternary loess and Tertiary substrate based on samples taken along transect ABCD (*n*: number of samples, *m*: mean, *s*: standard deviation)

	<i>n</i>	Clay (%)		Silt (%)		Sand (%)	
		<i>m</i>	<i>s</i>	<i>m</i>	<i>s</i>	<i>m</i>	<i>s</i>
Quaternary loess	23	19.1	6.8	48.9	9.0	32.0	11.4
Tertiary substrate	17	40.2	8.0	53.3	7.2	6.5	5.6

4.5 ECa mapping

Table 4.2 shows the summary statistics of the EM38DD measurements for both fields. The mean of the ECa_v measurements of both fields (91 mS m⁻¹) was much larger compared to the ECa_h measurements (48 mS m⁻¹). This indicates that, in general, higher conductive soil is located below less conductive material. The standard deviations were the largest for field 1, indicating that this field was more heterogeneous in soil composition.

Table 4.2 Descriptive statistics (*m*: mean, *min*: minimum, *max*: maximum, *s*: standard deviation) of ECa_v, and ECa_h for the two fields (field 1 contained 5509 measurement points, field 2 contained 1814 measurement points).

Variable	Field 1				Field 2			
	<i>m</i>	min	max	<i>s</i>	<i>m</i>	min	max	<i>s</i>
ECa _v (mS m ⁻¹)	91	49	144	21	91	68	110	11
ECa _h (mS m ⁻¹)	48	19	100	15	48	32	72	7

Since the absolute values of ECa measured under different cultivation or soil moisture conditions could not be compared directly, measurements (already standardized at 25 °C) of adjacent fields had to be rescaled to a common basis. Therefore the ECa values located near to the boundary between field 1 and field 2 were matched using a nearest neighbour search within a moving window with a radius of 7 m centred at each point of field 2. The ECa_v of pairs of neighbours located in the opposite field were plotted in Fig. 4.2 and the following linear regression was fit to them:

$$ECa_{v_field1} = 1.50 \cdot ECa_{v_field2} - 25.85 \quad R^2 = 0.87$$

[4.1]

Using this relationship, ECa_v values of the entire second field were converted to a common basis with field 1 and these data were used in the remainder of this chapter.

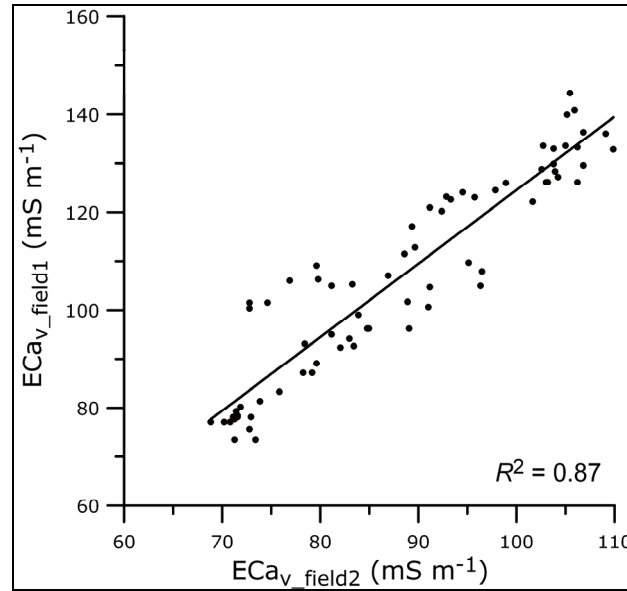


Fig. 4.2 ECa_{v_field1} as a function of ECa_{v_field2} (72 data points at the boundary of both fields).

The ECa_v measurements of both fields were interpolated as shown in Fig. 4.3. The variogram parameters are defined in Table 4.3. It can be seen that the highest ECa_v values occurred in the northern and in the southeastern parts of the study area. Moreover, the conversion to a common basis of the measurements of both fields resulted in a close match and a continuity beyond the boundary between both fields.

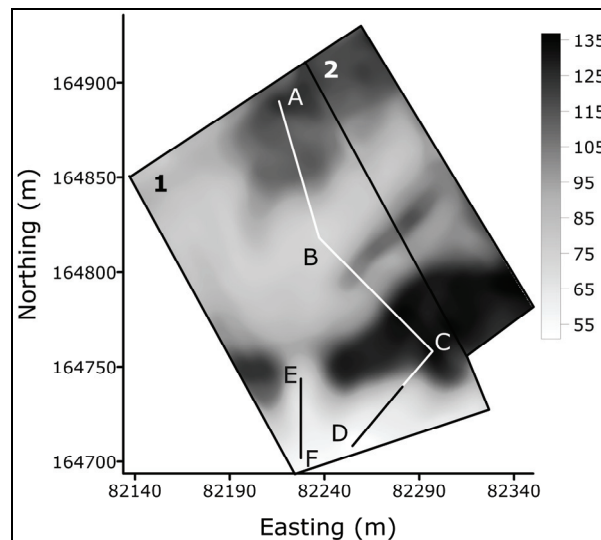


Fig. 4.3 Map of interpolated ECa_v ($mS\ m^{-1}$) with transects ABCD and EF.

Table 4.3 Parameters of the Gaussian variogram model for ECa_v , current elevation (Z), elevation of the Tertiary surface ($Z - z_{clay}^*$) and predicted depth-to-clay (z_{clay}^*). (C_0 : nugget variance; C_1 : sill and a : range)

Variable	C_0	C_1	a (m)
ECa_v ($mS\ m^{-1}$)	5	446	29
Z (m)	0.0	7.7	129
$Z - z_{clay}^*$ (m)	0.005	23.005	150
z_{clay}^* (m)	0.003	0.353	30

4.6 Depth observations

Two transects ABCD and EF were laid out in such a way that both the largest and lowest ECa measurements of field 1 were visited equally (Fig. 4.3). Along the 225 m of transect ABCD 46 observation points were located at 5 m intervals, while along the 42 m of transect EF 15 points were selected at 3 m intervals. At each of these 61 points, the depth to the Tertiary clay (z_{clay} or expressed as depth-to-clay) was observed by augering with a gouge auger.

Fig. 4.4(b) shows z_{clay} with respect to elevation together with the present day soil surface for transect ABCD. At most locations, a clearly observable distinction was present between the loess topsoil and the Tertiary clay. However, between points B and C, a mixture of loess-clay was found on top of the clayey substrate at some locations. This mixture was maximally about 0.5-0.6 m thick. Along this transect, the Tertiary clay substrate was present within the first 1.6 m at the first 42 sampling points. The last four sampling points on transect ABCD were characterized by a loess layer that extended down to more than 3.5 m, which was the maximal augering depth. At 14 observation points along transect EF, the Tertiary substrate was located between 1.5 and 3 m below the soil surface. The exact z_{clay} of the remaining sampling point was unavailable, due to the extent of the loess cover below the 3.5 m boundary.

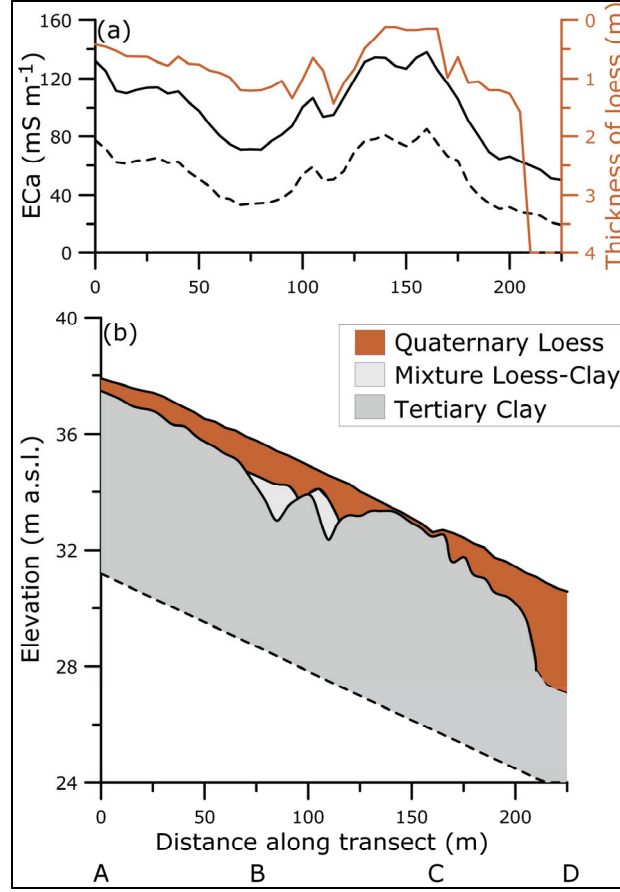


Fig. 4.4 ECa_v and ECa_h measurements and thickness of the loess along the 225 m transect ABCD (a) and the build-up of the three layers encountered along this transect (b).

4.7 Fitting

In a two-layered model where silty soil (like loess) is located above clayey material, the relationship between the depth to the clay substrate (z_{clay}) and the ECa_v can be modelled by using the McNeill (1980b) cumulative response $R_v(z_{clay})$ from the soil above z_{clay} (Eq. (2.9)). The cumulative response from the upper Quaternary loess and the lower Tertiary clayey material can be calculated as $R_v(z_{clay})$ and $1 - R_v(z_{clay})$, respectively. Therefore, at each z_{clay} , the corresponding ECa_v^* can be modelled given the apparent conductivity values of homogeneous Quaternary loess ($EC_{v,loess}$) and Tertiary clay ($EC_{v,clay}$):

$$ECa_v^* = [R_v(z_{clay})] \cdot EC_{v,loess} + [1 - R_v(z_{clay})] \cdot EC_{v,clay} \quad [4.2]$$

Inversely, z_{clay}^* can be modelled given the ECa_v measurements. Therefore, $R_v(z_{clay}^*)$ was calculated given the ECa_v measurements, $EC_{v,loess}$ and $EC_{v,clay}$:

$$R_v(z_{clay}^*) = \frac{ECa_v - EC_{v,clay}}{EC_{v,loess} - EC_{v,clay}} \quad [4.3]$$

This calculated $R_v(z_{clay}^*)$ can be input to Eq. (2.9) to obtain the modelled z_{clay}^* .

$$z_{\text{clay}}^* = \left[\frac{1}{4 \cdot (1 - R_v(z_{\text{clay}}^*))^2} - \frac{1}{4} \right]^{0.5} \quad [4.4]$$

To fit a theoretical relationship to the z_{clay} - ECa_v data points based on the McNeill (1980b) cumulative depth response, the sum of the squared differences between z_{clay} and z_{clay}^* must be minimized:

$$\sum_{i=1}^n [z_{\text{clay}}(i) - z_{\text{clay}}^*(i)]^2 = \min \quad [4.5]$$

with i the number of the observation and n the total amount of observations. z_{clay}^* was modelled with Eqs. (4.3) and (4.4) given the ECa_v measurements. The modelling parameters $\text{EC}_{v,\text{loess}}$ and $\text{EC}_{v,\text{clay}}$ were iteratively adjusted to obtain the smallest sum of the squared differences between z_{clay} and z_{clay}^* .

A similar approach can be followed to fit the theoretical relationship according to McNeill (1980b) to the z_{clay} - ECa_h data given the cumulative response $R_h(z_{\text{clay}})$ from the soil below a depth of z_{clay} (Eq. (2.10)).

After modelling z_{clay}^* given the ECa measurements, an independent validation can be executed to evaluate the model performance. Three validation indices were used as validation criteria: the mean estimation error (MEE), the root mean-squared estimation error (RMSEE) and the Pearson correlation coefficient r . The MEE and RMSEE were obtained from:

$$\text{MEE} = \frac{1}{n} \sum_{i=1}^n [z_{\text{clay}}^*(i) - z_{\text{clay}}(i)] \quad [4.6]$$

$$\text{RMSEE} = \sqrt{\frac{1}{n} \sum_{i=1}^n [z_{\text{clay}}^*(i) - z_{\text{clay}}(i)]^2} \quad [4.7]$$

with i the number of the validation observation and n the total amount of validation observations. The MEE is a measure of the bias and accuracy while the RMSEE accounts for the precision of the predictions. They should approach zero as the model predictions become optimal. An r value close to one indicates a strong positive linear relationship between observed and predicted depths.

Fig. 4.4(a) shows the ECa_v and ECa_h profiles measured along the transect ABCD. It is clear that these profiles behave similarly to the depth to Tertiary clay as shown in Fig. 4.4(b). The 42 z_{clay} observations of transect ABCD and the 14 observations of transect EF were compared with their nearest ECa measurements. The fitting of the McNeill-relationship to the z_{clay} - ECa_v data points was done by minimizing the sum of the squared differences between z_{clay} and z_{clay}^* by iteratively altering the modelling parameters $\text{EC}_{v,\text{loess}}$ and $\text{EC}_{v,\text{clay}}$ in Eqs. (4.3) and (4.4). The optimal values of $\text{EC}_{v,\text{loess}}$ and $\text{EC}_{v,\text{clay}}$ were 36 and 150 mS m^{-1} , respectively, with a R^2 of 0.86 (Fig. 4.5). The same procedure was applied to the z_{clay} - ECa_h data. The resulting

$EC_{h,loess}$ and $EC_{h,clay}$ were 12 and 145 $mS\ m^{-1}$, respectively, with a R^2 of 0.88. However, as the theoretical relationship by McNeill (1980b) indicates, the horizontal orientation is less sensitive to deeper soil layers. It receives 70 % of its influence from the top 0.75 m in homogeneous soil while the vertical orientation integrates 70 % of its response over the top 1.60 m soil. Therefore preference was given to the z_{clay} - ECa_v relationship to model z_{clay}^* :

$$z_{clay}^* = \left[\frac{1}{4 \cdot \left(1 - \frac{ECa_v - 150}{-114} \right)^2} - \frac{1}{4} \right]^{0.5} \quad [4.8]$$

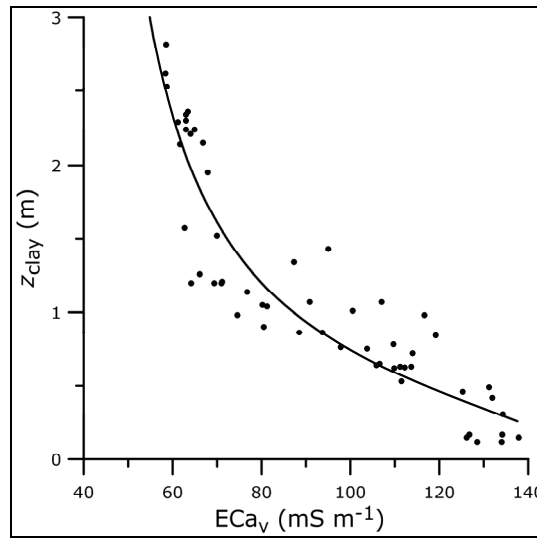


Fig. 4.5 z_{clay} as a function of ECa_v along study transects ABCD and EF with fitted McNeill-curve.

4.8 Paleotopography beneath the loess cover

The accuracy of the proposed model to predict z_{clay}^* was evaluated by investigating at 24 locations, laid out as a grid. At these locations, the observed depths were compared with the modelled depths. The MEE and RMSEE were respectively 0.04 m and 0.22 m. The r between z_{clay} and z_{clay}^* was 0.83 (Fig. 4.6). Therefore, the modelled relationship had a low bias, was reasonably accurate and correlated well with the observed depths.

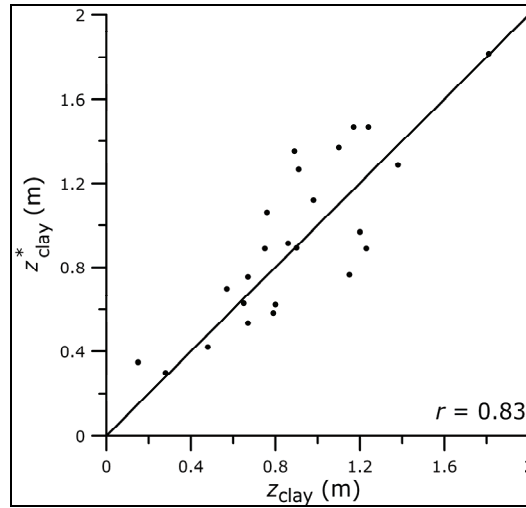


Fig. 4.6 Validation of predicted depth to the Tertiary clay (z^*_{clay}) using 24 observed depths (z_{clay}).

The soil surface elevation (Z) of the fields was interpolated and visualized in Fig. 4.7(a). The ECa_v measurements were converted into z^*_{clay} using Eq. (4.8). We did not use an interpolation method, like regression kriging or simple kriging with varying local means (Goovaerts, 1997), to construct the z^*_{clay} map because the spatial configuration of the observations of z_{clay} was concentrated along one transect only. The predicted values were subtracted from Z and the resulting $Z - z^*_{\text{clay}}$ values were interpolated as shown in Fig. 4.7(b).

To improve the visibility of the paleotopography, the interpolated map of the predicted depths is displayed in Fig. 4.7(c). The previous interpolations were carried out based on the variogram parameters given in Table 4.3. When comparing the current topography (Fig. 4.7(a)) with the paleotopography represented by the Tertiary clay (Fig. 4.7(b) and (c)), it will be clear that the paleolandscape beneath the loess cover is less smooth. A pattern of shallow gullies emerged in the Tertiary substrate, despite its clayey composition. These gullies combine into one major gully which ends in what seems to be a wider valley. To evaluate the continuity of these flow pathways, the Idrisi Kilimanjaro (Clark Labs, Worcester, MA, U.S.A.) modules RUNOFF (Jenson and Domingue, 1988) and WATERSHED were applied to the paleotopography surface. The result is visualized in Fig. 4.7(b). A clear accumulation of flow lines, representing past surface flow patterns, emerges. Hubert (1976) reported the occurrence of strong erosion during the glacial stages of the Pleistocene. Due to the deposition of the wind transported loess in the Late-Pleistocene the variability of the glacial Quaternary surface disappeared, however, locally a mixture of loess and clay remained, as observed between point B and C on the transect (Fig. 4.4(b)). Valleys were filled up with thick loess sediments, while elevated locations were covered by a thin layer. Subsequent erosion modified the thickness of the loess further, increasing the thickness of the valley loess by colluvial deposits.

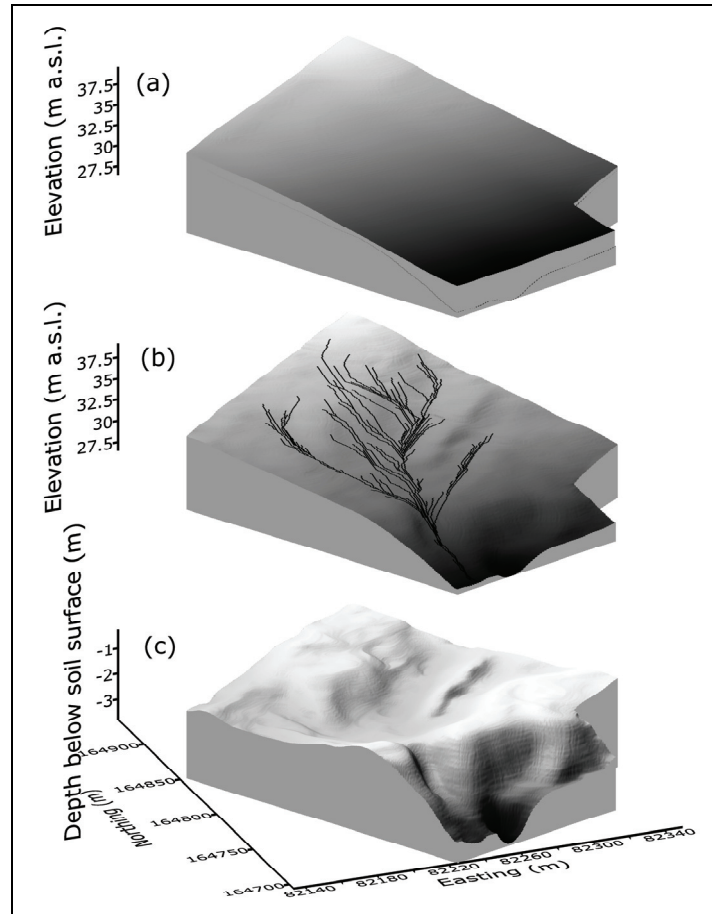


Fig. 4.7 Current soil surface (a), paleotopography beneath the loess cover represented as elevation above sea level with indications of simulated flow lines (b), and paleotopography represented as depth below soil surface (c).

4.9 Conclusions

The ECa measurements of the EM38DD sensor in the vertical mode proved to be suitable to predict z_{clay} (RMSEE of 0.22 m). The relationship between z_{clay} and ECa was found to be best represented by the theoretical response curve proposed by McNeill (1980b) (R^2 of 0.86). Also, measurements obtained on one field could be combined with those of an adjacent field without the need of additional field validation. The reconstructed paleotopography showed realistic patterns of surface processes, which could be modelled as a continuous flow process by a flow runoff model.

As a result, we can conclude that the combination of high density EMI sensor measurements with direct observations of the depth of the Tertiary clay beneath the Quaternary loess cover for shallow depths (< 3 m), proved to be a successful method for the reconstruction of the paleotopography at the end of the last glacial period.

Chapter 5

Comparing the EM38DD and DUALEM-21S sensors for depth-to-clay mapping¹

5.1 Abstract

Geophysical instruments show large potential for the detailed quantification of soil stratigraphy. In this study, two electromagnetic induction sensors were evaluated on their capacity to map small-scale variations of the depth to the interface (z_{clay}) in a two-layered soil. On a 2 ha study site, z_{clay} between the silty topsoil and the contrasting clayey subsoil was modelled first by relating the two apparent electrical conductivity (ECa) measurements of the EM38DD sensor to observations of z_{clay} obtained by augerings. However, a substantial number of these calibration observations was needed to account for the modelling parameters. To avoid this step, an entirely non-invasive procedure was proposed based on one survey with the DUALEM-21S sensor. This sensor records simultaneously four ECa values with different coil configurations. These measurements correspond to four different depth response functions that allow modelling z_{clay} without calibration observations. The only assumption was a two-layered build-up of the soil profile. The z_{clay} predictions were validated with 24 independent depth observations. Both procedures resulted in equal correlation coefficients (0.85) between predicted and measured z_{clay} and average estimation errors (0.26 m). This indicated that both sensors allowed the accurate mapping of the depth to a contrasting textural layer. With the EM38DD, calibration observations are needed, whereas the four different coil configurations of the DUALEM-21S sensor provide sufficient information to predict the interface depth without augering efforts.

¹Modified from: Saey, T., Simpson, D., Vermeersch, H., Cockx, L., Van Meirvenne, M., 2009. Comparing the EM38DD and DUALEM-21S sensors for depth-to-clay mapping. Soil Science Society of America Journal, 73: 1-6.

5.2 Introduction

Electromagnetic induction (EMI) is a technique that measures the apparent soil electrical conductivity (ECa) by inducing an electrical current in the soil. Soil ECa is controlled by a combination of soil properties, like porosity, moisture content, concentration of dissolved electrolytes in the soil solution, temperature and the amount and composition of colloids (McNeill, 1980a). The major advantages of EMI are: (i) it is non-invasive and (ii) it gives an immediate response. These characteristics have made EMI instruments very popular for the inventory of lateral changes in subsurface soil properties with a fine spatial resolution. In general, EMI is most successful in areas with a single dominant factor of soil variability. Variations in EMI response can be directly related to changes in the dominant property (Doolittle and Collins, 1998).

Previous studies related the ECa measured with the EM38 sensor to the depth and thickness of soil horizons (Doolittle et al., 1994; Bork et al., 1998; Inman et al., 2002; Saey et al., 2008), soil moisture content (Brevik et al., 2006; Huth and Poulton, 2007), clay content (McBratney et al., 2005; Triantafilis and Lesch, 2005) and salinity (Lesch et al., 1998; Amezketa, 2006; 2007). In all of these studies, a single coil spacing was used to derive a relationship between ECa as measured by the EM38 and the property of interest. With EMI the depth of investigation is controlled by the coil spacing, coil orientation, frequency of the induced current and height of the probe above the ground (Gebbers et al., 2007). Because most EMI instruments have fixed frequency, the only options to control the depth of investigation are coil orientation, coil spacing and height above the ground. Therefore, colocalized instrument measurements attributed to multiple coil spacings or coil orientations provide more information in depth. Recently, Triantafilis et al. (2003) used the ratio between soil ECa measurements of EM31 and EM38 instruments, which differ in coil spacing and frequency, to infer a subsurface clay layer underlying sandier sediments in a prior stream channel.

With the EM38DD, the soil ECa is measured simultaneously in two orientations, each having its own depth response profile. The ratio of the two orientations gives an indication of the heterogeneity of the soil profile. This ratio proved to be a useful tool for the delineation of pedological discontinuities like frost-wedge pseudomorphs (Cockx et al., 2006) and clay lenses (Cockx et al., 2007). Less research has been done to exploit the possibilities of the DUALEM EMI soil sensors. These mostly have multiple coil spacings and multiple coil orientations, providing simultaneous measurements with different depth sensitivity. Abdu et al. (2007) compared the ECa - depth relationship between the DUALEM-1S and Geonics

EM38DD sensors. Lee et al. (2006) quantified the effectiveness of the DUALEM-2 in locating a failed septic system in a fine-textured soil.

Our aim was to accurately characterize the depth to the interface between two contrasting soil layers with the aid of EMI. As a test case, we used a 2 ha study site in central Belgium where Tertiary marine clay was covered by aeolian loess dating from the Weichselian glacial stage. The objective was to compare ECa measurements obtained with the EM38DD sensor with those of the DUALEM-21S sensor to obtain a continuous, detailed inventory of the field-scale soil stratigraphy.

5.3 Study site

The research site was located in Heestert (Belgium), situated in the European loess belt. The site was located on a southeast facing hillside with an average slope gradient of 7 % and an elevation ranging between 30 to 40 m above sea level (a.s.l.). The study site was a 2 ha arable parcel (with central coordinates: 50°47'58"N, 3°24'41"E). The soil type is a Luvisol according to the WRB classification system (FAO/ISRIC/ISSS, 1998), which is characterized by an argic horizon located between 0.3 - 0.35 m and 1.3 - 1.4 m depth.

5.4 ECa survey

Table 5.1 shows the summary statistics of the EM38DD and DUALEM-21S ECa measurements obtained at the study site. The means of the ECa values measured with coil configurations that give a larger weight to deeper soil layers are the largest: $ECa-DUALEM_{v,2} (ECa_{v,2}) > ECa-DUALEM_{v,1} (ECa_{v,1}) \approx ECa-EM38_v (ECa_v) > ECa-DUALEM_{p,2,1} (ECa_{p,2,1}) > ECa-EM38_h (ECa_h) > ECa-DUALEM_{p,1,1} (ECa_{p,1,1})$. However, the coefficient of variation of these signals was smaller. This indicates that in this two-layered soil, the subsoil can be considered more conductive and less heterogeneous than the topsoil.

Table 5.1 Descriptive statistics of ECa for the different coil configurations of the EMI sensors EM38DD and DUALEM-21S (n : number of observations, m : mean, s^2 : variance and CV : coefficient of variation).

	n	m mS m^{-1}	min mS m^{-1}	max mS m^{-1}	s^2 $(\text{mS m}^{-1})^2$	CV %
EM38 _h	8562	33	6	86	243	47
EM38 _v	8562	67	29	127	408	30
DUALEM _{p,1.1}	10103	29	7	76	175	46
DUALEM _{p,2.1}	10103	48	11	110	388	41
DUALEM _{v,1}	10103	66	24	124	374	29
DUALEM _{v,2}	10103	88	30	136	400	23

5.5 EM38DD

Ordinary kriging (OK) was used to interpolate the EM38DD measurements to a grid of 0.5 by 0.5 m (Goovaerts, 1997). A maximum of 64 neighbors was used within a circular search area with a radius of 20 m around the location being interpolated. The spatial structures of ECa_v and ECa_h were modelled by Gaussian variogram models. The parameters are given in Table 5.2. The interpolated ECa maps are shown in Fig. 5.1(a) and Fig. 5.1(b). Large differences in ECa were found over short distances, with a similar pattern between ECa_v and ECa_h .

Table 5.2 Variogram parameters for the variables ECa_v (mS m^{-1}), ECa_h (mS m^{-1}), current elevation (Z (m)), predicted depth-to-clay (z^*_{clay} (m)) modelled with the EM38DD measurements together with 56 calibration observations and z^*_{clay} (m) modelled with the DUALEM-21S measurements (C_0 : nugget variance; $C_0 + C_1$: sill and a : range of Gaussian variogram models).

	C_0	$C_0 + C_1$	a (m)
ECa_v	5	225	20
ECa_h	5	145	20
Z	0.001	0.601	35
z^*_{clay} (EM38DD + 56 calibration observations)	0.005	0.225	20
z^*_{clay} (DUALEM-21S)	0.008	0.363	20

To calibrate ECa_v and ECa_h with the depth to the interface (z_{clay}) between the Quaternary silty loess material and clay-rich Tertiary substrate, two calibration transects, ABCD and EF, were laid out. These transects were selected in such a way that both the highest and the lowest ECa measurements were visited more or less with the same frequency (Fig. 5.1(a)). The depth to the interface was measured at 46 observation points along transect ABCD (at 5 m interval) and 15 points along transect EF (at 3 m interval). The interface was encountered at 56

observation locations using a gouge auger. At four points of transect ABCD and one point of transect EF, the thickness of the loess exceeded our maximum augering depth of 3.5 m.

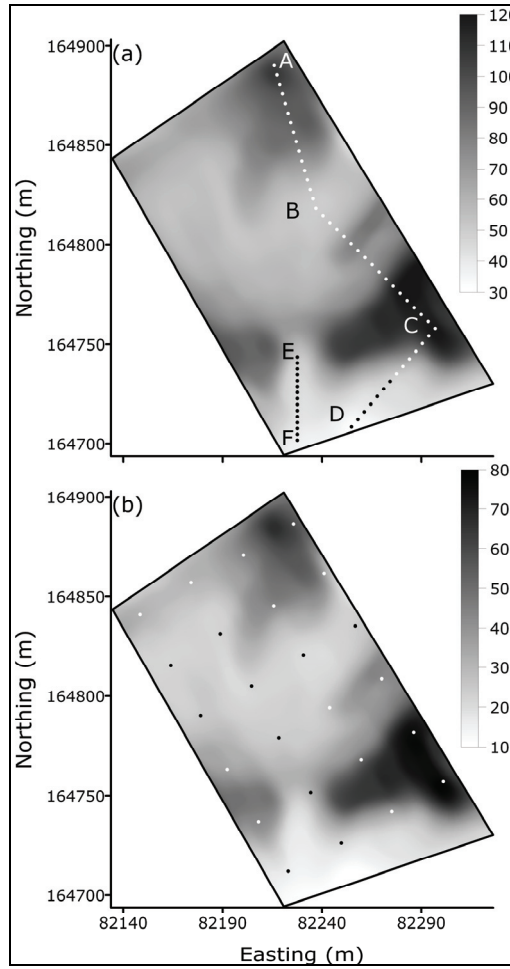


Fig. 5.1 Interpolated ECA_v (mS m⁻¹) with localization of calibration points on transects ABCD and EF (a) and interpolated ECA_h (mS m⁻¹) with localization of validation points (b).

The relationship between ECa measurements and z_{clay} observations was modelled using the McNeill (1980b) cumulative response curves. The main assumptions of this model are a two-layered soil build-up and a uniform ECa of the Quaternary loess and the Tertiary clayey substrate throughout the field. The cumulative response from the Quaternary topsoil and the Tertiary subsoil can be calculated as $R(z_{\text{clay}})$ and $1-R(z_{\text{clay}})$, for the vertical and horizontal dipole mode (Eqs. (2.9) and (2.10)). For each ECA_v and ECA_h measurement z_{clay}^* can be modelled by solving a system of nonlinear equations. Therefore, the automated function FSOLVE based on the Levenberg-Marquardt algorithm (Marquardt, 1963) in the high-level language and interactive environment Matlab (MathWorks, Natick, Massachusetts, U.S.A.) was used given the conductivity values of homogeneous Quaternary topsoil (EC_{loess}) and Tertiary clayey subsoil (EC_{clay}):

$$ECa_v = [R_v(z_{clay}^*)] \cdot EC_{loess} + [1 - R_v(z_{clay}^*)] \cdot EC_{clay} \quad [5.1]$$

$$ECa_h = [R_h(z_{clay}^*)] \cdot EC_{loess} + [1 - R_h(z_{clay}^*)] \cdot EC_{clay} \quad [5.2]$$

To fit these theoretical relationships to the $z_{clay} - ECa$ data, the sum of the squared differences between z_{clay} and z_{clay}^* was minimized:

$$\sum_{i=1}^n [z_{clay}(i) - z_{clay}^*(i)]^2 = \min \quad [5.3]$$

with n being the number of observations. The parameters EC_{loess} and EC_{clay} were iteratively adjusted to obtain the smallest sum of the squared differences between z_{clay} and z_{clay}^* . The obtained values of EC_{loess} and EC_{clay} were 12 mS m^{-1} and 125 mS m^{-1} . Converted to a reference temperature of $25 \text{ }^\circ\text{C}$, these values became 15 mS m^{-1} and 156 mS m^{-1} , which are similar to the values found in Chapter 4 (Saey et al. (2008)). So, at each measurement point, ECa_v and ECa_h were linked to z_{clay}^* by using Eqs. (2.9) and (2.10), (5.1) and (5.2) as:

$$ECa_v = 12 + \frac{113}{(4 \cdot z_{clay}^{*2} + 1)^{0.5}} \quad [5.4]$$

$$ECa_h = 12 - 226 \cdot z_{clay}^* + 113 \cdot (4 \cdot z_{clay}^{*2} + 1)^{0.5} \quad [5.5]$$

This system was solved to z_{clay}^* with Matlab using the Levenberg-Marquardt algorithm (Marquardt, 1963).

An independent validation was performed to evaluate the predictive quality of this model. Three indices were used as validation criteria: the mean estimation error (MEE), the root mean squared estimation error (RMSEE) and the Pearson correlation coefficient r . The validation data were obtained as 24 independent observations of the interface depth. These were taken at the centers of 24 grid cells projected over the study site. The observed depths were compared with the model predictions (Fig. 5.2). A strong correlation between predicted and measured depths (0.85) and a low RMSEE (0.26 m) indicated that this procedure was highly accurate in predicting z_{clay}^* . However, on average this procedure overestimated z_{clay} with a bias of 0.12 m, as indicated by the MEE.

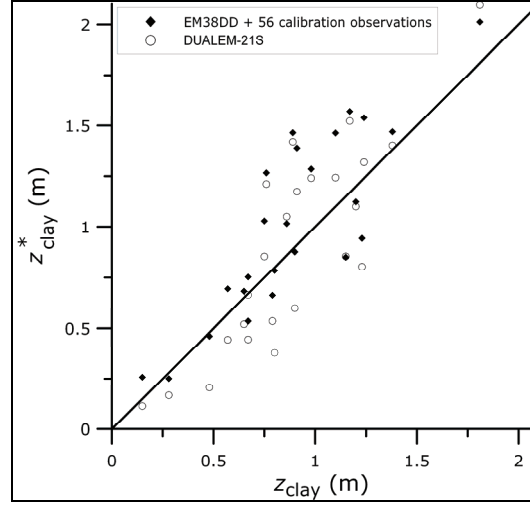


Fig. 5.2 Scatterplot of predicted interface depth (z_{clay}^*) versus the observed depth (z_{clay}) for both EMI-procedures ($n = 24$).

5.6 DUALEM-21S

The four simultaneous ECa measurements obtained with the quadruple-array DUALEM-21S instrument were used to reconstruct z_{clay} . In a two-layered soil build-up, the measured ECa can be estimated by summing the conductivities and depth-weighted contributions of each layer. Due to the characteristic depth response profiles for each coil configuration, the following four equations could be formulated (taking the height of the DUALEM-21S sensor above the soil surface (0.16 m) into account):

$$\text{ECa}_{p,1.1} = [R_{p,1.1}(z_{\text{clay}}^* + 0.16) - R_{p,1.1}(0.16)] \cdot \text{EC}_{\text{loess}}^* + [1 - R_{p,1.1}(z_{\text{clay}}^* + 0.16)] \cdot \text{EC}_{\text{clay}}^* \quad [5.6]$$

$$\text{ECa}_{p,2.1} = [R_{p,2.1}(z_{\text{clay}}^* + 0.16) - R_{p,2.1}(0.16)] \cdot \text{EC}_{\text{loess}}^* + [1 - R_{p,2.1}(z_{\text{clay}}^* + 0.16)] \cdot \text{EC}_{\text{clay}}^* \quad [5.7]$$

$$\text{ECa}_{v,1} = [R_{v,1}(z_{\text{clay}}^* + 0.16) - R_{v,1}(0.16)] \cdot \text{EC}_{\text{loess}}^* + [1 - R_{v,1}(z_{\text{clay}}^* + 0.16)] \cdot \text{EC}_{\text{clay}}^* \quad [5.8]$$

$$\text{ECa}_{v,2} = [R_{v,2}(z_{\text{clay}}^* + 0.16) - R_{v,2}(0.16)] \cdot \text{EC}_{\text{loess}}^* + [1 - R_{v,2}(z_{\text{clay}}^* + 0.16)] \cdot \text{EC}_{\text{clay}}^* \quad [5.9]$$

With $R_{p,x}(z)$ and $R_{v,x}(z)$ the cumulative responses above a depth z for the perpendicular and vertical dipole mode respectively and transmitter-receiver coil spacing of x .

At each measurement location, the nonlinear Eqs. (5.6), (5.7), (5.8) and (5.9) were combined to model $\text{EC}_{\text{loess}}^*$, $\text{EC}_{\text{clay}}^*$, and z_{clay}^* , given the quadruple-array ECa measurements: $\text{ECa}_{p,1.1}$, $\text{ECa}_{p,2.1}$, $\text{ECa}_{v,1}$ and $\text{ECa}_{v,2}$. This system was also solved with Matlab using the Levenberg-Marquardt algorithm (Marquardt, 1963).

The summary statistics of EC_{loess}^* , EC_{clay}^* , and z_{clay}^* within the study site ($\pm 10,000$ locations) are given in Table 5.3. The mean EC_{loess}^* is much smaller than the mean EC_{clay}^* , which confirms the subsoil material to be more conductive than the topsoil material. The spatial variability of EC_{loess}^* and EC_{clay}^* reflects a more realistic situation, compared to the assumption of uniformity which had to be made with the EM38DD. The coefficient of variation indicates that the variability of the toplayer is much larger compared to the sublayer. Soil tillage practices might have mixed the Tertiary clayey subsoil with the Quaternary silty topsoil at low interface depths explaining the larger variability of the topsoil.

Table 5.3 Descriptive statistics of EC_{clay}^* ($mS\ m^{-1}$), EC_{loess}^* ($mS\ m^{-1}$) and z_{clay}^* (m) modelled with the DUALEM-21S measurements (m : mean, s^2 : variance and CV : coefficient of variation).

	m	min	max	s^2	CV
EC_{loess}^*	18	3	31	21	25
EC_{clay}^*	124	85	171	10	3
z_{clay}^*	1.09	0.09	4.90	0.59	70

The procedure using the DUALEM-21S measurements for predicting z_{clay}^* was also validated using the same 24 depth observations as in the EM38DD validation. Fig. 5.2 shows the scatterplot of the observed versus predicted depths. The correlation coefficient between the predicted and measured depths and average error were identical to the values obtained with the EM38DD procedure ($r = 0.85$ and $RMSEE = 0.26$ m), with no bias. Therefore, both procedures performed similarly well in estimating z_{clay}^* . Nevertheless, the DUALEM-21S procedure did not require calibration observations. Moreover, this sensor allowed the estimation of ECa of the top- and subsoil layers.

5.7 Reconstructing the paleotopography

Soil surface elevation (Z) and z_{clay}^* as produced by both sensor procedures was interpolated using OK, similarly the ECa maps. The variogram parameters are given in Table 5.2. Fig. 5.3(a) shows the smooth behaviour of the present topography. However, both z_{clay}^* surfaces, resulting from the two EMI procedures (Fig. 5.3(b) and 5.3(c)), exhibit a strong small-scale variability of the interface between the Quaternary loess and the Tertiary clay. Moreover, both z_{clay}^* surfaces show a similar behavior. The DUALEM-21S procedure displays a larger detail at higher depths compared to the EM38DD-based procedure, probably due to the higher DOE of the DUALEM_{v,2} coil configuration.

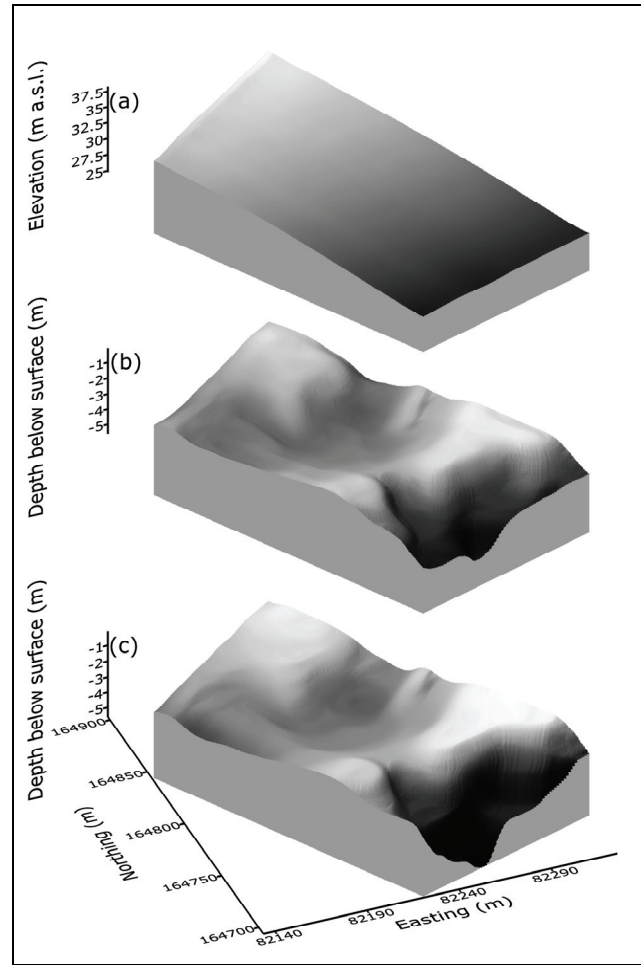


Fig. 5.3 Elevation of the current soil surface (a), z_{clay}^* predicted by the EM38DD procedure (b), and z_{clay}^* predicted by the DUALEM-21S procedure (c).

5.8 Conclusions

Both EMI sensors allowed to predict z_{clay} in a two-layered soil accurately in a rapid, effective and non-destructive manner (RMSEE of 0.26 m). With the EM38DD, a number of soil auger observations is required to calibrate the ECa measurements in respect to z_{clay} . The quadruple-array DUALEM EMI 2,1S instrument avoids the need for calibration augerings. Its rich information enables a quantification of z_{clay} with a similar predictive accuracy. Additionally, it provides inventories of the spatial variability in top- and subsoil conductivity.

Chapter 6

Mapping depth-to-clay using fitted multiple depth response curves¹

6.1 Abstract

As an alternative for the depth response approximations based on the theoretical Maxwell's equations, a procedure was proposed to fit depth response curves for different coil configurations. A 39 ha study area was selected in the Belgian loess belt, where loess material was situated on a Tertiary substrate. A survey with the DUALEM-21S electromagnetic induction instrument was carried out to map the depth-to-clay (z_{clay}). The depth response curves were fitted both for the vertical and perpendicular coil configurations using 85 depth observations of z_{clay} .

The resulting depth response curves $R(z_{\text{clay}})$ were:

$$R_{p,s}(z_{\text{clay}}) = 0.8135 \cdot e^{-1.4131 \cdot \left(\frac{z_{\text{clay}}}{s}\right)} \quad \text{and} \quad R_{v,s}(z_{\text{clay}}) = 0.9802 \cdot e^{-0.8102 \cdot \left(\frac{z_{\text{clay}}}{s}\right)}$$

for the perpendicular and vertical coil configurations (with s as the intercoil spacing).

A set of 4 equations based on the developed depth response functions was used to model z_{clay} at each of the 209 400 measurement points. These z_{clay} predictions were validated using geo-electrical imaging. With two multi-electrode resistivity arrays, z_{clay} was 1D-inverted at 95 locations along two transects, assuming a two-layered soil system. A coefficient of determination of 0.95, with a root-mean squared estimation error of 0.22 m, was found between the predicted and 1D-inverted depths. This procedure allowed the accurate 3D-reconstruction of the paleolandscape before the deposition of the loess. Flow lines were modelled on this paleosurface, revealing past or subsurface stream patterns not visible on the present relief.

¹Modified from: Saey, T., Van Meirvenne, M., De Smedt, P., Cockx, L., Meerschman, E., Islam, M. M., Meeuws, F., 2011. Mapping depth-to-clay using fitted multiple depth response curves of a proximal EMI sensor. *Geoderma*, Published Online (DOI: doi:10.1016/j.geoderma.2011.01.015).

6.2 Introduction

Electromagnetic induction (EMI) instruments measure a depth-weighted average of the soil electrical conductivity. Quantitative applications of EMI sensors to subsoil investigations depend on the ability to transform the measured apparent electrical conductivities (ECa) into horizontal and vertical variations of relevant soil properties such as soil type, soil horizons, soil water storage and soil organic matter (Domsch and Giebel, 2004; Saey et al., 2009b; Tromp-van Meerveld and McDonnell, 2009). Although useful for looking at lateral spatial variation, the ECa gives limited information on how conductivity varies with depth (Pellerin and Wannamaker, 2005). Generally, the propagation of EMI radiation into the soil is described by Maxwell's equations (Reynolds, 1997). The relative response to the primary magnetic field created by the EMI instruments varies with depth and is therefore expressed as a depth response function. This response function is the weighting function for the ECa (= depth-weighted conductivity) (Morris, 2009).

McNeill (1980b) defined the depth response functions of EMI instruments in homogeneous soils by asymptotic approximations of the Maxwell's equations. Hendrickx et al. (2002) proved these approximations to be valid in heterogeneous soils. They are based on the assumption that the induction number (β) is very small (Spies and Frischknecht, 1991). This is equivalent to stating that the flow of charge in any loop of the magnetic field is completely independent of the flow of charge in any other loop since they are not magnetically coupled (McNeill, 1980b). The induction number is the ratio of the intercoil separation s to the skin depth δ . This skin depth is defined as the distance at which the propagating magnetic field strength has been attenuated to e^{-1} of the strength at the surface and varies inversely with the ECa at low frequencies. Within the restriction of a small β , the McNeill approximation (1980b) holds which means that the instrument output is proportional to the ECa and the depth response functions are independent of ECa (Hendrickx et al., 2002). However, Callegary et al. (2007) proved with numerical models based on Maxwell's equations that the depth response can be altered by soil properties affecting the ECa. Especially under high electrically conductive conditions, the simulated depth response function deviates from the function predicted from the McNeill (1980b) approximation.

Saey et al. (2009a) used the depth response curves of McNeill (1980b) and Dualem Inc. (2007) based on Wait (1962) for the vertical and perpendicular coil configurations to predict the depth-to-clay (z_{clay}) in a two-layered soil. Moreira Santos et al. (2010) used a one-dimensional, laterally constrained algorithm to invert field-measured ECa data collected with a DUALEM-421S instrument. A forward modelling subroutine, based on the cumulative

response from McNeill (1980b) was used to calculate the apparent conductivity response of the model. Low z_{clay} values were associated with high ECa values and corresponding high β what makes the asymptotic approximations for the theoretical depth response functions deviating from the real depth response. On the other hand, different numerical inversion simulations based on Maxwell's equations fail to handle the depth functions for the perpendicular coil configurations. Therefore, the objective of this study was to fit depth response curves for different EMI coil configurations in a two-layered soil and apply these to map z_{clay} in a study area within the Belgian loess belt.

6.3 Study site

The 39 ha research area was located in Heestert (Belgium) (Fig. 6.1). It is situated on a southeast facing hillside with an elevation ranging between 25 to 45 m above sea level (a.s.l.). The site consists of eleven neighbouring arable fields (central coordinates: 50°47'58"N, 3°24'41"E). On the national soil map (scale 1:20 000), the soil series of the study area are characterized by a shallow or deeper clay substrate, a silt loam topsoil texture, moderately wet conditions and a textural B-horizon. This soil type corresponds to a loess-derived Haplic Luvisol (World Reference Base, 1998), which is characterized by an argic horizon ranging from 0.3-0.35 m up to 1.3-1.4 m in depth. Nevertheless, the Tertiary clay substrate has much higher clay content than this argic horizon. Initially, the deposited loess was calcareous, but it decalcified mostly to a depth of 2-2.5 m (Hubert, 1976). Generally, a two-layered soil system is acceptable with silty-loess material above a clayey substrate.

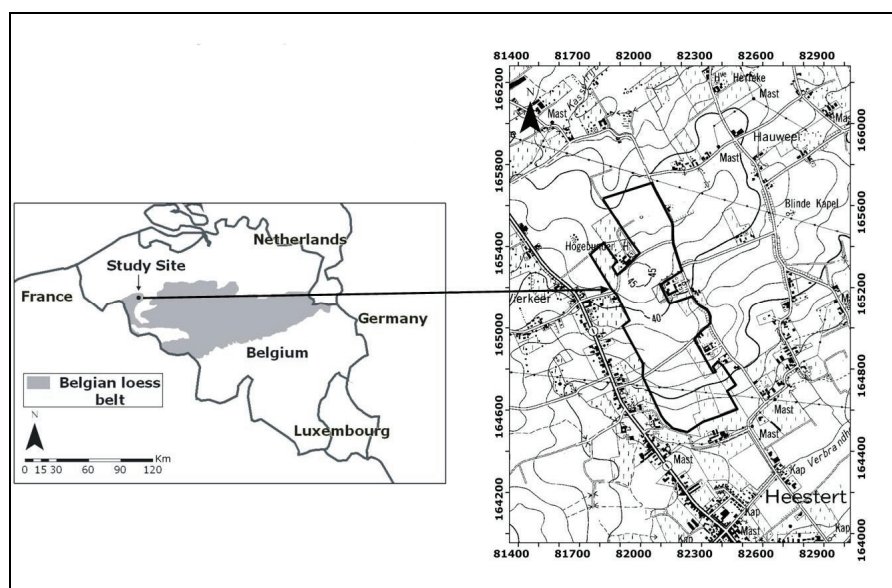


Fig. 6.1 Localization of the study area in the Belgian loess belt and topographic map with indication of the boundaries (coordinates are according to the Belgian metric Lambert 72 projection).

6.4 ECa survey

The soil ECa of the study area was recorded with the DUALEM-21S soil sensor. The sensor was put in a non-metal sled and pulled behind an all-terrain vehicle at about 10 km h⁻¹ crossing the field at parallel lines 4 m apart.

Table 6.1 shows the summary statistics of the four ECa measurements taken with the DUALEM-21S sensor at 209 400 locations. The mean and maximum values of the ECa values increase with increasing DOE (Saey et al., 2009a), so the larger the measured soil volume, the higher the conductivity. The negative minimum values of ECa_{p,1,1} and ECa_{p,2,1} were assumed to be caused by anomalies in the subsoil like small metal objects. The standard deviations increase with increasing DOE, because of the higher differences in absolute values. Fig. 6.2 shows the ECa_{v,1} measurements of the study area converted to a reference measurement temperature of 25°C. In order to obtain estimates of variables at unsampled locations, ordinary point kriging (OK) was used as an interpolation method. In this study, a minimum of 8 neighbours was used within a circular search area with a radius of 20 m around the location being interpolated. The spatial structure of the variables was represented by variogram models, which were used to assign weights to the neighbouring points. The parameters of the ECa_{v,1} variogram model are given in Table 6.2. Large differences of ECa_{v,1} were observed across the study area, probably due to depth variations of the higher conductive subsoil.

Table 6.1 Descriptive statistics (*m*: mean, min: minimum, max: maximum, *s*: standard deviation) of ECa_{p,1,1}, ECa_{p,2,1}, ECa_{v,1} and ECa_{v,2} for the 209 400 measurements in the study area (in mS m⁻¹ after conversion to a reference temperature of 25°C).

Variable	<i>m</i>	min	max	<i>s</i>
ECa _{p,1,1}	33	-22	108	13
ECa _{p,2,1}	56	-35	164	22
ECa _{v,1}	65	2	176	26
ECa _{v,2}	85	33	230	30

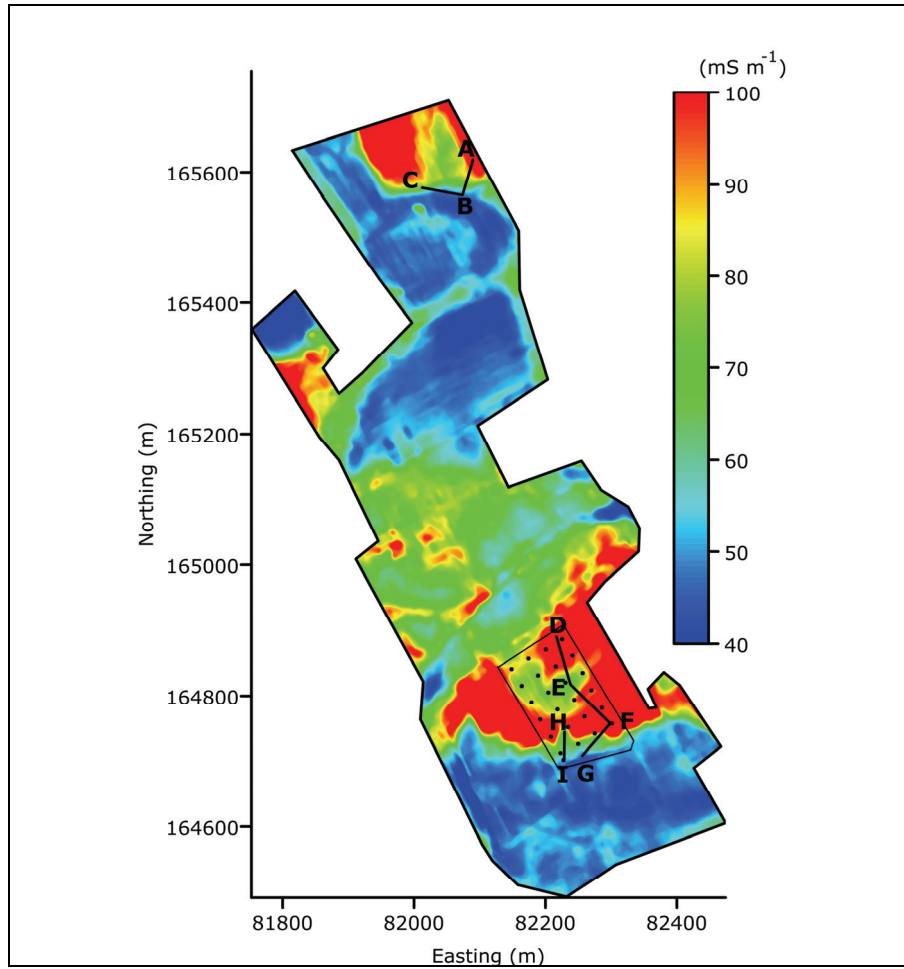


Fig. 6.2 Kriged apparent electrical conductivity map (converted to a reference temperature of 25°C) in the 1 m – vertical coil configuration ($ECa_{v,1}$) with localization of transects AB, BC, DEFG and HI and the 30 m by 30 m grid. The border of the test area is denoted with a black frame.

Table 6.2 Parameters of the variogram model for $ECa_{v,1}$, elevation of the current soil surface (Z) and z^*_{clay} (C_0 : nugget variance; $C_0 + C_1$: sill and a : range).

Variable	Type	C_0	$C_0 + C_1$	Slope	a (m)
$ECa_{v,1}$ ($mS\ m^{-1}$)	Linear	0	-	4.2	-
Z (m)	Gaussian	0.0005	1.7005	-	30
z^*_{clay} (m)	Gaussian	0.004	1.559	-	30

6.5 Depth observations

The locations of the z_{clay} observations within the test area were shown on Fig. 6.2. This test area was taken because of the high differences in ECa values on a relatively short distance and was supposed to be representative for the entire study area. Two transects DEFG and HI and one 30 m by 30 m grid (Fig. 6.2) were laid out within our test area in such a way that higher and lower ECa measurements of the test field were visited (Fig. 6.2) (Saey et al., 2008). Along the 225 m of transect DEFG 46 observation points were located at 5 m intervals, while along transect HI 15 points were selected at 3 m intervals. 24 observation points were located on a 30 m by 30 m grid. At each of these 85 points, z_{clay} was observed by augering with a gouge auger. At the last four sampling points of transect DEFG and the last sampling point of transect HI, the loess layer extended beyond a depth of 3.5 m, which was our maximal augering depth. These observations were not taken into account for the calculation of the depth response curves.

With these 80 depth observations, the cumulative response curves for the perpendicular and vertical coil configurations were fitted. Table 6.3 shows that on the 225 m transect DEFG, z_{clay} is on average relatively shallow (0.79 m), with a variation from 0.12 m to 1.57 m, similarly to the spread of the z_{clay} observations on the 30 m by 30 m grid (0.15 m to 1.81 m). On the 45 m transect HI, z_{clay} increases from 1.52 m to 2.82 m.

Table 6.3 Descriptive statistics (n : number, m : mean, min: minimum, max: maximum, s : standard deviation) of z_{clay} at the test field.

	n	m	min	max	s
		(m)	(m)	(m)	(m)
transect DEFG	42	0.79	0.12	1.57	0.39
transect HI	14	2.26	1.52	2.82	0.30
grid	24	0.89	0.15	1.81	0.36

6.6 EC-probe measurements

The standard EC-probe set for soil conductivity measurements consists of an EC-probe and an earth resistivity meter. Measurement of the soil resistivity using four electrodes is based on the Wenner-method, described by Rhoades and Van Schilfgaarde (1976). The EC-probe measures in situ the electrical resistivity of a limited (elliptic) soil volume of 80 cm³ of soil around the probe. A temperature sensor is used to convert the measurements to a reference

temperature. This sensor can be used only for a limited number of punctual measurements. Moreover, these act as calibration measurements for the proximal soil sensing data.

With the EC-probe, EC measurements of the two layers were conducted according to a 30 m by 30 m grid on the test area (Fig. 6.2). However, only measurements at a depth more than 30 cm above or below the loess-clay interface were retained to obtain the average EC. Moreover, the limited length of the EC-probe rod (1 m) diminished the amount of measurements substantially. The average EC of the loess layer (EC_{loess}) was $21 \pm 6 \text{ mS m}^{-1}$ (12 measurements) and of the clayey layer (EC_{clay}) it was $192 \pm 13 \text{ mS m}^{-1}$ (7 measurements), at 25°C . These values were taken to be representative for the two different layers across the study area.

6.7 Fitting depth response curves

In a two-layered soil model where silty loess is situated above a clayey substrate, the relationship between z_{clay} and the ECa can be modelled by formulating the cumulative response $R_p(z_{\text{clay}})$ for the perpendicular coil orientation and $R_v(z_{\text{clay}})$ for the vertical coil orientation. Doolittle et al. (1994), Cockx et al. (2007) and Vitharana et al. (2008a) fitted exponential regression models to their z_{clay} - ECa observations. Depths are normalized by dividing the z_{clay} by the intercoil spacing s to remove the effect of differences in intercoil spacing into our cumulative response functions $R_p(z_{\text{clay}})$ and $R_v(z_{\text{clay}})$ (Morris, 2009):

$$R_p(z_{\text{clay}}) = 1 - \alpha_p \cdot e^{-\beta_p \left(\frac{z_{\text{clay}}}{s} \right)} \quad [6.1]$$

$$R_v(z_{\text{clay}}) = 1 - \alpha_v \cdot e^{-\beta_v \left(\frac{z_{\text{clay}}}{s} \right)} \quad [6.2]$$

with α_p and β_p the unknown parameters of the exponential cumulative response function for the perpendicular coil configuration $R_p(z_{\text{clay}})$ and α_v and β_v the unknown parameters of the exponential cumulative response function for the vertical coil configuration $R_v(z_{\text{clay}})$. These unknown parameters α_p and β_p will be empirically determined by fitting the cumulative response function $R_p(z_{\text{clay}})$ to the z_{clay} - $ECa_{p,1,1}$ and z_{clay} - $ECa_{p,2,1}$ observations and α_v and β_v will be determined by fitting the cumulative response function $R_v(z_{\text{clay}})$ to the z_{clay} - $ECa_{v,1}$ and z_{clay} - $ECa_{v,2}$ observations. The procedure used to fit $R_p(z_{\text{clay}})$ to the z_{clay} - $ECa_{p,1,1}$ measurements is described below.

The cumulative responses from the upper and lower layers are $R_{p,s}(z_{\text{clay}})$ and $1 - R_{p,s}(z_{\text{clay}})$, with s the intercoil spacing. For every z_{clay} , the corresponding $ECa_{p,1,1}$ and $ECa_{p,2,1}$ can be expressed as a function of the apparent conductivity values of the Quaternary loess and Tertiary clay

(EC_{loess} and EC_{clay} respectively), taking the height of the DUALEM-21S sensor above the soil surface (0.16 m) into account:

$$ECa_{p,1.1} = [R_{p,1.1}(z_{\text{clay}} + 0.16) - R_{p,1.1}(0.16)] \cdot EC_{\text{loess}} + [1 - R_{p,1.1}(z_{\text{clay}} + 0.16)] \cdot EC_{\text{clay}} \quad [6.3]$$

$$ECa_{p,2.1} = [R_{p,2.1}(z_{\text{clay}} + 0.16) - R_{p,2.1}(0.16)] \cdot EC_{\text{loess}} + [1 - R_{p,2.1}(z_{\text{clay}} + 0.16)] \cdot EC_{\text{clay}} \quad [6.4]$$

Based on Eqs. (6.3) and (6.4), z_{clay}^* can be modelled given the $ECa_{p,1.1}$ and $ECa_{p,2.1}$ measurements. Therefore, $R_{p,1.1}(z_{\text{clay}}^*)$ and $R_{p,2.1}(z_{\text{clay}}^*)$ were calculated given the ECa measurements and the conductivities of the two layers (EC_{loess} and EC_{clay}):

$$R_{p,1.1}(z_{\text{clay}}^* + 0.16) = \frac{ECa_{p,1.1} + R_{p,1.1}(0.16) \cdot EC_{\text{loess}} - EC_{\text{clay}}}{EC_{\text{loess}} - EC_{\text{clay}}} \quad [6.5]$$

$$R_{p,2.1}(z_{\text{clay}}^* + 0.16) = \frac{ECa_{p,2.1} + R_{p,2.1}(0.16) \cdot EC_{\text{loess}} - EC_{\text{clay}}}{EC_{\text{loess}} - EC_{\text{clay}}} \quad [6.6]$$

These calculated $R_{p,1.1}(z_{\text{clay}}^* + 0.16)$ and $R_{p,2.1}(z_{\text{clay}}^* + 0.16)$ can be put into Eqs. (6.1) and (6.2) to obtain the modelled z_{clay}^* :

$$z_{\text{clay}}^* = -\frac{s}{\beta_p} \cdot \ln\left(\frac{(1 - R_{p,1.1}(z_{\text{clay}}^*))}{\alpha_p}\right) - 0.16 \quad [6.7]$$

$$z_{\text{clay}}^* = -\frac{s}{\beta_p} \cdot \ln\left(\frac{(1 - R_{p,2.1}(z_{\text{clay}}^*))}{\alpha_p}\right) - 0.16 \quad [6.8]$$

To fit a cumulative depth response function to the z_{clay} - $ECa_{p,1.1}$ and z_{clay} - $ECa_{p,2.1}$ data points, the sum of the squared differences between z_{clay} and z_{clay}^* was minimized, simultaneously for both the 1.1P and 2.1P coil configurations:

$$\sum_{i=1}^n [z_{\text{clay}}(i) - z_{\text{clay}}^*(i)]^2 = \min \quad [6.9]$$

with i the number of the observation and n the total amount of observations. The parameters of the cumulative response function α_p and β_p were iteratively adjusted to obtain the smallest sum of the squared differences between z_{clay} and z_{clay}^* for both the 1.1P and 2.1P coil configurations.

The same approach was followed to fit a cumulative depth response function to the z_{clay} - $ECa_{v,1}$ and z_{clay} - $ECa_{v,2}$ observations, resulting in unique parameters α_v and β_v for the response function of the vertical coil configuration. This minimization procedure was performed for both perpendicular coil configurations together and for both vertical coil configurations together. The difference between observed and modelled z_{clay} was

simultaneously minimized for both 1.1P and 2.1P coil configurations and simultaneously for both 1V and 2V coil configurations.

The optimal values of α_p and β_p were 0.8135 and 1.4131 and 0.9802 and 0.8102 for α_v and β_v . The obtained empirical depth response curves were:

$$R_{p,s}(z_{\text{clay}}) = 1 - 0.8135 \cdot e^{-1.4131 \left(\frac{z_{\text{clay}}}{s} \right)} \quad [6.10]$$

$$R_{v,s}(z_{\text{clay}}) = 1 - 0.9802 \cdot e^{-0.8102 \left(\frac{z_{\text{clay}}}{s} \right)} \quad [6.11]$$

with $R_{p,s}(z)$ and $R_{v,s}(z)$ the responses above a depth z for the perpendicular and vertical dipole mode and transmitter-receiver coil spacing s . The DOE for the fitted cumulative depth response functions were 0.62 m and 1.32 m for the 1.1P and 2.1P coil configurations and 1.30 and 2.76 m for the 1V and 2V coil configurations. Fig. 6.3 shows the cumulative response curves (expressed as z_{clay} - ECa relationship given the conductivities of the different layers EC_{loess} and EC_{clay}) plotted against their 80 corresponding z_{clay} - ECa observations. The modelled response curves coincide well with the z_{clay} - ECa observations. Coefficients of determination (R^2) are 0.74 and 0.77 for the 1.1P and 2.1P coil configurations and 0.65 and 0.68 for the 1V and 2V coil configurations. Only the low $ECa_{v,1}$ observations underestimate the real z_{clay} . Below an ECa of about 20 mS m⁻¹ for the 1.1P coil configuration, z_{clay} changes largely with small changes in ECa. Therefore, this depth response curve is inappropriate to predict the deeper z_{clay} . The inverse situation can be observed with regard to the 2V configuration. This configuration shows an almost linear z_{clay} - ECa trend below a value of about 90 mS m⁻¹, confirming the sensitivity of the 2V coil configurations for deeper z_{clay} .

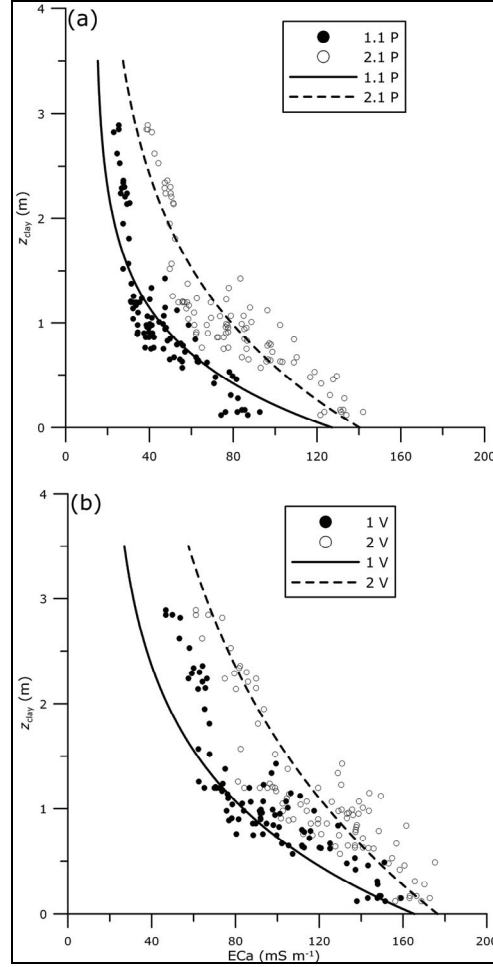


Fig. 6.3. Fitted cumulative depth response curves (and expressed as depth-to-clay (z_{clay}) – apparent electrical conductivity (ECa) relationship) (a) for the perpendicular coil configurations and (b) the vertical coil configurations of the DUALEM-21S, each with their corresponding z_{clay} -ECa observations.

6.8 Depth modelling

The four simultaneous ECa measurements obtained with the quadruple-array DUALEM-21S sensor were combined to model and map z_{clay} . In a two-layered soil build-up, the measured ECa can be estimated by summing the conductivities and contributions of each layer. The conductivities of the loess and clayey layer were taken from the EC-borehole measurements and assumed homogeneous across the study area. Finally, the following four equations could be formulated:

$$\text{ECa}_{p,1.1} = [R_{p,1.1}(z_{\text{clay}}^* + 0.16) - R_{p,1.1}(0.16)] \cdot \text{EC}_{\text{loess}} + [1 - R_{p,1.1}(z_{\text{clay}}^* + 0.16)] \cdot \text{EC}_{\text{clay}} \quad [6.12]$$

$$\text{ECa}_{p,2.1} = [R_{p,2.1}(z_{\text{clay}}^* + 0.16) - R_{p,2.1}(0.16)] \cdot \text{EC}_{\text{loess}} + [1 - R_{p,2.1}(z_{\text{clay}}^* + 0.16)] \cdot \text{EC}_{\text{clay}} \quad [6.13]$$

$$ECa_{v,1} = [R_{v,1}(z_{clay}^* + 0.16) - R_{v,1}(0.16)] \cdot EC_{loess} + [1 - R_{v,1}(z_{clay}^* + 0.16)] \cdot EC_{clay} \quad [6.14]$$

$$ECa_{v,2} = [R_{v,2}(z_{clay}^* + 0.16) - R_{v,2}(0.16)] \cdot EC_{loess} + [1 - R_{v,2}(z_{clay}^* + 0.16)] \cdot EC_{clay} \quad [6.15]$$

with $R_{p,s}(z)$ and $R_{v,s}(z)$ the responses above a depth z for the perpendicular and vertical dipole mode respectively (Eqs. (3.6) and (3.4)) and $EC_{loess} = 21 \text{ mS m}^{-1}$ and $EC_{clay} = 192 \text{ mS m}^{-1}$. At each of the 209 400 measurement locations, the nonlinear Eqs. (6.12), (6.13), (6.14) and (6.15) were combined to model z_{clay}^* . This system was solved with Matlab using the Levenberg-Marquardt algorithm (Marquardt, 1963).

6.9 Resistivity imaging

Geo-electrical imaging was done with the ABEM Terrameter and Lund electrode selector system (ABEM instrument AB, Sundbyberg, Sweden). The combined Wenner-Schlumberger electrode configuration was chosen because it has a better horizontal coverage than the Wenner array. The Wenner-Schlumberger array shows a fair sensitivity to horizontal and vertical features (Kaufmann and Cerak, 2001)

The data obtained were first interpreted using RES2DINV software (Loke et al., 2003) to determine a two-dimensional resistivity model for the subsurface which produces a pseudosection that agrees with the actual measurements (Geotomo software, 2007).

If the layering of the soil is known, the purpose of a 1D-inversion subroutine exists in determining the thickness and the resistivity of the different layers. We used RES1D (Loke, 2001) for this purpose. In this method, an initial model must be given, and the optimisation subroutine modifies the thickness and resistivity of the layers so as to reduce the difference between the calculated and measured apparent resistivity values.

The accuracy of the proposed model to predict z_{clay}^* was evaluated by using the 1D-inverted depths at the 2 transects AB and BC located in a different part of the study area but with an analogous range of ECa values as the test area (Fig. 6.2). 1D inversion was done given an initial model representing a two-layered soil with resistivity of the topsoil much higher than that of the subsoil. This initial model was confirmed by the 2D-transect modelling (Fig. 6.4).

EC_{loess}^* and EC_{clay}^* were also modelled at each measurement location. They were found to be relatively stable, except near the borders of the transects, which was due to less resistivity measurements. The average EC_{loess}^* and EC_{clay}^* were 28 and 194 mS m^{-1} , which corresponded well to the values measured with the EC probe (21 and 192 mS m^{-1}). At these 95 locations, the 1D-inverted depths were compared with the modelled depths (Fig. 6.5). The MEE and

RMSEE were respectively 0.08 m and 0.22 m. In order to compare the RMSEE or the accuracy of prediction between variables of different type, the RMSEE can be normalized by the total variation, by dividing it by the standard deviation of the observations (in this case 0.67 m). As a rule of thumb, Hengl et al. (2003) considered that a value of relative RMSEE close to 40 % means a fairly satisfactory accuracy of prediction. Otherwise, if the values get > 71 %, this means that the model accounted for less than 50 % of variability at the validation points and the prediction is unsatisfactory. In this case, the relative RMSEE is 33 %, certainly accurate enough for hydrological modelling. The R^2 between z_{clay} and z^*_{clay} was 0.95, which is highly significant at $\alpha = 0.05$. Therefore, the modelled relationship was found to have a negligible bias, to be reasonably accurate and to correlate well with the observed depths. Moreover, the formulated cumulative depth response curves prove to be useful for modelling the depth to the interface in a two-layered soil.

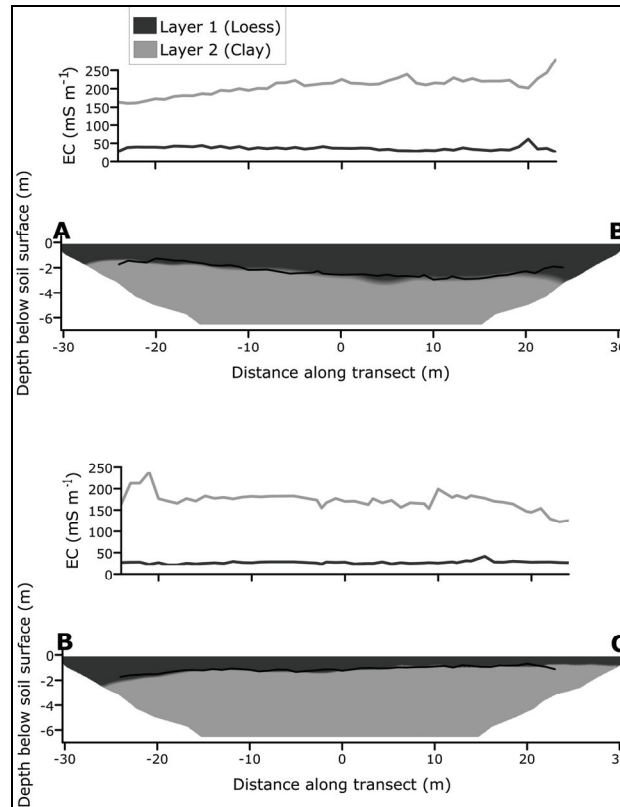


Fig. 6.4 2D-inverted transects with 1D-inverted depths of the interface between the loess and clay (black line) and the corresponding modelled conductivities of the loess (EC_{loess}) and clay (EC_{clay}) for transects AB and BC.

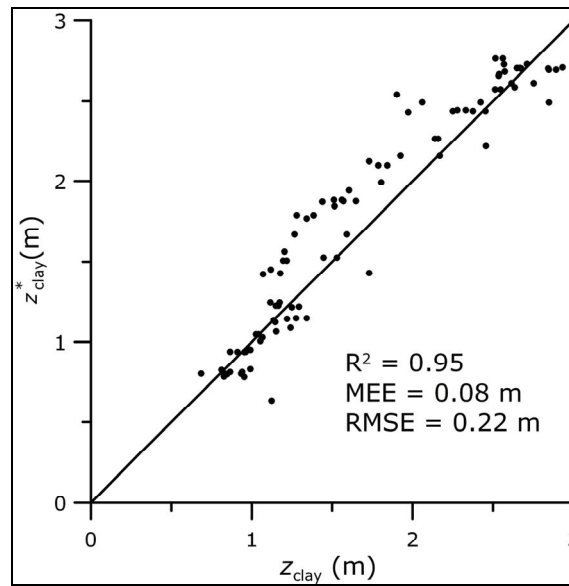


Fig. 6.5 Scatterplot of the predicted clay depth (z^*_{clay}) versus the observed depth (z_{clay}) with validation indices.

6.10 Paleolandscape beneath the loess cover

The soil surface elevation (Z) of the fields was gathered with LIDAR and visualized in Fig. 6.6(a). At each location, the 4 ECa measurements were converted into z^*_{clay} using the set of Eqs. (6.12), (6.13), (6.14) and (6.15) given the fitted depth response curves (Eqs. (6.10) and (6.11)). The interpolated map of z^*_{clay} was subtracted from Z and the resulting $Z - z^*_{\text{clay}}$ elevations are given in Fig. 6.6(b). To investigate the large variation in thickness of the loess cover, z^*_{clay} is displayed in Fig. 6.6(c). The kriging interpolations were carried out similarly to the $\text{ECa}_{v,1}$ but with a different variogram model (parameters given in Table 6.2). When comparing the current topography (Fig. 6.6(a)) with the paleolandscape beneath the loess cover (Fig. 6.6(b)), it will be clear that the paleolandscape is much more variable. Different gully systems occur on the paleorelief and are very pronounced on both sides of ridge B onto the Tertiary surface (Fig. 6.6(b)). When comparing the current elevation (Fig. 6.6(a)) with the paleolandscape (Fig. 6.6(b)), the boundary between the southern and northern watersheds differs. This was indicated on Fig. 6.6(a) and Fig. 6.6(b) with the dashed lines. The watershed boundary onto the paleolandscape cannot be correlated to the boundary on the current elevation due to the uneven loess cover near this boundary. Therefore, subsurface flow onto the paleolandscape will not coincide with the surface runoff. North of this watershed boundary, a small plateau (A) occurs onto the Tertiary surface (Fig. 6.6(b)) with a wide gully around it. To evaluate the continuity of these flow pathways, the Idrisi Kilimanjaro (Clark Labs, Worcester, MA, U.S.A.) modules RUNOFF (Jenson and Domingue, 1988) and

WATERSHED were applied to the paleolandscape. With this analysis, current and subsurface or past flow patterns were obtained and visualized in both Fig. 6.6(a) and Fig. 6.6(b). Comparing the current and past flow lines confirms the above observations about the watershed boundaries. Ridge B shows to be more pronounced on the Tertiary surface, because a flowline was modelled across it on the current surface (Fig. 6.6(a)). In general, the flowlines do not coincide on places with large variations in z_{clay}^* . Water that percolates through the loess cover flows from both flanks of ridge B and will accumulate in a gully at both sides of it. The wide gully around plateau A could also serve as a surface drainage path for the higher part of the study area.

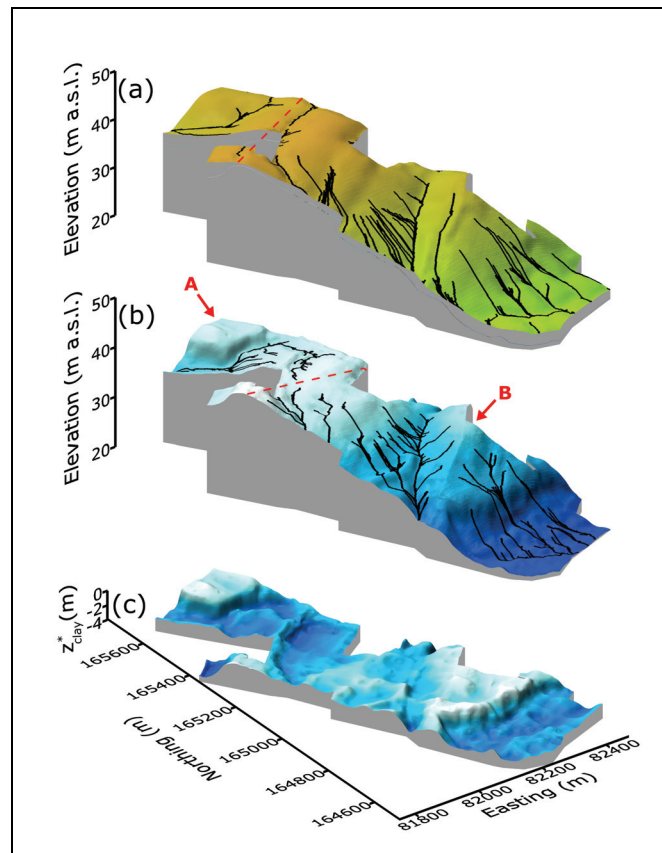


Fig. 6.6. (a) The elevation of the current surface with modelled flow patterns and (b) the elevation of the paleolandscape before the deposition of the loess cover with modelled flow patterns and (c) 3D-surface of the modelled depth-to-clay (z_{clay}^*).

6.11 Conclusions

The presented methodology presents an application of the prediction of sensor depth response curves in a two-layered soil. The depth response curves of an EMI instrument with multiple coil configurations were calculated in a rapid, effective and accurate way (R^2 of 0.74 and 0.77 for the perpendicular coil configurations; R^2 of 0.65 and 0.68 for the vertical coil configurations). Finally, the depth-to-clay was modelled accurately (RMSEE of 0.22 m), which allowed the detailed reconstruction of the paleolandscape beneath the loess cover. Flowlines visualized on this Tertiary surface represented past or subsurface drainage paths.

Chapter 7

Reconstructing a Holocene tidal channel in a polder area

7.1 Abstract

Conventional geological and soil maps of coastal lowlands are unable to account for the high lateral and vertical textural variability in the subsoil. Intensive sampling campaigns need to be carried out to quantify this variability. As an alternative, a proximal soil sensing procedure based on a single survey with the DUALEM-21S electromagnetic induction instrument was evaluated for mapping a Holocene tidal area in the coastal plain. A 6.5 ha study site was selected, next to the sea-dike. Probably, the positioning of the sea-dike next to the study site was related to the trace of tidal channels. Therefore, we evaluated the effectiveness of an electromagnetic survey with a DUALEM-21S instrument in mapping these features. Based on a limited amount of augerings complemented with EC-probe measurements of the different layers, a three-layered model was constructed with a clayey toplayer of 30 cm across the field, a clayey sublayer of the tidal channel over coarse sand. This model was supplemented by the measured electrical conductivity (EC) of the tidal clay and of the underlying sand. The four simultaneous ECa measurements allowed modelling the depth of the interface between the clay and coarse sand (z_{sand}) and the conductivity of the topsoil. The four measurements correspond to four different depth response functions that allow modelling z_{sand} without calibration observations. The predictions were validated with 20 depth observations on a 50 by 50 m grid and 16 observations on a transect with a distance of 10 m in-between. A correlation coefficient of 0.92, with an average error of 0.27 m, was found between the predicted and measured depths. So, the dense ECa measurements (2 by 2 m resolution) allowed us to build a three-dimensional surface of the depth of the tidal channel. This confirms that in medieval times a parallel dike had to be constructed to the west of the channel protecting the hinterland against flooding.

7.2 Introduction

Due to centuries of land use and soil tillage in most European countries, the topsoil has lost all traces about the past natural and anthropogenic history of the site. However, the subsoil might still contain useful information, but it is less accessible. In the past soil augerings were the major modus to conduct such investigations, but they remain punctual visits often aiming at reconstructing spatially continuous phenomena (Vitharana et al., 2008a). Moreover, most soil maps aimed at supporting agricultural developments and thus focused on the topsoil (Kværnø et al., 2007). On the other hand, geological maps represent an overview of the geographical distribution of outcropping deposits, often at a rather coarse scale preventing detailed interferences (Smirnov et al., 2008).

Soil and geological maps are of little use in the Holocene coastal plains because the sedimentary sequences are characterized by a high lateral and vertical variability (Bertrand and Baeteman, 2005). Yet they still contain information about the recent history of these landscapes, which were brought in culture in medieval times. Questions about the landscape build-up at that time and the building activities of dikes still remain open to modern historians and archaeologists.

The recent introduction of non-invasive proximal soil sensing systems offers new perspectives to study subsoil variability in detail providing several advantages over traditional invasive measurement methods (Saey et al., 2009b). These advantages include lower cost, increased efficiency and above all, much denser results (Sudduth et al., 2005). A promising technique is electromagnetic induction (EMI) (Brenning et al., 2008). With EMI, bulk measurements of the soil apparent electrical conductivity (ECa) can be obtained, which act as an indicator of important soil properties such as clay content, moisture content, and organic matter content (Sudduth et al., 2003; Domsch and Giebel, 2004; McBratney et al., 2005; Saey et al., 2009b). Additionally to the fact that geospatial ECa measurements are reliable, quick, and easy to obtain, they can be made mobile, allowing to cover larger areas fairly efficiently (Corwin and Lesch, 2004).

The objective of this study was to develop and apply a methodology to investigate a Holocene tidal area which was diked-in during medieval times using sensed ECa data.

7.3 Regional setting

The study area is a 6.5 ha agricultural field as a part of an 89 ha area which was geophysically scanned before the construction of a golf court. The study site was located in the western part of the coastal plain of Belgium (central coordinates: 51°06'48''N and 2°42'04''E) (Fig. 7.1). This plain is part of the former wetlands along the southern North Sea Area, which stretch from Calais in northern France to Skagen in the north of Denmark. The quaternary sediments in the coastal plain consist mainly of alternations of sand, silt, clay and peat beds which have been deposited due to interaction of sea level rise, palaeotopography, sediment supply and creation of accommodation space (Baeteman et al., 1999; Baeteman, 2008).

In the larger study area, which has been part of the IJzer Estuary and palaeovalley, late-Holocene sand and silt deposits are dominating. Sand-filled tidal channels were formed during the *La Tène* (from 560 year BC) and Roman period, incising through the older deposits and causing peat erosion. Finally, the cannels were filled with clayey sediments under calm and smooth conditions, which started beyond the 7th-century AD (Baeteman, 2008). Unprocessed data of the recent archaeological and pedological research will inform us about the exact end date of the infill. The soil characteristics are rather uniform throughout the entire study site. The topsoil (plough layer and the bioturbated zone beneath) consists of clayey sediments overlaying the sandy deposits.

The area was geophysically scanned to support archaeological excavations which were carried out before the construction of a golf court.

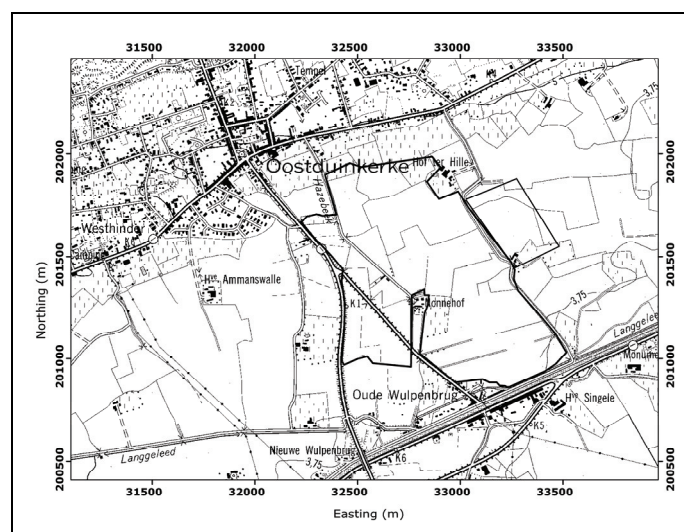
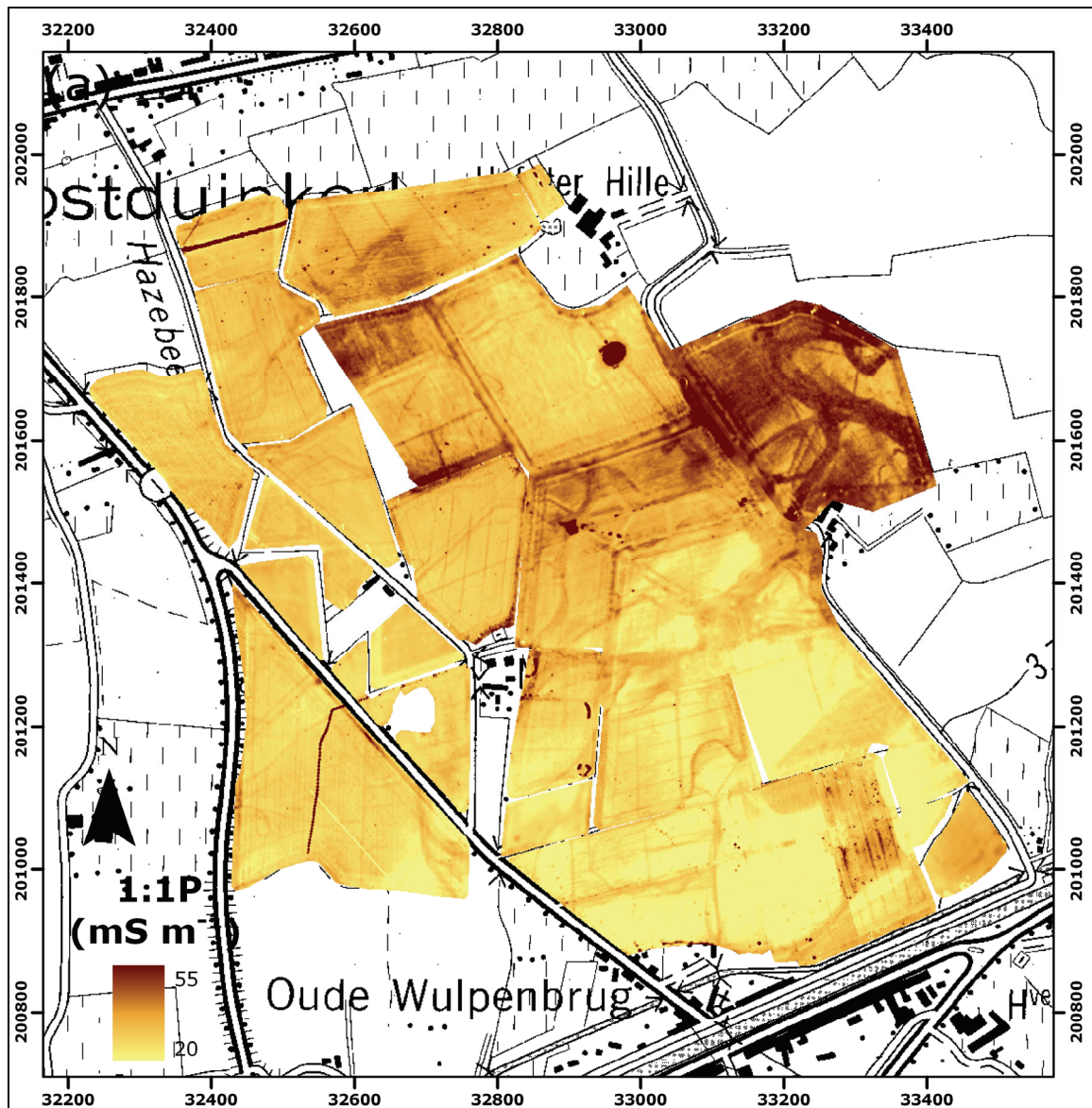
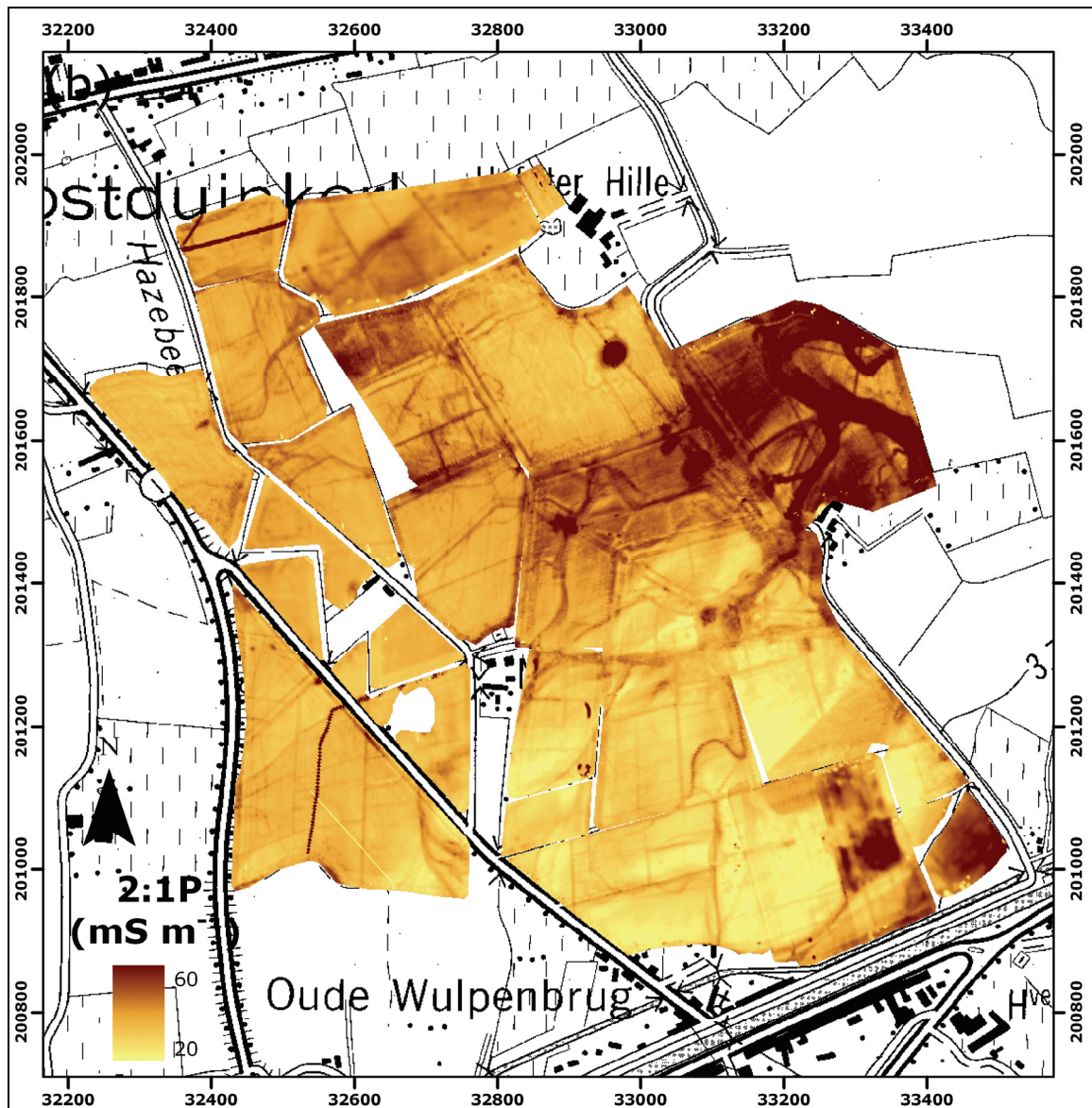


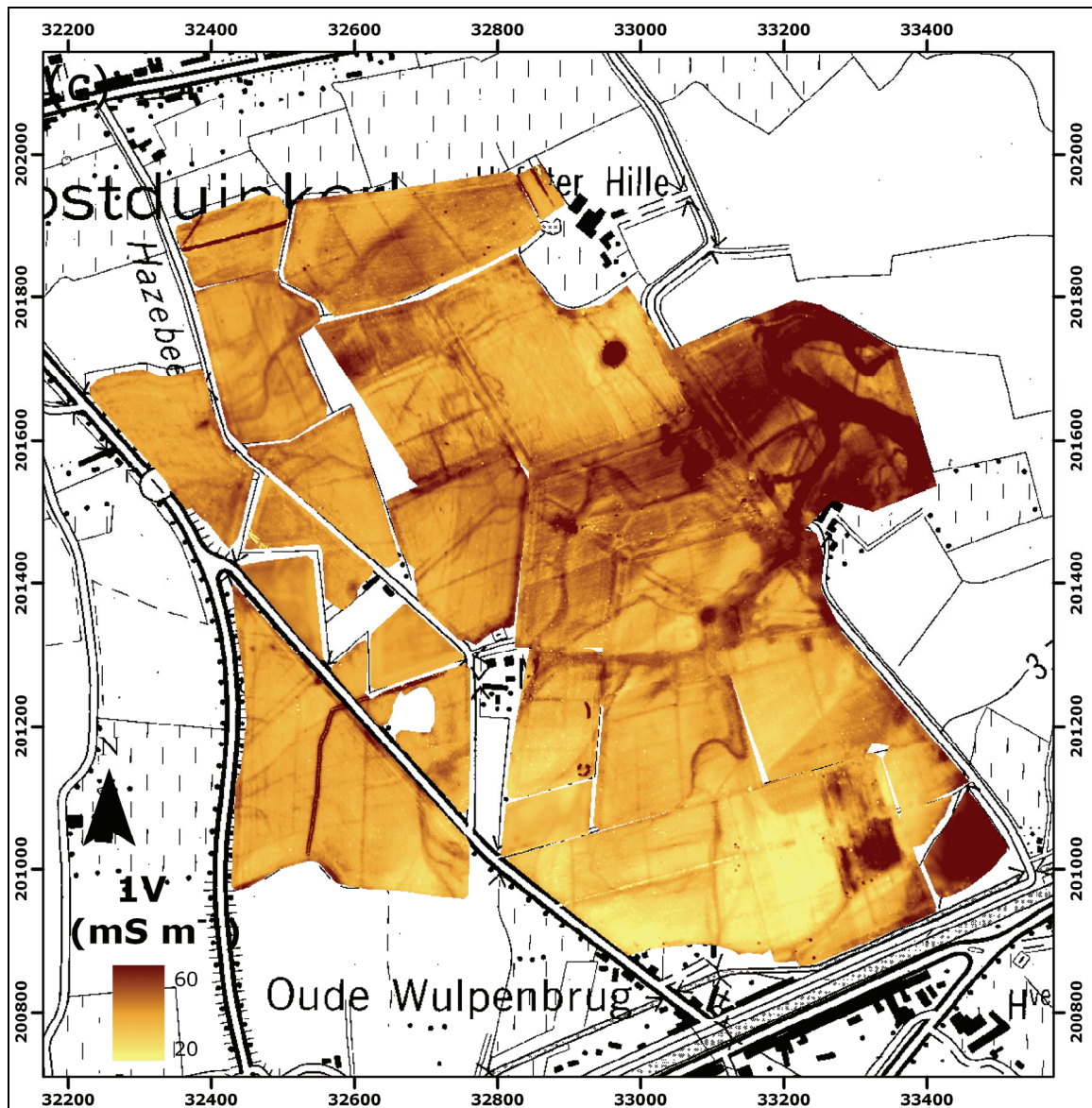
Fig. 7.1. Localization of the study site on the topographic map

7.4 ECa survey

The four ECa measurements of the entire 89 ha are given in Fig. 7.2. A lot of features can be seen on the four ECa measurements. When we focus on the 6.5 ha study site 2, Table 7.1 shows that the mean and maximum values of the $ECa_{p,2,1}$ and $ECa_{v,2}$ are almost identical, and larger than the shallower $ECa_{p,1,1}$ and the deeper $ECa_{v,2}$, indicating that on average the topsoil and deeper material contains less clay than the top 1.0 – 1.5 m. The negative minimum value of the $ECa_{p,1,1}$ (-28 mS m^{-1}) and $ECa_{p,2,1}$ (-36 mS m^{-1}) and the high maximum value (267 mS m^{-1}) of the $ECa_{p,1,1}$ are caused by anomalies like metal objects situated in the subsoil. The standard deviations are similar for the four ECa measurements.







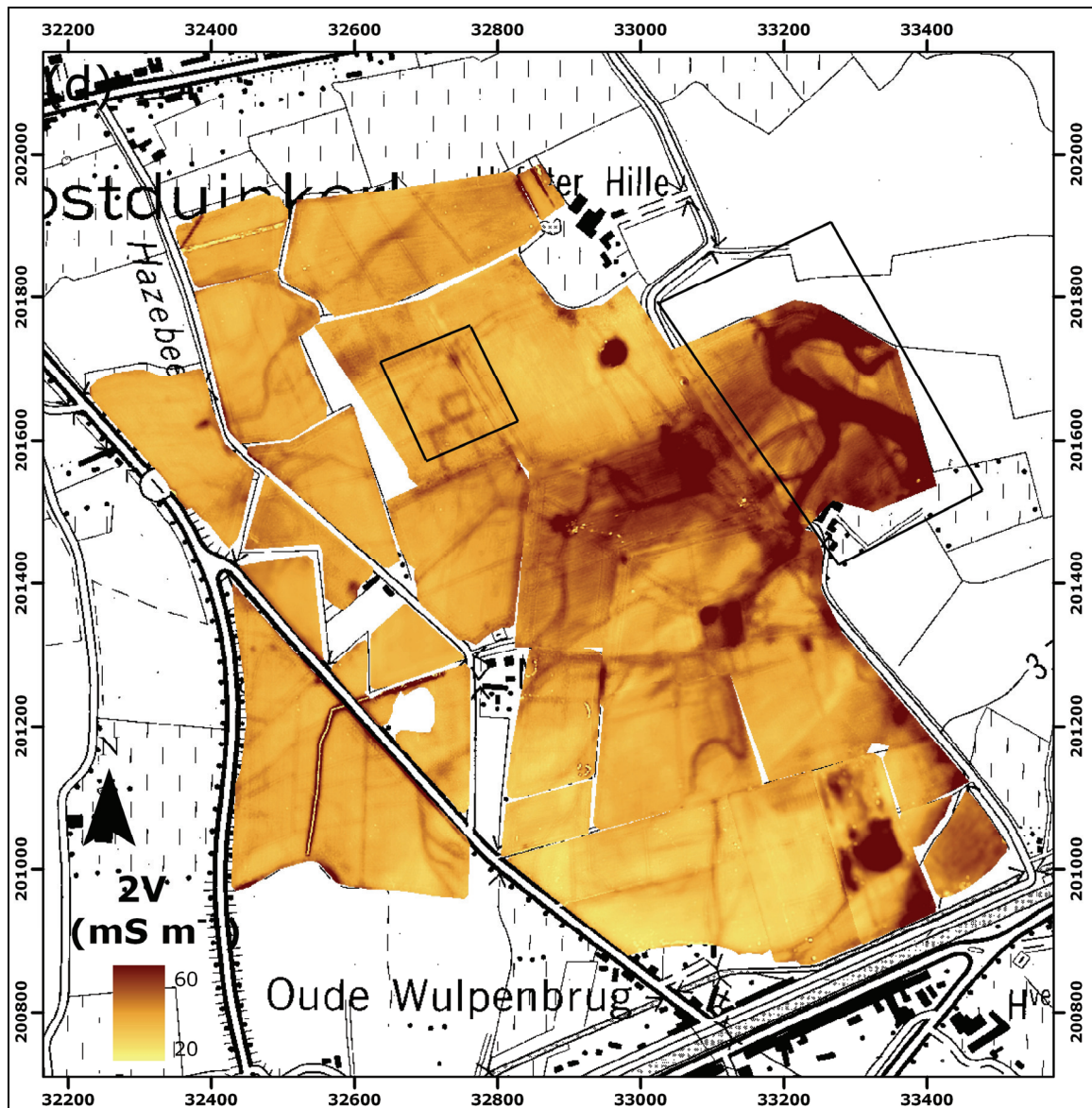


Fig. 7.2. Measured apparent electrical conductivity map in the 1.1 m - perpendicular coil configuration ($ECa_{p,1.1}$) (a), in the 2.1 m - perpendicular coil configuration ($ECa_{p,2.1}$) (b), in the 1 m - vertical coil configuration ($ECa_{v,1}$) (c) and in the 2 m - vertical coil configuration ($ECa_{v,2}$) (d), with localization of the study site 1 (black box right) and study site 2 (black box left).

Table 7.1. Descriptive statistics (*m*: mean, min: minimum, max: maximum, *s*: standard deviation) of ECa_{p,1,1}, ECa_{p,2,1}, ECa_{v,1} and ECa_{v,2} for the study site (39326 measurement points).

Variable	<i>m</i>	min	max	<i>s</i>
	(mS m ⁻¹)	(mS m ⁻¹)	(mS m ⁻¹)	(mS m ⁻¹)
ECa _{p,1,1}	46	-28	267	7
ECa _{p,2,1}	57	-36	130	9
ECa _{v,1}	58	23	140	9
ECa _{v,2}	54	11	96	10

Ordinary kriging was used to interpolate the measurements to a 0.5 by 0.5 m grid. A maximum of 64 neighbours was used within a circular search area with radius of 20 m around the location being interpolated. The spatial structures of the ECa measurements were modelled using simple and nested models (Fig. 7.3). The variogram of the ECa_{p,1,1} has a substantial higher nugget variance than the other measurements. This indicates that there is more random noise in the ECa_{p,1,1} measurements. The variogram of the ECa_{v,2} measurements contains a Gaussian model, which indicates that these are more spatially continuous compared with the other ECa measurements.

Fig. 7.4 shows the interpolated ECa maps of the study area. The patterns appear to be analogue for the four simultaneous measurements, certainly for the ECa_{p,2,1}, ECa_{v,1} and ECa_{v,2}, but the absolute values differ. Indications of a clear fluvial structure are visible on the ECa maps, although no trace of it was visible at the surface (the topography is flat). This fluvial structure is less clear on the ECa_{p,1,1} map, probably because it is most clearly differentiable below the topsoil. This fluvial structure was most likely a tidal channel which was connected with the North Sea. Additional linear features cross over the field, which indicate more recent human activities (like the installation of drainage tubes).

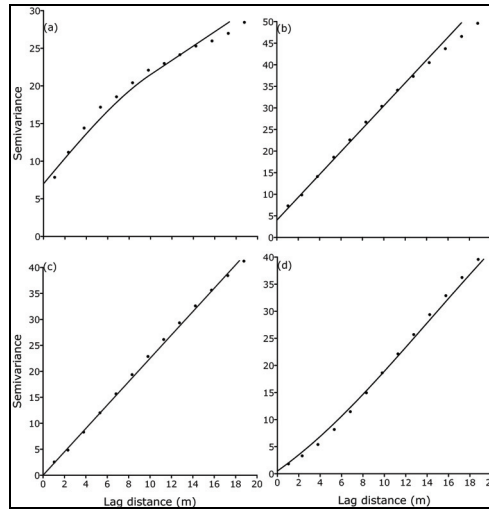


Fig. 7.3. Variograms of the apparent electrical conductivity in the 1.1 m – perpendicular coil configuration (a), in the 2.1 m – perpendicular coil configuration (b), in the 1 m – vertical coil configuration (c) and in the 2 m – vertical coil configuration (d).

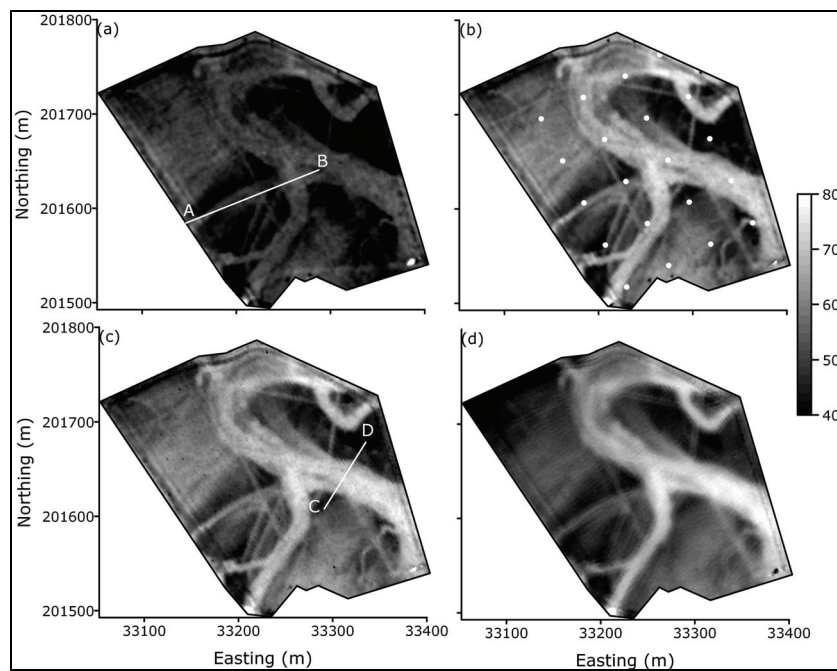


Fig. 7.4. Interpolated apparent electrical conductivity (ECa) map in the 1.1 m – perpendicular coil configuration with localization of transect AB (a), in the 2.1 m – perpendicular coil configuration with 20 points in a 50 by 50 m grid (b), in the 1 m – vertical coil configuration with localization of transect CD (c) and in the 2 m – vertical coil configuration (d) (all in mS m^{-1}).

7.5 Depth observations

To complement the sensor measurements with field verifications we positioned a transect “AB” in such a way that both high and low ECa values were visited (Fig 7.4(c)). Along this 150 m long transect, 16 observations were made by a hand auger at 10 m interval. At each of these points, the thickness of the plough layer and the depth of the interface between the marine clay and the underlying coarse sand (z_{sand}) was noted. This distinction was clearly observable. Fig. 7.5 shows the result as a cross section. In general, the sand was found at a depth of 1 to 1.2 m. However, when we reached the tidal channel, this interface dropped to a depth of about 2.6 – 2.8 m (from about 105 m along the transect onwards). It will be clear that this finding has consequences in terms of agricultural land use (nutrient availability and leaching, water availability, etc.), but also for other land activities such as building construction.

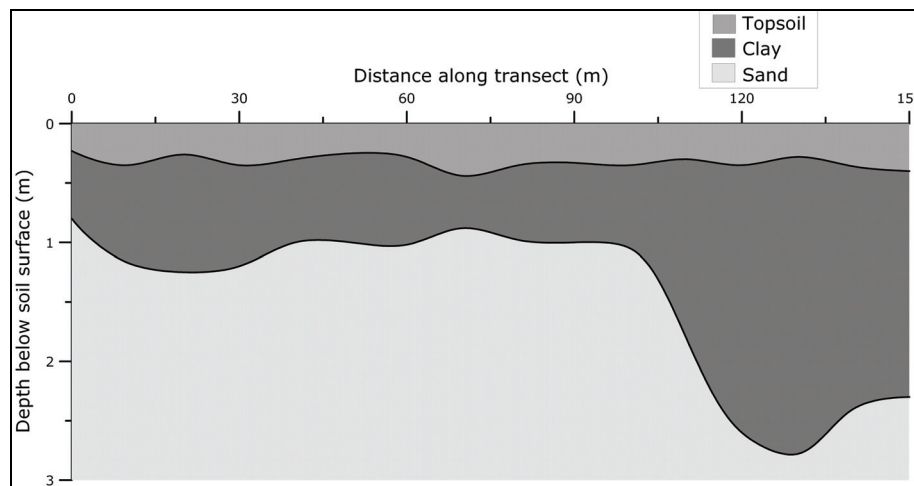


Fig. 7.5. Build-up of the three-layered soil along transect AB.

7.6 Punctual EC-measurements

The standard EC-probe set for soil conductivity measurements consists of an EC-probe and an earth resistivity meter. Measurement of the soil resistivity using four electrodes is based on the Wenner-method, applied by Rhoades and Van Schilfgaarde (1976) for the development of an EC-probe.

Since at each spot a hole has to be augered, this sensor can be used only for a limited number of punctual measurements. These can act, however, as calibration measurements for the proximal soil sensing data. Using the EC-probe, 20 measurements of the three different layers

were conducted where possible, according to a 50 by 50 m grid schema laid over the field (Fig. 7.4(b)). Only measurements at a depth more than 30 cm above or below each interface were retained to obtain the average EC. Moreover, the limited length of the EC-probe rod (1 m) diminished the amount of measurements substantially. From these, the EC of the topsoil (EC_{top}) was variable across the study area, the EC of the clay layer (EC_{clay}) $109 \pm 6 \text{ mS m}^{-1}$ (8 measurements) and of the sand layer (EC_{sand}) it was $21 \pm 4 \text{ mS m}^{-1}$ (4 measurements), at 25°C . These values were assumed to be representative for the two subsoil layers across the field so that they could be used to model the depth of the interface.

7.7 Depth modelling

The four simultaneous ECa measurements obtained with the quadruple-array DUALEM-21S sensor were used to model and map z_{sand} . In a three-layered soil build-up, the measured ECa can be estimated by summing the conductivities and depth-weighted contributions of each layer. The conductivities of the clay and sand layer were taken from the EC-borehole measurements and assumed homogeneous across the study site. The conductivity of the topsoil (EC_{top}) was modelled because it varied strongly across the field. These were used to model the depth of the interface between the clay and the sand. Due to the characteristic depth response profiles for each coil configuration, the following four equations could be formulated, taking the height of the DUALEM-21S sensor above the soil surface into account (0.16 m):

$$ECa_{p,1,1} = [R_{p,1,1}(0.3 + 0.16) - R_{p,1,1}(0.16)] \cdot EC_{top}^* + [R_{p,1,1}(z_{sand}^* + 0.16) - R_{p,1,1}(0.3 + 0.16)] \cdot EC_{clay} + [1 - R_{p,1,1}(z_{sand}^* + 0.16)] \cdot EC_{sand} \quad [7.1]$$

$$ECa_{p,2,1} = [R_{p,2,1}(0.3 + 0.16) - R_{p,2,1}(0.16)] \cdot EC_{top}^* + [R_{p,2,1}(z_{sand}^* + 0.16) - R_{p,2,1}(0.3 + 0.16)] \cdot EC_{clay} + [1 - R_{p,2,1}(z_{sand}^* + 0.16)] \cdot EC_{sand} \quad [7.2]$$

$$ECa_{v,1} = [R_{v,1}(0.3 + 0.16) - R_{v,1}(0.16)] \cdot EC_{top}^* + [R_{v,1}(z_{sand}^* + 0.16) - R_{v,1}(0.3 + 0.16)] \cdot EC_{clay} + [1 - R_{v,1}(z_{sand}^* + 0.16)] \cdot EC_{sand} \quad [7.3]$$

$$ECa_{v,2} = [R_{v,2}(0.3 + 0.16) - R_{v,2}(0.16)] \cdot EC_{top}^* + [R_{v,2}(z_{sand}^* + 0.16) - R_{v,2}(0.3 + 0.16)] \cdot EC_{clay} + [1 - R_{v,2}(z_{sand}^* + 0.16)] \cdot EC_{sand} \quad [7.4]$$

With $R_{p,x}(z)$ and $R_{v,x}(z)$ the cumulative responses above a depth z for the perpendicular and vertical dipole mode respectively and transmitter-receiver coil spacing x , $EC_{clay} = 109 \text{ mS m}^{-1}$ and $EC_{sand} = 21 \text{ mS m}^{-1}$.

At each of the 39 326 measurement locations, the nonlinear Eqs. (7.1), (7.2), (7.3) and (7.4) were combined to model EC_{top}^* and z_{sand}^* . This system was solved with Matlab using the Levenberg-Marquardt algorithm (Marquardt, 1963).

7.8 Validation

The accuracy of the proposed model to predict z_{sand}^* was evaluated by investigating at 20 locations, laid out as a grid of 50 by 50 m supplemented with the 16 points located on transect AB. At these locations, the observed depths were compared with the modelled depths (Fig. 7.6). The MEE and RMSEE were respectively 0.08 m and 0.27 m. The Pearson correlation coefficient between z_{sand} and z_{sand}^* was 0.92, which is highly significant at $\alpha = 0.05$. Therefore, the modelled relationship was found to poses a negligible bias, to be reasonably accurate and to correlate well with the observed depths. Moreover, our assumption that the EC of the three layers could be represented by the average value obtained with the EC-probe seemed to be reasonable.

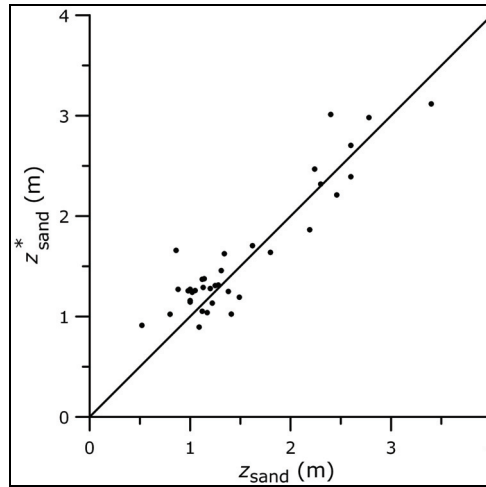


Fig. 7.6. Scatterplot of the predicted interface depth (z_{sand}^*) vs. the observed depth (z_{sand}).

7.9 Reconstruction of the tidal channel

The soil surface elevation (Z) was also available from our GPS measurements, with an absolute vertical accuracy in the order of 20-30 cm. However, the relative point-by-point accuracy was much better, allowing the data to construct a surface of Z . It was interpolated with ordinary kriging and the result is given in Fig. 7.7(a). z_{sand}^* was also interpolated using ordinary kriging under similar conditions as the ECa maps (Fig. 7.4). Finally, z_{sand}^* was subtracted from Z and the resulting map is shown in Fig. 7.7(b), representing the depth of the interface below the soil surface. This result visualizes the channel pattern and its dimensions. Along transect CD (Fig. 7.4(c)) the tidal channel has a width of 53 m with a depth of maximally 2.8 m. Its cross-section is approximately 49 m^2 , which means that with a hypothetical but reasonable water velocity of 1 m s^{-1} , a flux of $49\,000 \text{ l s}^{-1}$ could flow through it. The entire volume of this tidal channel within the study field was calculated to be $71\,940 \text{ m}^3$.

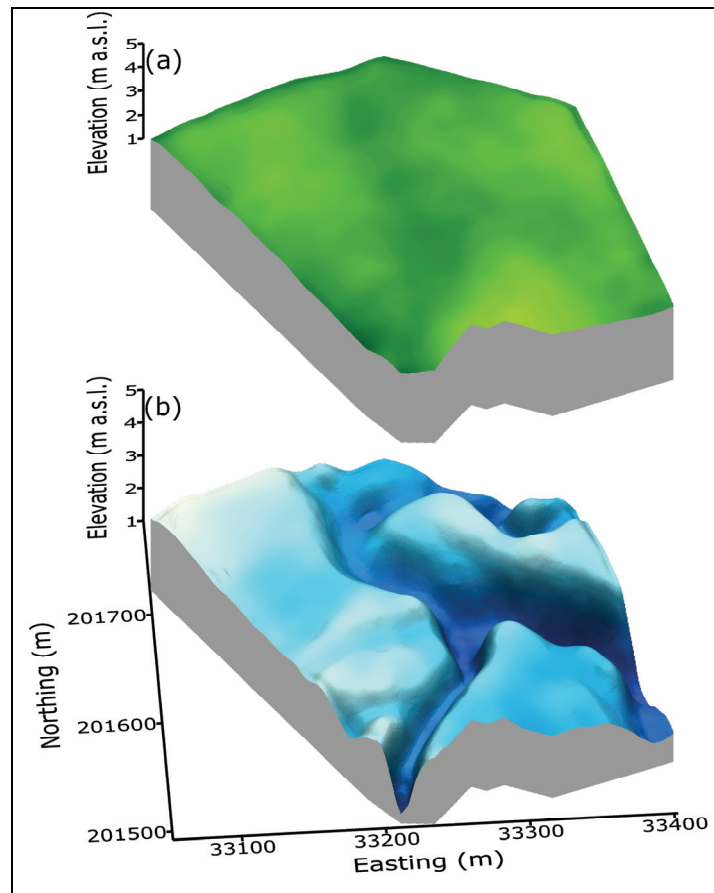


Fig. 7.7. The elevation of the current surface (a) and the elevation of the tidal channel (b).

It will be clear that such a tidal channel able of passing such large volumes of sea water in the area represented a potential treat for flooding and had to be diked-in before the area could be developed into cultivated land. During Roman times, or even before, it is likely that smaller ships could navigate on it towards or from the sea.

7.10 Conclusions

The presented methodology allowed an accurate prediction of the depth between two contrasting layers in a three-layered soil based on one survey with the DUALEM-21S EMI proximal sensor (RMSEE of 0.27 m). However, the homogeneity and the conductivities of different soil horizons had to be determined from a limited number of borehole EC-measurements. This procedure offers a rapid, effective and accurate way to reveal the ancient tidal channel. It definitely solves some historical and paleo-archeological questions about the medieval landscape. These findings contribute to the knowledge of the past, current en future perspective of coastal plains.

Chapter 8

EC-depth modelling with a multi-signal EMI sensor to accentuate archaeological features¹

8.1 Abstract

Multiple apparent electrical conductivity (ECa) measurements with an electromagnetic induction (EMI) sensor frequently reveal analogue patterns caused by conductive features in the soil. A procedure was proposed to highlight different archaeological anomalies based on combinations of the simultaneous ECa measurements with the DUALEM-21S instrument. A 3.5 ha study site was selected and 0.79 ha of that area has been recorded by archaeological excavation. Since the majority of upper archaeological features was found between the plough layer and 1.0 m below soil surface, a set of 4 equations was developed to model the EC within that predefined depth interval. This set of four equations employed the four depth response curves, specific for the four DUALEM-21S coil configurations. The modelled conductivity between 0.5 and 1.0 m (EC^*_2) showed a larger variability across the archaeological features than the raw EC data. To quantify the added value of this modelled conductivity, EC^*_2 and measured ECa were compared with the rasterized map of the archaeological traces. Finally, the EC^*_2 map proved to distinguish better between the archaeological features and the ‘empty’ background. This technique allowed the highlighting of vague anomalies in the simultaneous DUALEM-21S ECa measurements.

¹Modified from: Saey, T., Lehouck, A., Van Meirvenne, M., De Smedt, P., Meerschman, E., Islam, M. M., Meeuws, F., Cockx, L., 20___. EC-depth modelling with a multi-signal EMI sensor to accentuate archaeological features. Archaeological Prospection, Submitted.

8.2 Introduction

Geophysics provides effective solutions for the non-invasive exploration of some archaeological sites. Forte and Pipan (2008), Neubauer et al. (2002) and Gaffney et al. (2005) have shown the value of geophysics in the preliminary study of spatial patterning in artifact variability. In most cases, geophysical techniques are used for detecting anomalies interpreted as buried features, but an evaluation by archaeological excavation is less common. Among geophysical methods, electromagnetic induction (EMI) is noteworthy as a tool in landscape archaeology and contextual site analysis. With EMI, areas of archaeological interest can be mapped with high lateral and vertical resolution to delineate feature densities of human and natural origin (see i.e. Simpson et al., 2008; Rodrigues et al., 2009). Consequently, EMI can be used in some cases as a reference guide to direct the placement of excavation activities and thus reducing the costs of exploration stages (Venter et al., 2006). Generally, EMI determines the electrical conductivity and magnetic susceptibility of soils from observations of induced electromagnetic fields. The magnetic susceptibility from EMI instruments is considered useful for archaeology because it is well suited to image traces of human occupation, such as foundations, ditches, pits and in some cases even post holes. However, the success of magnetic mapping depends on the contrasts in magnetic soil properties (Lück et al., 2003).

Previously, several archaeological studies used the apparent electrical conductivity (ECa) with the EM38 instrument in the vertical coil configuration, thus with one transmitter and one receiver coil. Simpson et al. (2008) showed the ECa maps to reveal the ditch of a moated site, a large channel part of a marine tidal system and large volumes of brick rubble. Persson and Olofsson (2004) found a former excavation tunnel in their ECa measurement. Lück et al. (2003) identified small structures such as posts of pits within their ECa map and confirm the potency for prospecting archaeological ditch systems. The use of several receivers to improve the depth of investigation and the horizontal definition of inhomogeneities was demonstrated by Simpson et al. (2009b). Recently, the DUALEM-21S was developed, which is able to measure both ECa and MSa at two coil orientations for two coil separations (Saey et al., 2009a). Because of their specific spatial sensitivity, the multiple coil configurations have the potential to detect more archaeological features than individual signals. However, EMI sensors with multiple coil configurations have been rarely used for archaeological prospecting. Nevertheless, Simpson et al. (2009b) revealed new anomalies by subtracting two DUALEM-21S ECa measurements as small anomalies in a single measurement can be masked by highly conductive features in the soil (for example a clayey substrate). Generally, EMI instruments are characterized by a continuous depth response function, determined by

the instrument frequency, coil spacing and orientation. Therefore, the ECa is an integration of the conductivities (EC) of different features in the subsoil, each with a response determined by their depth sensitivity function (McNeill, 1980b). Based on this depth response function, the depth of exploration (DOE) is defined as the depth at the 70 % cumulative response. This implies that 30 % of the cumulative response comes from features below the DOE (Morris, 2009). Therefore, contrasting features with a large vertical extent (like a Tertiary substrate) have a substantial contribution to the measured ECa (Saey et al., 2009a), even if situated below the DOE. Adversely, most archaeological features have a limited vertical depth extent, which makes them difficult to differentiate within a single ECa measurement. Moreover, the archaeological features in arable land are rarely preserved within the ploughed layer. Therefore, our aim is to combine the four simultaneous ECa measurements obtained with the DUALEM-21S to highlight archaeological anomalies just below the ploughed topsoil. This filtering technique must enable the archeologist to recognize shallow archaeological features non-invasively.

8.3 Site description

The 3.5 ha study site 2 (Fig 8.1 and Fig 8.2(d)) is also a part of the 89 ha area which was geophysically scanned before the construction of a golf court (central coordinates: 51°06'46''N and 2°41'38''E).

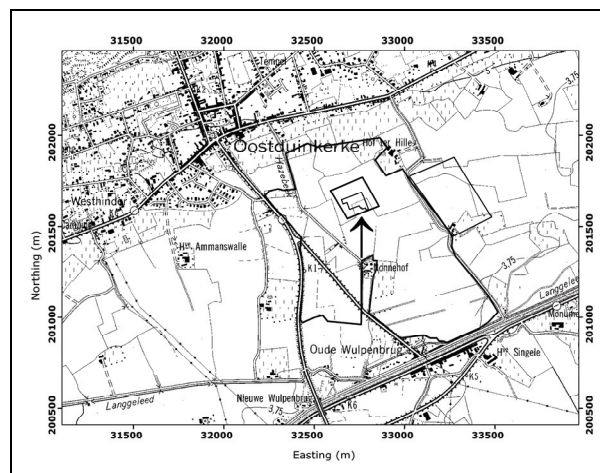


Fig. 8.1. Topographic map with indication of the boundaries of study and excavation sites (see arrow).

In 2000, the municipality of Koksijde took the initiative to establish an 85 ha golf court on their territory. Because of the destructive character of these landscape interventions, this 85 ha area had to be investigated archeologically. The terrain will be disturbed by diggings and

embankments. Where the water features will be scheduled, very deep diggings will disturb the original soil profile and archive.

A major slots review is frequently used as the only technique for the archaeological prospecting of large areas. Because of cost and labour constraints, a combination of different methods with limited soil surgery were used on this 85 ha golf court: historical research, landscape-analysis, field prospecting and geophysics are the basis for the investigation. Some reasons for this choice were: (i) The archaeological soil archive from the Late Middle Ages is situated nearby the soil surface, (ii) The parcelling goes back to the 12th-13th century, which implies that remains from these periods are frequently localized nearby the pattern of parcel divisions (iii) Big differences in soil texture are assumed to be present in this area. Therefore, geophysical prospecting techniques with EMI are designated to map spatially the anthropogenic and natural soil disturbances and (iv) High groundwater levels and the presence of unexploded war ammunition put constraints on the possibilities for the digestion of the area. With this method, trenches and excavations can be targeted more efficiently and in better conditions.

8.4 Historical and archaeological setting

During the Carolingian period, the environment was well-developed in a cultural landscape (deduced from recent archaeological research). The presence of some scattered farms could be documented during the excavation campaign. In this study, the medieval site was called *einzelhöfe* and was inhabited by a group of fishermen between the (late?) 10th and the 12th century AD. This site is part of the scattered farmsteads from the fishery village of Oostduinkerke (some 800 m to the north), which probably developed along the southern bank of an old tidal branch of the river IJzer. This old branch can be seen as the main tidal river of the area in that period (Lehouck, 2010).

The settlement is characterized by a bipartite structure of a residential upper court (area of the farmstead) and a non-residential lower farmyard. This kind of feature is typical for late medieval moated sites, but is not well documented for the earlier period. Study site 2 was discovered in 2008 by field surveying (micro topography, field walking and a coarse auger campaign), however the bipartite structure was indistinguishable using traditional methods of archaeological prospection.

8.5 ECa survey

The ECa of the 3.5 ha study site was investigated with the DUALEM-21S proximal EMI soil sensor as a part of the investigation of the 85 ha golf court. Therefore the sensor was put in a non-metal sled and pulled behind an all-terrain vehicle at about 6-10 km h⁻¹ crossing the field at parallel lines 1.7 m apart.

Table 8.1 shows the summary statistics of the four ECa measurements taken with the DUALEM-21S sensor on 20280 locations at the study site. The mean values of the ECa increase with increasing DOE, but decrease from the 1V (DOE = 1.55 m) to the 2V (DOE = 3.18 m) coil configuration. Therefore, the larger the measured soil volume, the higher the conductivity, this up to a depth of approximately 1.55 m. Between a depth of 1.55 m and 3.18 m, low conductive material must be present which decreases the ECa of the measured soil volume. The negative minimum value of ECa_{v,1} was caused by anomalies in the subsoil like small metal objects. Fig. 8.2 shows the ECa measurements of the study site converted to a reference temperature of 25°C. To obtain estimates of variables at unsampled locations, ordinary point kriging (OK) was used as an interpolation method (Goovaerts, 1997). In this study, a minimum of 4 neighbours was used within a circular search area with a radius of 10 m around the location being interpolated. The spatial structure of the variables was represented by variogram models, which were used to assign weights to the neighbouring points. On Fig. 8.2, different linear, sinuous and square structures, which can be assigned to fluvial, medieval and recent activities, were observed across the study site, most obvious on the ECa_{v,1} and ECa_{p,2,1} measurements,

Table 8.1. Descriptive statistics (*m*: mean, min: minimum, max: maximum, *s*: standard deviation) of ECa_{p,1,1}, ECa_{p,2,1}, ECa_{v,1} and ECa_{v,2} for the 20280 measurements on the 3.5 ha study site (in mS m⁻¹ after conversion to a reference temperature of 25°C).

Variable	<i>m</i>	min	max	<i>s</i>
ECa _{p,1,1}	36	17	88	6
ECa _{p,2,1}	42	28	71	6
ECa _{v,1}	43	-6	67	5
ECa _{v,2}	40	16	60	4

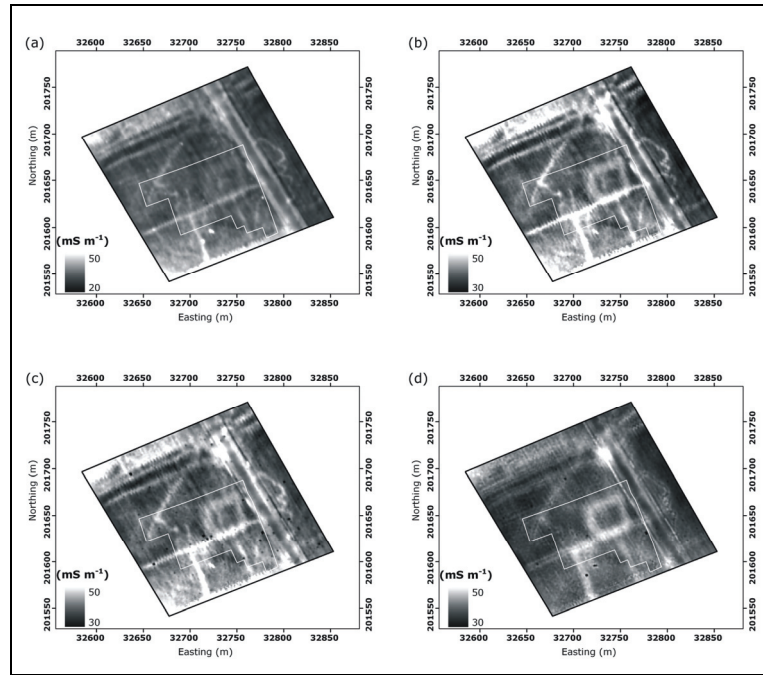


Fig. 8.2. Measured apparent electrical conductivity map (converted to a reference temperature of 25°C) in the 1.1 m - perpendicular coil configuration ($ECa_{p,1.1}$) (a), in the 2.1 m - perpendicular coil configuration ($ECa_{p,2.1}$) (b), in the 1 m - vertical coil configuration ($ECa_{v,1}$) (c) and in the 2 m - vertical coil configuration ($ECa_{v,2}$) (d), with localization of the excavated site (white line).

An excavation site of 0.79 ha was selected (white boundary on Fig. 8.2) based on historical research and the presence of distinct square and linear patterns on the DUALEM-21S ECa measurements. The topsoil was removed to improve the visibility of the archaeological traces and structures. A detailed drawing of the features was made and digitized at the end of 2009 (Fig. 8.3). On the excavation site, we assume that all natural and human-made features of medieval time can be distinguished because they manifest as very compact and clayey structures in the sandy subsoil. The farmstead moat, with the bottom situated approximately 1 meter below ground level, is filled up with compact greyish homogeneous silty or clayey material with embedded artifacts and charcoal fragments, even as the shallow and smaller farmyard ditch. The infill of the ditched field boundary is largely the same. However, a much more organic infill with remains of reed and wood could be observed. This structure was fossilized more recently (during the mid 20th-century AD). The freakish small tidal creeks are filled up with a homogeneous and very compact clay sediment with numerous shells of *scrobicularia* sp. and *cerestoderma* sp. embedded.

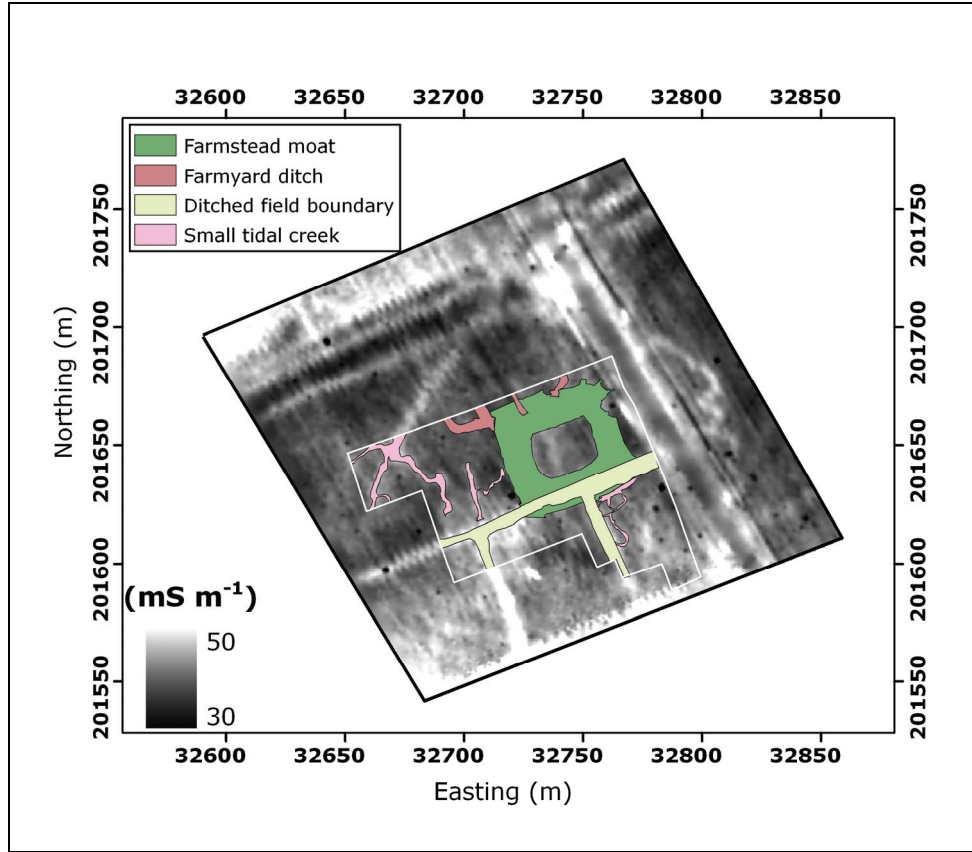


Fig. 8.3. Measured apparent electrical conductivity map in the 1 m - vertical coil configuration ($EC_{a,v,1}$) with indication of the excavated archaeological features.

8.6 EC-depth modelling

The four simultaneous EC_a measurements obtained with the DUALEM-21S sensor have their own depth sensitivity given by Eqs. (2.9) and (2.11). In a layered soil build-up, the measured EC_a can be estimated by summing the conductivities (EC) and depth-weighted contributions of each delimited layer. Inversely, the EC of a defined layer can be determined based on the measured EC_a and the depth sensitivity curves. By establishing a set of four equations, the EC of three layers with predefined depth boundaries can be estimated accurately given the four measured EC_a values.

Because field prospecting revealed that the soil archive was situated nearby the soil surface, depth intervals were chosen accordingly. Most of the remaining archaeological features were found between 0.5 m and 1 m depth or just below the ploughed layer. Therefore, our focus lies on modelling the EC between these depths. The aim was to transform the four EC_a measurements in three EC's between 0 m and 0.5 m (EC^*_1), between 0.5 m and 1 m (EC^*_2) and below 1 m (EC^*_3). Due to the characteristic depth response profiles for each coil

configuration, the following four equations were formulated, taking the height of the DUALEM-21S sensor above the soil surface into account (0.16 m):

$$ECa_{p,1,1} = [R_{p,1,1}(0.5 + 0.16) - R_{p,1,1}(0.16)] \cdot EC_1^* + [R_{p,1,1}(1 + 0.16) - R_{p,1,1}(0.5 + 0.16)] \cdot EC_2^* + [1 - R_{p,1,1}(1 + 0.16)] \cdot EC_3^* \quad [8.1]$$

$$ECa_{p,2,1} = [R_{p,2,1}(0.5 + 0.16) - R_{p,2,1}(0.16)] \cdot EC_1^* + [R_{p,2,1}(1 + 0.16) - R_{p,2,1}(0.5 + 0.16)] \cdot EC_2^* + [1 - R_{p,2,1}(1 + 0.16)] \cdot EC_3^* \quad [8.2]$$

$$ECa_{v,1} = [R_{v,1}(0.5 + 0.16) - R_{v,1}(0.16)] \cdot EC_1^* + [R_{v,1}(1 + 0.16) - R_{v,1}(0.5 + 0.16)] \cdot EC_2^* + [1 - R_{v,1}(1 + 0.16)] \cdot EC_3^* \quad [8.3]$$

$$ECa_{v,2} = [R_{v,2}(0.5 + 0.16) - R_{v,2}(0.16)] \cdot EC_1^* + [R_{v,2}(1 + 0.16) - R_{v,2}(0.5 + 0.16)] \cdot EC_2^* + [1 - R_{v,2}(1 + 0.16)] \cdot EC_3^* \quad [8.4]$$

with $R_{p,x}(z)$ and $R_{v,x}(z)$ the cumulative responses above a depth z for the perpendicular and vertical dipole mode and transmitter-receiver coil spacing x . At each of the 20280 measurement locations, this set of equations was solved to the unknown EC_1^* , EC_2^* and EC_3^* using the Levenberg-Marquardt algorithm (Marquardt, 1963). The three maps are given in Fig. 8.4. EC_1^* (Fig. 8.4a) shows that the topsoil (0 – 0.5 m) contained little variability. On the contrary, the EC_2^* map (Fig. 8.4b) accentuates the recorded archaeological features. Especially the farmyard ditch becomes more pronounced, compared to the four single ECa measurements (Fig. 8.2). The range of the EC_2^* values is larger compared to the single ECa ranges, resulting in more distinct differences between the archaeological traces (Fig. 8.4b). On Fig. 8.4c, the farmstead moat and farmyard ditch disappear. The presence of ditched field boundaries and small tidal creeks on this modelled EC_3^* reveal the existence of these features below 1 m depth.

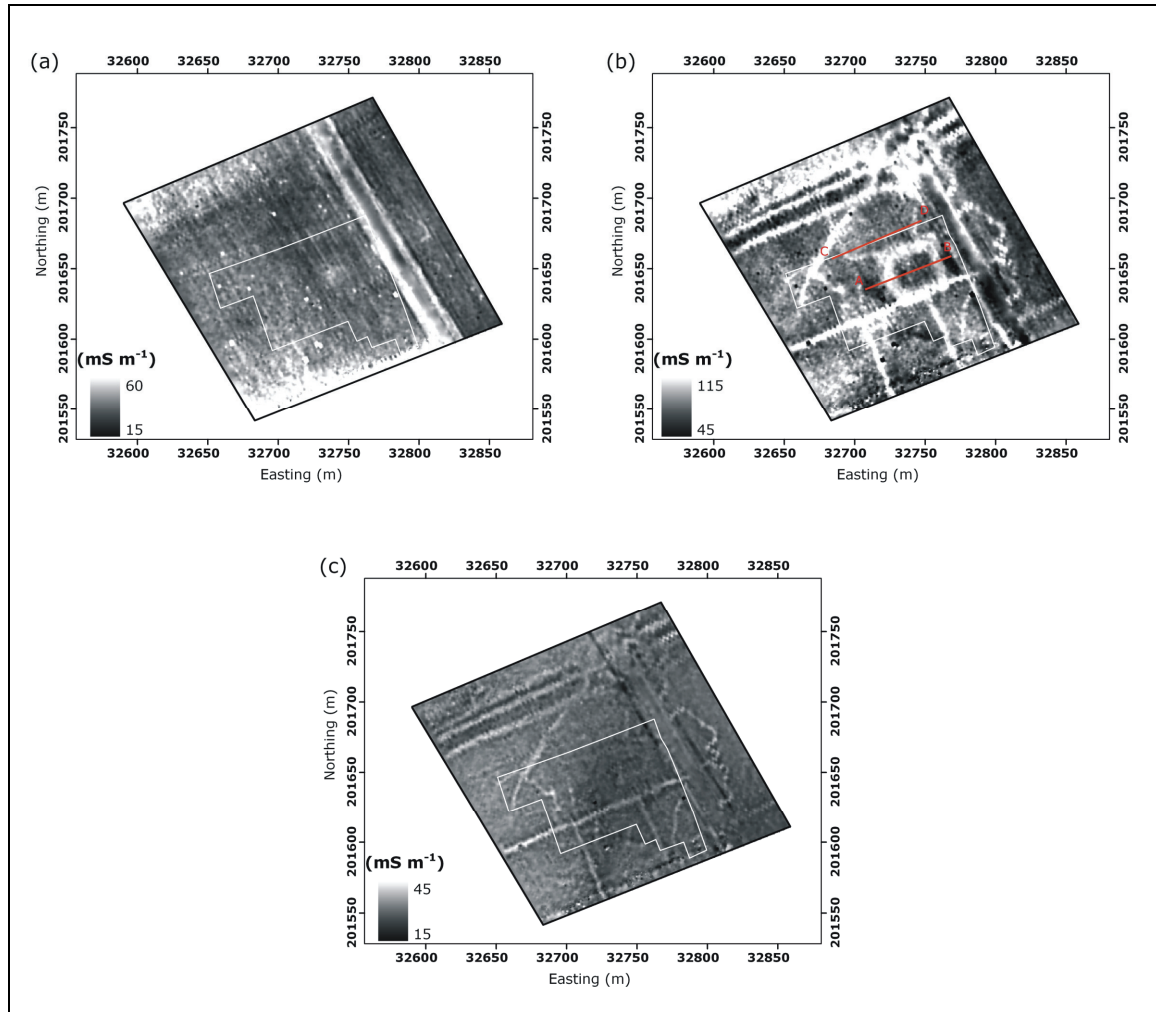


Fig. 8.4. Modelled conductivity map between 0 and 0.5 m (EC^*_1) (a), between 0.5 and 1.0 m (EC^*_2) (b) and deeper than 1.0 m (EC^*_3).

8.7 Validation

To complement the sensor measurements with field verifications we positioned two transects AB and CD through both farmstead moat and farmyard ditches (Fig. 8.4b). The E_{Ca} and EC^*_2 values along these transects were given in Fig. 8.5. When comparing the modelled EC^*_2 with the E_{Ca} measurements along both transects, EC^*_2 was characterized by more variability. To obtain a relative measure of the variability, we calculated the coefficient of variation (CV), defined as ratio between the standard deviation and the mean, along transects AB and CD. Along transect AB crossing the farmstead moat, a clear distinction in CV was observed: for EC^*_2 a CV of 25% was found, while the CV of a single measurement varied between 6 and 8 %. Along transect CD, the CV increases only slightly (8%) compared to the single E_{Ca} measurements (3 – 5%), This was related to the less pronounced farmyard ditch underlying

transect CD. Still, these illustrate that the modelled EC_2^* exhibited a higher variability at archaeological features.

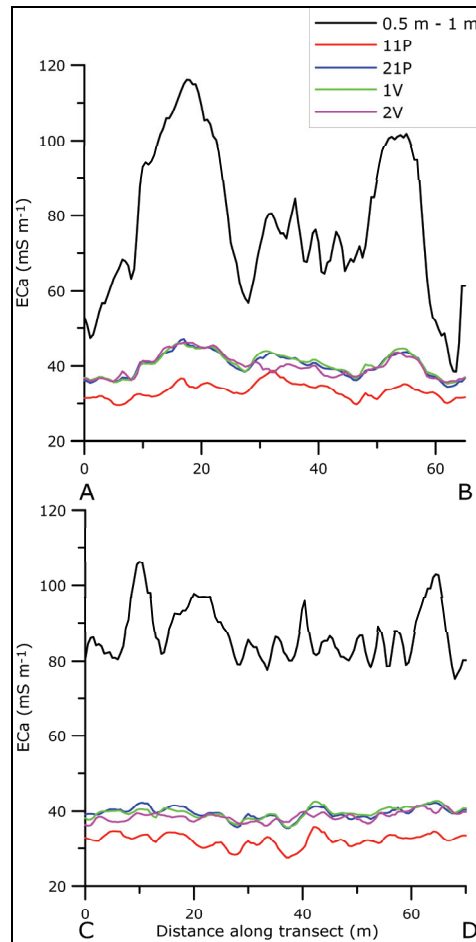


Fig. 8.5. Measured apparent electrical conductivities (ECa's) and modelled conductivity between 0.5 and 1.0 m (EC_2^*) along transects AB and CD.

Both ECa measurements and EC_2^* modelling were compared at the excavated site. Both $ECa_{p,2.1}$ (Fig. 8.2b) and $ECa_{v,1}$ (Fig. 8.2c) gave indications of the farmstead moat, ditched field boundaries and small tidal creeks, but the features became much better delineated on the EC_2^* map (Fig. 8.4b). Moreover, the farmyard ditch could be localized on the EC_2^* map. Also, its boundary continued beyond the borders of the excavation area. Both ECa's and EC_2^* were evaluated using the rasterized validation image (Fig. 8.6) from the excavated site. Zone 1 is the zone where no shallow traces were found; zone 2 bundled the distinct archaeological features. Table 8.2 lists the mean and coefficient of variation of the ECa measurements and the modelled EC_2^* stratified according to the two zones. The EC-depth modelling clearly increased the ECa variability within the zones, because the EC_2^* encountered the highest CV for both zones. The EC_2^* stratification also showed less variation in zone 2 compared to zone 1, detected as anomalies from buried archaeological features. The ECa stratification on the

other hand experienced equal or larger CV's in zone 2. Moreover, the differences in mean values between the zones were highest for EC_2^* and expressed by the relative difference (RD). For the ECa measurements, this RD was calculated as:

$$RD = \frac{X_{zone2} - X_{zone1}}{X_{zone2}} \quad [8.5]$$

with X the EC_2^* modelling or ECa measurements.

The relative difference between the zones was substantially higher for the EC_2^* modelling: the RD was 20 % for EC_2^* while the maximum RD of a single ECa measurement was 8 %. This clearly confirmed that the archaeological features are better accentuated using the EC-depth procedure.

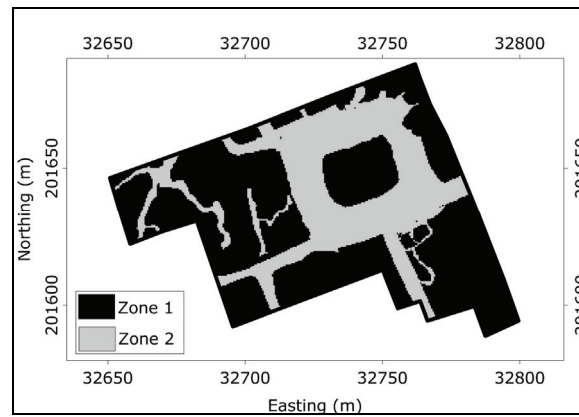


Fig. 8.6. Rasterized map of the excavated archaeological features (zone 1: features absent; zone 2: features present).

Table 8.2. Descriptive statistics (m : mean in mS m^{-1} after conversion to a reference temperature of 25°C), CV: coefficient of variation in % and RD: relative difference in %) of $\text{ECa}_{p,1,1}$, $\text{ECa}_{p,2,1}$, $\text{ECa}_{v,1}$ and $\text{ECa}_{v,2}$ measurements and modelled EC^*_2 stratified according to the two zones of the validation

Variable	image				
	Zone 1		Zone 2		RD
	m	CV	m	CV	
$\text{ECa}_{p,1,1}$	35	8	35	10	2
$\text{ECa}_{p,2,1}$	41	8	44	10	7
$\text{ECa}_{v,1}$	41	8	44	8	6
$\text{ECa}_{v,2}$	40	7	43	7	8
EC^*_2	85	22	106	20	20

8.8 Conclusions

Multiple signals of an EMI sensor are able to detect archaeological features more accurately compared to a single signal. The combination of multiple ECa measurements to a modelled EC value for a certain depth interval (EC^*) amplified small anomalies in the measurements. The relative difference between the zones was 20 % for the EC^* while the maximum relative difference of a single ECa measurement was 8 %. The resulting maps of modelled EC^* succeed in the accentuation of different types of archaeological features, even at low measurement resolution. This technique could direct the archaeological survey more efficiently and aids in the spatial recognition of continuous patterns. However, it remains necessary to combine this geophysical technique with traditional methods of field survey to obtain of a successful archaeological investigation.

Chapter 9

Combining multiple signals to prospect land for metal objects¹

9.1 Abstract

Buried unexploded ammunition is a major problem on arable land in former battle areas. Many battlefields of the First World War (WW I) still contain a lot of unexploded shells just below the plough layer, posing serious threats to soil editors and trenchers. Electromagnetic induction (EMI) sensors have been used for a variety of agricultural and archaeological purposes to map the natural soil variability and to locate buried archaeological remains. Besides its sensitivity to variations in soil texture and anthropogenic disturbances, EMI proves to respond strongly on metal objects in the soil. Most EMI sensors rely on a single signal, with magnitude and sign of the metal anomalies differing according to the instruments coil distance and separation. The multi-coil EMI sensor, the DUALEM-21S, provides four simultaneous apparent electrical conductivity (ECa) signals enhancing significantly the possibilities for signal processing. To calibrate our instrument, we buried different masses of metal at different depths. The four ECa measurements showed a response to the metal objects down to 1.2 m. The measurements were subtracted with their gradual trend to obtain the local anomalies (ΔECa). A combination of these four ΔECa 's was used to amplify the signal response to metal, influenced by both depth and mass of the buried objects. On an intensively shelled former WW I battle field near Ypres (Belgium), a detailed prospection was conducted with the DUALEM-21S. Based on our multi-signal procedure, we located 40 positions, 20 where we predicted buried metal and 20 where we expected that no metal was present within 1.2 m depth. There were no false negative predictions and at the 20 location where we expected metal, shells up to 90 kg were excavated. As a final outcome we produced a map with predictions of the mass of metal objects in the soil assuming a fixed depth, and alternatively a map with predictions of the depth of metal objects assuming a given mass. Apart from their potential for agricultural and archaeological investigations, multi-ECa signals were shown to be useful for locating metal objects, like unexploded WW I shells, in the top 1.2 m of a soil.

¹Modified from: Saey, T., Van Meirvenne, M., Dewilde, M., Wyffels, F., De Smedt, P., 2011. Combining multiple signals of an electromagnetic induction sensor to prospect land for metal objects. Near Surface Geophysics, In Press (DOI: 10.3997/1873-0604.2010070).

9.2 Introduction

Electromagnetic (EMI) methods for near-surface investigations have undergone rapid improvements over the past years. A number of new applications have appeared in precision agriculture and archeological prospection. In precision agriculture, the measurement of apparent soil electrical conductivity (ECa) with EMI is a technology that has become an invaluable tool for identifying the soil physico-chemical properties influencing crop yield patterns and for establishing the spatial variation of these soil properties (Corwin and Lesch, 2005). In archaeology, geophysical prospecting appears as a means to obtain a broader description of the archaeological landscape and as a means for extremely detailed intra-site measurements (Neubauer et al., 2002). Indeed, all the buried structures that are potentially detectable will be detected, whatever their nature and age (Bossuet et al., 2001). Despite the fact that EMI is less frequently used in archaeology, measurements of the apparent magnetic susceptibility (MSa) with EMI exhibit similar anomalies due to magnetic susceptible materials as gradiometers (Simpson et al., 2009a). The great advantage of using EMI is the low cost of sampling data at sufficient intensities to provide accurate mapped information. It is a rapid, non-invasive method for collecting soil ECa and MSa information (Saey et al., 2009b). Moreover, EMI proves useful for the detection and location of buried metal objects (Casey and Baertlein, 1999).

During the First World War (WW I), fought between August 1914 and November 1918, an estimated 1.45 billion shells were fired by the combined German, French and British armies on all fronts (Prentiss, 1937). In the war zone around Ypres, the exact number of shells fired during WW I remains unrecorded, but it must have been several tens of millions (Van Meirvenne et al., 2008). Karg (2005) estimated that about 10-15 % of them remained unexploded. Although this former front zone has continuously been cleaned-up since 1919, unexploded WW I ammunition is still found frequently during soil tillage and archaeological excavations because deeper objects move to the surface or because farmers plough deeper (Masters and Stichelbaut, 2009). Consequently, it is important to detect metal below the plough layer. The Belgian army maintains a permanent unit available to collect and dismantle former WW I shells. About 250 ton of such material is being processed annually.

Although the use of magnetometry permits detection of ferrous metallic objects at the greatest depths, the real problem is generally not the detection at great depths, but the identification of the target itself. Generally, the number of unexploded targets can be extremely small compared to the total number of retained targets with magnetometry. Electromagnetic induction surveys have been successful in detecting subsurface ferrous and non-ferrous

metallic objects, and these surveys are a mainstay amongst technologies currently utilized in unexploded ordnance (UXO) clearance projects. Mostly, time-domain electromagnetic instruments are used for UXO detection. They are able to measure at different times, hereby characterizing the metallic object (Pasion, 1999). Recently, multi-array frequency-domain EMI systems have been applied for detecting unexploded shells. Huang et al. (2007) described a new broadband EMI array system with a single transmitter and seven pairs of receivers to delineate unexploded ordnance (UXO). Less research has been done to exploit the possibilities of the DUALEM EMI soil sensors for metal detection and characterization. Generally, these sensors were used for the time-effective prospection of large areas for agricultural (Abdu et al., 2007), geomorphological (Saey et al., 2009a) and archaeological (Simpson et al., 2009a) purposes. On arable fields situated in historical battlefields, these EMI sensors could indicate the presence of buried shells supplementary to their agricultural and archaeological value.

The main objective of this study was to investigate the ability of a multi-array electromagnetic induction sensor in detecting metal objects below the plough layer. Therefore, a procedure was developed: (1) to search a combination of the multiple signals which yields a unique response of the metal objects; (2) to relate the combined signals to the depth and mass of the objects and (3) to evaluate the applicability of this procedure at a former WW I battle field.

9.3 Metal detecting

Most modern metal detectors are based on the principle of electromagnetic induction. Generally, they use separate transmit/receive circuits and operate in the very low frequency-region, typically between a few kHz and a few tens of kHz (say 1-50 kHz). An alternating charge passing through the transmitter coil generates a time-varying magnetic field, the primary field. This primary field induces surface currents on the target and eddy currents in the soil, which in turn generate a secondary magnetic field. Both the primary and the secondary field create currents through the receiver coil, from which the voltage is measured. For time domain transmission, as time elapses, the surface currents diffuse inwards the object, and the observed secondary field consequently decays. The rate of decay is determined by the target's conductivity, magnetic permeability, shape, and size. Therefore, information on the target's nature can be gathered by analyzing the decay by measuring the secondary field at different times, done with time-domain EMI instruments. Frequency-domain EMI sensors measure the secondary field at one time, frequently with various receiver coils at different distances from the transmitter coil. The combination of the four simultaneous ECa measurements of the DUALEM-21S instrument shows large potential for the identification

and characterisation of underground features (Saey et al., 2009a). The noise level of the DUALEM-21S $MSa_{p,1,1}$ and $MSa_{p,2,1}$ measurements is very high, diminishing the possibilities for combining the four simultaneous magnetic susceptibility measurements. Measurements on the calibration and validation site were taken along parallel lines with an in-between distance of respectively 0.30 m and 0.85 m.

9.4 Calibration and validation sites

Our 0.1 ha calibration site was located in Lovendegem (with central coordinates: 51°07'19"N, 3°37'05"E), in the province of East-Flanders, Belgium (Fig. 9.1). On this site, topsoil texture is loamy sand. Groups of three metal bars (chrome metal bars with length 2 m and diameter 12 mm) with a total fixed mass (m) of 11.4 kg were put in the soil at depths (z) of 0.0 m, 0.2 m, 0.4 m, 0.6 m, 0.8 m, 1.0 m and 1.2 m below surface. Additionally, metal bars were buried at a fixed z of 0.4 m but with an increasing m of 3.8 kg, 7.6 kg, 11.4 kg, 15.2 kg and 19.0 kg (Fig. 9.2). This design was created to quantify the effect of m and z on the measurements with the multi-signal EMI sensor. East of these two transects with differing depth and mass, other metal objects were buried in the soil. These were irrelevant for this research. This design was created to quantify the effect of m and z on the measurements with the multi-signal EMI sensor. We did not consider the effect of the targets shape and conductivity on the EMI measurements. On this site, DUALEM-21S measurements were performed with the instrument orientated perpendicular to the metal bars. Distance in-between the tracks or middle of the instrument was 0.3 m.

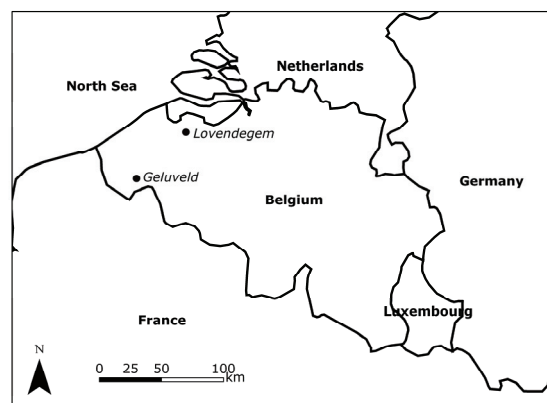


Fig. 9.1. Localization of the Lovendegem and Geluveld study sites in Belgium.

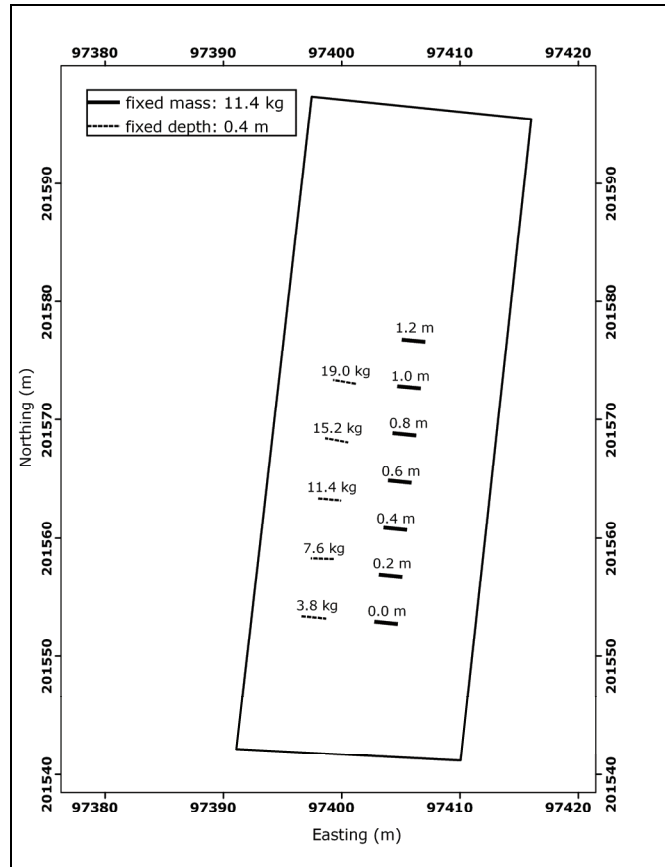


Fig. 9.2. Situation of the metal bars with different m buried at different z in the soil.

The 2.6 ha validation site was a former WW I battle field, located in Geluveld (with central coordinates: 50°50'23"N, 2°59'23"E), in the southwest of the province of West-Flanders, Belgium (Fig. 9.1). On our site, the topsoil texture consists of sandy/silty Pleistocene wind-blown sediments. The substrate directly located below the sandy loam is composed of a range of marine sandy depositions dating from the Early Eocene, with embedded clay patches. This site has been bombed intensively during WW I. It was situated on the "Geluveld plateau", southeast of Ypres. Due to the intense bombardments during WW I, a large amount of shell fragments and unexploded ammunition was expected in the subsoil of this arable field. The farmer frequently surfaces unexploded shells during tillage, confirming this hypothesis. On this site, the measurements were performed with the instrument parallel to the measurement direction. Distance in-between the tracks was 0.85 m.

9.4 ECa survey

The soil ECa of the study area was recorded with the DUALEM-21S soil sensor. Measurements on the calibration and validation site were taken along parallel lines with an in-between distance of respectively 0.30 m and 0.85 m. To remove the influence of the natural soil variability on the measurements and focus on the local anomalies in the data, a filtering procedure was followed. The extreme values were converted to the mean value of the neighboring measurement points within a circular search area with a radius of 10 m (ECa_{filtered}). Afterwards, this gradual trend was subtracted from the original ECa measurements to highlight the local anomalies (ΔECa):

$$\Delta ECa = (ECa - ECa_{\text{filtered}}) \quad [9.1]$$

At the calibration site, homogeneous ECa of 10 mS m^{-1} was subtracted from the measurements to obtain the ΔECa . The four ΔECa maps of the calibration site are given in Fig. 9.3. Each signal responded in a different way to the buried metal bars, at different z and with different m . The variation in magnitude of the response can be attributed to the z and m of the buried metal; the differences in sign of the anomalies can be assigned to the specific coil configurations.

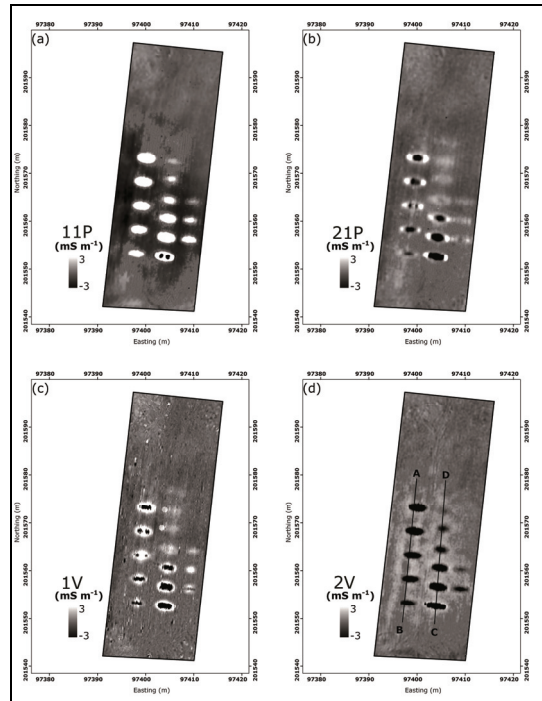


Fig. 9.3. $\Delta ECa_{p,1,1}$ with indication of m and z of the metal bars in the soil (a), $\Delta ECa_{p,2,1}$ (b), $\Delta ECa_{v,1}$ (c) and $\Delta ECa_{v,2}$ with delineation of transects AB and DC (d) at the Lovendegem calibration site (right of the 2 transects, metal bars were buried in a vertical position, not relevant for this research).

9.5 Transects

To quantify the influence of the metal bars on the measurements, we focused on the ΔECa values along two transects AB and DC (Fig. 9.3d). On transect AB, the amount of metal bars or m at a fixed z of 0.4 m varied, while along transect DC, z of a metal mass of 11.4 kg varied. Fig. 9.4 shows the ΔECa transects AB and DC, with varying m and z across the two transects. All ΔECa 's were sensitive to differences in m (transect AB) and z (transect DC) of the metal bars in the soil. $\Delta ECa_{v,1}$ was most affected by shallow objects, while $\Delta ECa_{p,1,1}$ and $\Delta ECa_{v,2}$ experienced influences up to $z = 1.0$ m. Besides, metal objects in the subsoil result in positive $\Delta ECa_{p,1,1}$ peaks, and negative $\Delta ECa_{p,2,1}$, $\Delta ECa_{v,1}$ and $\Delta ECa_{v,2}$ peaks. To improve the contrast between the metal objects and the non-metallic background, the four ΔECa 's were optimally combined to “fused electromagnetic metal prediction (FEMP)”:

$$FEMP = a \cdot \Delta ECa_{p,1,1} - b \cdot \Delta ECa_{p,2,1} - c \cdot \Delta ECa_{v,1} - d \cdot \Delta ECa_{v,2} \quad [9.2]$$

with a , b , c and d the weighting coefficients.

The sign of the weighing coefficients can be justified by the positive $\Delta ECa_{p,1,1}$ and negative $\Delta ECa_{p,2,1}$, $\Delta ECa_{v,1}$ and $\Delta ECa_{v,2}$ peaks above the metal bars. The weighting coefficients a , b , c and d were solved by equating the fused FEMP for the 11.4 kg peak at transect AB ($z = 0.4$ m) to the 0.4 m peak at transect DC ($m = 11.4$ kg) besides fixing them to a value of 100 mS m^{-1} ; by equating FEMP to 0 mS m^{-1} for metal at 1.2 m depth because the metal anomalies are 0 at this depth; and by fixing coefficient b to 1 as a starting condition. Finally, the following combination was found:

$$FEMP = 2.05 \cdot \Delta ECa_{p,1,1} - 1 \cdot \Delta ECa_{p,2,1} - 0.82 \cdot \Delta ECa_{v,1} - 1.89 \cdot \Delta ECa_{v,2} \quad [9.3]$$

Both $\Delta ECa_{p,1,1}$ and $\Delta ECa_{v,2}$ receive the greatest weight in the FEMP while $\Delta ECa_{v,1}$ receives the smallest weight. As such, the values of the solved weighting coefficients correspond well to the peaks in the ΔECa (Fig. 9.4). The higher the m of the objects on transect AB, the higher the FEMP. The closer the objects are to the surface on transect CD, the higher the FEMP. Finally, the combination gives positive unique anomalies for metal objects down to 1.0 m (Fig. 9.5). Metal is expected to be present at positive FEMP peaks. Negative FEMP values predict the absence of metal objects in the soil profile.

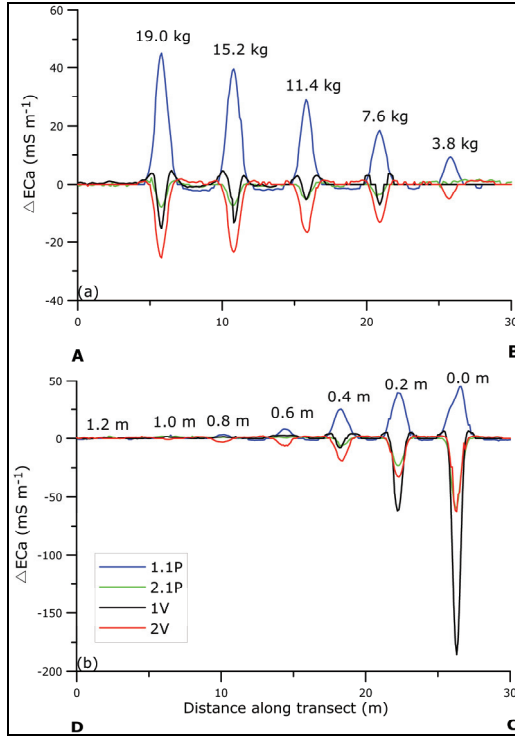


Fig. 9.4. ΔECa values along transect AB (a) and along transect DC (b).

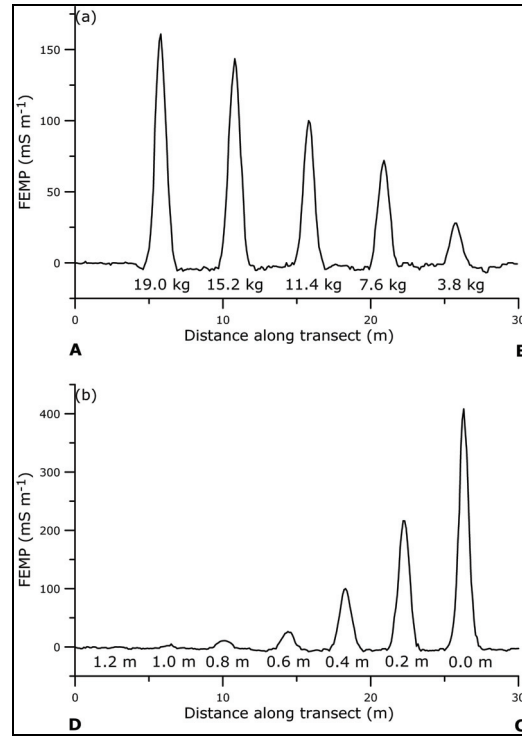


Fig. 9.5. FEMP values along transect AB (a) and along transect DC (b).

The value of the FEMP at the centre of each group of metal bars was related to m and z of the metal bars. A linear relationship was found between the FEMP peak values and m (Fig. 9.6a):

$$m = 0.108 \cdot \text{FEMP} + 0.651 \quad [9.4]$$

with an R^2 of 0.98 ($n = 5$).

A log-linear relationship was found between the FEMP peak values and z (Fig. 9.6b):

$$z = -0.213 \cdot \ln(\text{FEMP}) + 1.324 \quad [9.5]$$

with an R^2 of 0.99 ($n = 5$).

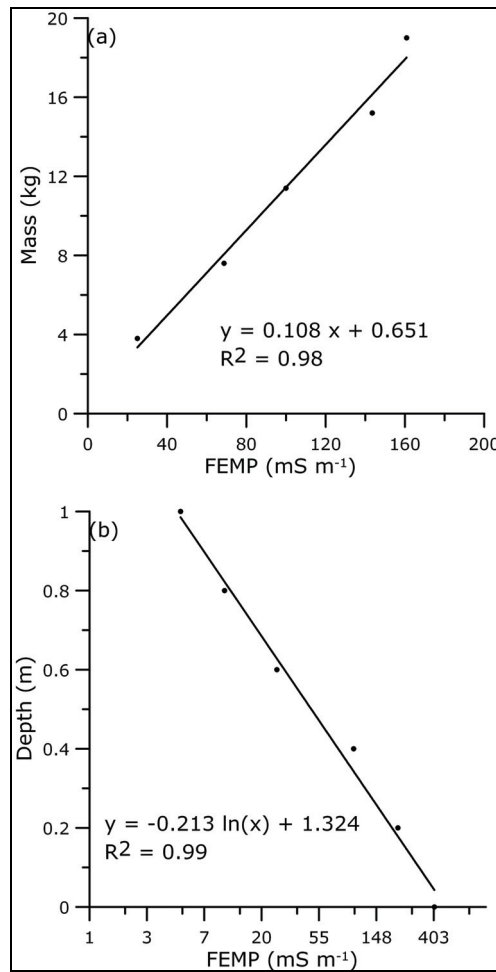


Fig. 9.6. m as a function of the FEMP of the metal bars along transect AB (a) and z as a function of $\ln(\text{FEMP})$ along transect DC (b).

9.7 Validation

On the Geluveld study site, metal objects were dug out in layers of 0.2 m in an area of 0.8 m by 0.8 m at 40 selected locations. For each successive layer, the encountered metal pieces were collected and weighted. This provided an assessment of the z and m of the metal objects at the visited locations.

Fig. 9.7 gives the ECa measurements with the DUALEM-21S at the Geluveld study site, ranging between 10 and 40 mS m⁻¹. The ECa values increase with increasing DOE (from Fig. 9.7(a) to (d)) for the specific coil configurations, so the larger the measured soil volume, the higher the conductivity, indicating a high conductive layer to be present in the deeper soil. The speckles onto the measurements are probably all due to bomb wefts with remaining shrapnel and unexploded ammunition. To obtain unique values of the metal anomalies, the

four Δ Ea maps were combined to the FEMP, shown on Fig. 9.8. Many speckles of high FEMP were observed at the site. So a lot of buried metal objects can be expected.

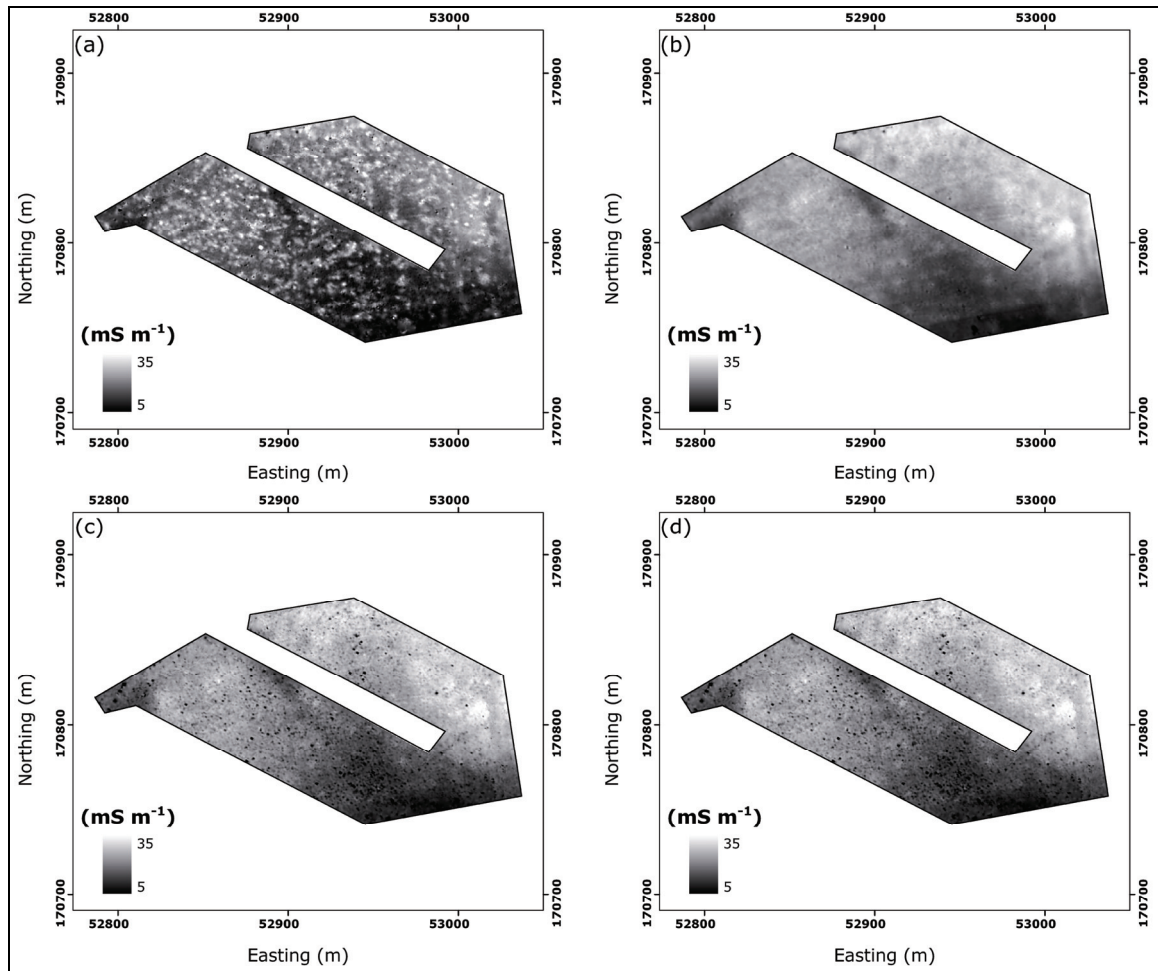


Fig. 9.7. $\text{ECa}_{p,1,1}$ (a), $\text{ECa}_{p,2,1}$ (b), $\text{ECa}_{v,1}$ (c) and $\text{ECa}_{v,2}$ (d) measurements with the DUALEM-21S instrument at the Geluvelde study site.

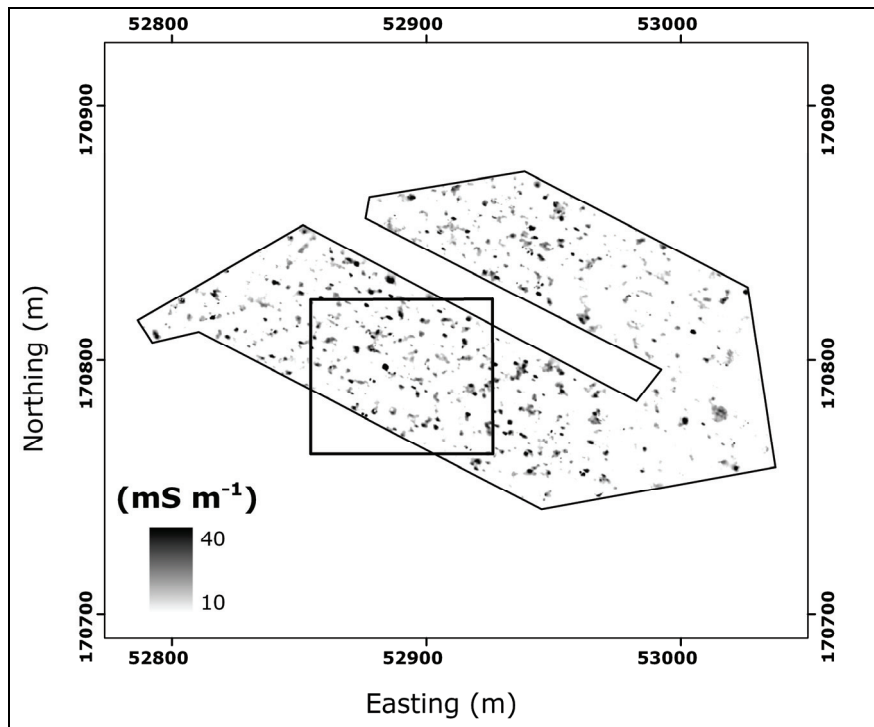


Fig. 9.8. FEMP map at the Geluvelde study site with indication of a detail window.

To validate Eqs. (9.4) and (9.5) established at the Lovendegem study site, 40 locations were designated based on the FEMP map. From these 40 locations, 20 were predicted to be ‘metal-empty’ ($\text{FEMP} < 0$), and 20 were modelled to contain buried metal. The latter 20 locations were spread out over the range of FEMP values, from 6 mS m^{-1} to 197 mS m^{-1} .

According to the excavations, the 20 locations where no metal was predicted in the subsoil proved ‘metal-empty’. The 20 spots with predicted metal contained pieces of varying mass at different depths in their profile. The metal pieces were weighted and their z was recorded. Table 9.1 gives the inventory of dug-outs at these 20 locations. Large shell remains were found at the 10 locations with the highest FEMP values ($> 47 \text{ mS m}^{-1}$). At location 17, the low FEMP value was attributed to the large z of the 18-Pounder shell (0.8 m). Below a FEMP value of 6 mS m^{-1} , no significant metal masses were found.

Table 9.1. Inventory of the metal objects in the subsoil at the 20 locations with metal predicted in the subsoil (p1 – p20) (in bold: shell remains) with their accompanied FEMP value (m : mass).

Location	m (kg)	m (kg)	m (kg)	m (kg)	FEMP (mS m ⁻¹)	z^* (m)	m^* (kg)	Identification
	0-0.4 m	0.4-0.6 m	0.6-0.8 m	> 0.8 m		$m = 11.4$ kg	$z = 0.4$ m	
p1	90.4	1.7	-	-	197	0.20	21.9	8-inch Howitzer
p2	3.9	-	-	-	155	0.25	17.4	18-Pounder
p3	16.3	-	-	-	120	0.30	13.6	4.5-inch Howitzer
p4	15.8	-	-	-	111	0.32	12.6	4.5-inch Howitzer
p5	3.7	2.5	-	-	94	0.36	10.8	18-Pounder
p6	-	0.8	30.9	-	65	0.43	7.7	60-Pounder
p7	4.6	5.8	1.5	10.8	57	0.46	6.8	18-Pounders
p8	0.9	-	-	-	55	0.47	6.6	shrapnel
p9	4.8	0.5	2.9	-	47	0.50	5.7	18-Pounder
p10	0.4	2.0	3.4	1.5	47	0.50	5.7	shrapnel
p11	0.5	1.2	-	-	24	0.65	3.2	shrapnel
p12	-	2.5	-	-	24	0.65	3.2	shrapnel
p13	2.0	-	-	-	19	0.70	2.7	shrapnel
p14	1.8	0.4	-	-	16	0.73	2.4	shrapnel
p15	-	0.02	-	-	14	0.76	2.2	shrapnel
p16	-	1.4	-	-	14	0.76	2.2	shrapnel
p17	0.07	0.2	6.3	-	10	0.83	1.7	18-Pounder
p18	0.02	-	-	-	8	0.88	1.5	shrapnel
p19	0.08	0.2	-	-	7	0.91	1.4	shrapnel
p20	0.1	-	-	-	6	0.94	1.3	shrapnel

Given the relationships found between the FEMP values and m and z , m can be predicted assuming a fixed z , or z can be modelled assuming a fixed m . Because the relationship m - FEMP was calculated for $z = 0.4$ m, Equation (9.4) was used to model m at $z = 0.4$ m as shown for the window indicated on Fig. 9.8 (Fig. 9.9(a)). Equation (9.5) was used to transform the logarithmic FEMP map in a z map of the metal objects assuming $m = 11.4$ kg

(Fig. 9.9(b)). Table 9.1 shows the modelled z and m for the locations with metal predicted in the soil profile. At some locations (for example p3, p4 and p12), m was predicted very well, because the depth of the objects coincides with the modelling depth. At most other locations, z was less accurate, either because the depth of the objects differed from the 0.4 m, or because metal was spread at multiple depth intervals. The greater part of the metal objects, assuming $m = 11.4$ kg, was predicted to be located between 0.4 m and 0.8 m depth. However, the greater part of the objects was situated in-between the soil surface and 0.6 m depth. Therefore, the z predictions proved to be less acceptable than the m modellings.

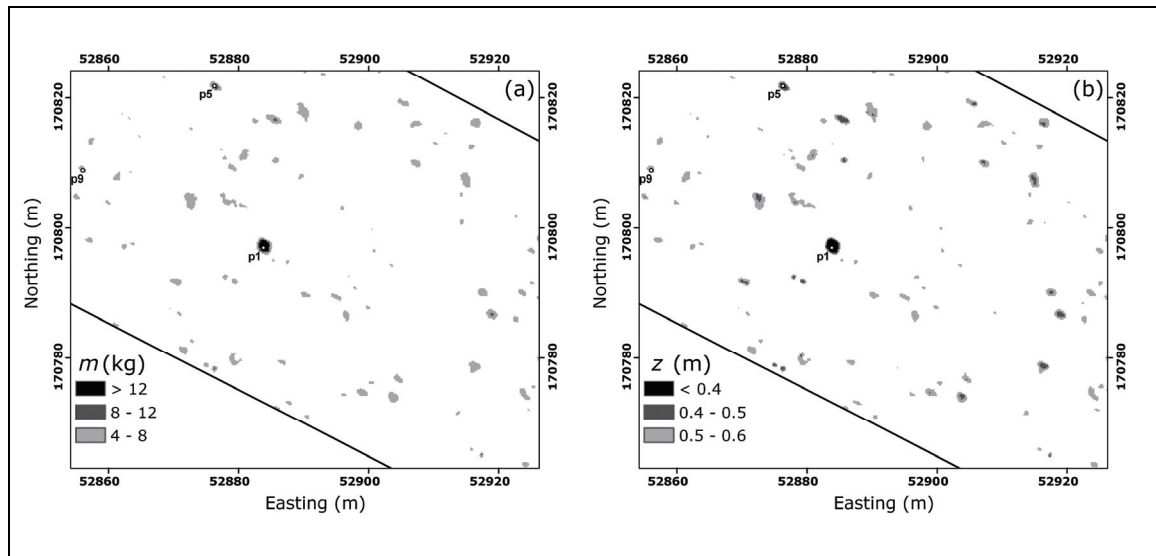


Fig. 9.9. m of the metal objects at the detail window on Fig. 9.8 assuming $z = 0.4$ m (a) and z assuming $m = 11.4$ kg (b).

9.8 Conclusions

We concluded that the following procedure proved successfully for delineating and characterizing metal objects in the subsoil:

- (1) The four ECa measurements of the DUALEM-21S were subtracted with their filtered values and the resulting ΔECa maps were combined to the $\text{FEMP} = 2.05 \cdot \Delta\text{ECa}_{p,1,1} - 1 \cdot \Delta\text{ECa}_{p,2,1} - 0.82 \cdot \Delta\text{ECa}_{v,1} - 1.89 \cdot \Delta\text{ECa}_{v,2}$ to obtain an unique signal from buried metal objects with different m and z .
- (2) A clear relationship exists between the FEMP values and m and z .
- (3) On a WW I battle field, large shell remains were encountered at locations with a FEMP value ongoing 47 mS m^{-1} . No metal could be found at locations with negative FEMP. Additionally, z predictions were made assuming a fixed m of the metal bodies and m was predicted assuming a fixed z .

This study confirmed the benefit of the combination of our multi-signal DUALEM-21S measurements in delineating buried metal objects besides their potency for agricultural and archaeological purposes. Depth and mass predictions proved more difficult, although some rough estimation could be made.

Chapter 10

General conclusions and future research

10.1 General conclusions

This research continued on the fundamentals laid down by the PhD's and papers of Vitharana (2008), Simpson (2009) and Cockx (2010). Cockx et al. (2006) showed that soil ECa data from an EMI proximal soil sensor was a valuable source of ancillary information to improve soil inventories. A wide range of soil management applications can benefit from an EMI-based soil inventory. Cockx et al. (2007) proved that the combination of the two signals of the EM38DD provides valuable information for vertical soil inventories at a field-scale. Vitharana et al. (2006) investigated in depth the application of the ECa for the inventory of the soil spatial variability in order to direct site-specific soil management. Simpson et al. (2009b) combined the multiple signals of the EMI proximal soil instruments for geoarchaeological applications. He analysed the simultaneous ECa and MSa signals together in order to characterize the physical nature of archaeological features.

The overall aim of this thesis was to investigate the integration of multiple ECa signals of two proximal soil sensors to map contrasting soil layers and to locate buried features. The general conclusions are outlined as answers on the research questions formulated in Chapter 1:

- (i) *Which soil textural fractions influence the soil electrical conductivity to identify heterogeneous soil profiles?*

Only the finest, clay fraction affects the ECa significantly.

Different soil textural fractions prove to influence the measured soil ECa. The vertical heterogeneity or interface between contrasting layers can only be detected when the conductivity of the bordering soil layers differs substantially. This conductivity mainly depends on the soil textural constitution. From the whole range of textural fractions (9 different fractions from clay to coarse sand), the clay fraction (0-2 μm) has the greatest influence on the ECa measurements. The pedotransferfunction $ECa_v = 16.2 + 1.314 \cdot Fr_{0-2,w}$ relates the ECa to the clay content for the vertical coil configuration under the restrictions of standard temperature and moisture conditions and a dominance of mica clay minerals. When the organic matter extends deeper than the upper half of the exploration depth (e.g. for the horizontal coil configuration),

both organic matter and clay content prove to be significant actors on the measured ECa.

Either heterogeneous profiles or man-induced disturbances could be identified by taking the ratio between a reference topsoil ECa as a direct conversion from the topsoil clay content (commonly soil texture maps of the topsoil exist) and the measured ECa (until a depth of approximately 1.5 m). This reference ECa is subject to uncertainties on the soil textural inventory and on the developed pedotransferfunction. If the ratio between the ECa's is near to one, the profile is quasi-homogeneous; a ratio exceeding one indicates the presence of more conductive material deeper in the soil profile, and *vice versa*.

- (ii) *Could one signal serve to model the depth between two contrasting layers accurately?*

Yes, but calibration observations are required.

Initially, the output of an EMI sensor was often a single measurement of ECa. This ECa measurement was calibrated to the depth of the interface between the contrasting layers using an empirical fit. A theoretic approach was formulated, incorporating the depth response function proposed by McNeill (1980b) as an approximation of the Maxwell's equations into the fitting process. For each coil configuration, the ECa measurements could be fitted to the depth observations to account for the modelling parameters. Finally, the relationship was able to transform the high-resolution ECa map into a three-dimensional map of the depth between the contrasting layers. The height of the interface, or the paleotopography could be visualized by subtracting this map from the current soil surface. Flowlines modelled on this surface by a flow runoff model represent past erosion processes.

- (iii) *Does combining multiple EMI measurements increase the accuracy and decrease the efforts for modelling the depth?*

No, the accuracies are similar.

Yes, the modelling efforts decrease.

Integrating the four simultaneous ECa measurements of the DUALEM-21S increases the possibilities for modelling the depth between two contrasting layers. The four different ECa measurements from each coil configuration correspond to four different depth response functions that allow depth sounding. No calibration augerings were needed for this accurate modelling, decreasing the labour efforts. The assumptions for the model were (i) a two-layered build-up of the soil profile and (ii) the theoretical depth responses from McNeill (1980b). In addition, it shows opportunities to provide inventories of the spatial variability in top- and subsoil conductivities.

- (iv) *Is it possible to develop depth response curves for the different coil configurations?*

Yes.

In soils with a very high electrical conductivity, Callegary et al. (2007) proved the depth response functions based on the Maxwell's equations deviating from the depth response functions approximated by McNeill (1980b). As an alternative, empirical depth response curves were formulated using the multiple ECa measurements and the calibration augerings. The depth response curves were fitted both for the vertical and perpendicular coil configurations whereafter the depth to the interface was modelled at each of the measurement points. Resistivity imaging provided highly accurate information of both stratigraphy and depth of the interface. Furthermore, it can be used as a tool to establish the inversion model and to validate the depth predictions. Finally, a precise inventory of the interface between two contrasting layers could be made on a landscape scale.

- (v) *Is it possible to model the depth of the interface when the upper material has a much higher conductivity than the lower layers?*

Yes.

High-conductive upper layers do not seem to attenuate the electromagnetic signal. Varying depths of tidal channel in the coastal area were accurately modelled using a multi-channel approach. The tidal channel was invisible at the surface because filled with clayey material, strongly contrasting to the subsoil which consisted of coarse sand. Even subtle variations in depth of the high-conductive top layer can easily be distinguished when the conductivity contrast between top- and subsoil layer is appreciable.

- (vi) *Can archaeological features be accentuated by fusing the multiple signals?*

Yes.

Small archaeological features are frequently masked in the ECa measurements by both the highly conductive surrounding material or by large disturbances in the neighbourhood. A procedure was proposed to highlight subtle anomalies masked by these confounders. Layer conductivities (within discrete depths) were modelled by combining the multiple ECa signals because these measurements commonly show analogue patterns in their ECa signals. By integrating these signals, the visualization of vague anomalies could be enhanced. Subtle archaeological traces not visible in the single ECa measurements or present below highly contrasting topsoil can easily be amplified. This could aid in recognizing the continuity of a variety of human-induced features with the final aim to direct archaeological excavations more efficiently.

- (vii) *Does the multi-signal approach improve metal delineation and estimation of mass and depth?*

Yes for the metal delineation.

No for the combined estimation of mass and depth.

Single ECa signals seem invaluable for delineating metal objects and modelling their characteristics, because either they are only sensitive for very shallow metal objects or their responses above metal objects at different depths or with different mass are similar. By filtering the natural soil variability and combining the multiple ECa signals to $FEMP = 2.05 \cdot \Delta ECa_{p,1,1} - 1 \cdot \Delta ECa_{p,2,1} - 0.82 \cdot \Delta ECa_{v,1} - 1.89 \cdot \Delta ECa_{v,2}$, accurate delineations of the anomalies caused by metal objects within the top 1.2 m of the soil could be made. This combined FEMP increases the contrast between the anomalies from the buried metal and the background substantially. An extra dimension was given to the ECa signals: not only the natural soil variability (ECa) and archaeological features (ECa and MSA) can be estimated, but anomalies caused by metal objects (for example unexploded shells and bombs) can be identified and situated. The suspicious locations should safely be approached before it is possible to release the terrain. Mass or depth predictions proved to be less accurate.

This thesis proved that multi-signal processing enhances and facilitates the interpretation of the obtained information. Heterogeneous soil profiles can be identified by comparing signals of the multiple coil configurations, each with their particular depth response function. From approximations of these depth response functions, the ECa measurements can be calibrated to the depth of the interface between the two contrasting soil layers. Depth sounding by the four simultaneous measurements of the DUALEM-21S instrument substantially decreases the labouring efforts. In highly conductive soils, the depth response approximations do not hold. Therefore, depth response functions can be modelled for each particular coil configuration. These depth response functions prove to work both for low-conductive material above highly conductive subsoil as for high-conductive material above low-conductive subsoil.

The signatures of different underground features can be strongly amplified by integrating the multiple signals. Combining the multiple signals can also highlight slightly contrasting anomalies invisible in single measurements. The influence of dominant natural or antropogenic disturbances can be reduced by combining the ECa measurements, emphasizing 'invisible' features.

Moreover, multi-signal processing enhances the possibilities for metal delineation. A clear distinction can be made between the anomalies caused by buried metal and the 'metal-empty' background.

To conclude, the strength of the multi-coil EMI instruments exists in the integrated evaluation of the different signals in order to get a clear picture and a uniform understanding about various underground phenomena. Nevertheless, experience about the instrument signals and the physical nature of the prospected soil and possible underground features remains crucial.

10.2 Future research

Every proximal soil-sensor technology has strengths and weaknesses, and no single sensor can map all soil properties and buried features. It is therefore important to select a set of sensors that complement each other. Integrating multiple proximal sensors in a single multi-sensor platform can provide a number of benefits over single-sensor systems: robust operational performance, increased confidence, extended attribute coverage and increased dimensionality of the measurement space. (Viscarra-Rossel et al., 2010).

Future research should therefore focus on both the combination of the multiple, simultaneous signals of advanced instruments and on the integration of multiple sensors in one measurement configuration.

Therefore, research should be conducted about the integration of the multiple MSa measurements with the ECa measurements to obtain complementary information from different soil volumes and a greater understanding about the physical nature of the prospected material. Regrettably, the noise level of the magnetic measurements from the DUALEM-21S perpendicular coil configurations of the DUALEM-21S instrument appears to be too high, diminishing the possibilities for multi-signal processing.

Extending this research could involve the intergration of the multiple EMI signals with additional information from proximal soil sensors based on another geophysical principle. Combining EMI with GPR could entail knowledge about the permittivity apart from the conductivity and susceptibility. Estimations about the soil water content are directly related to the dielectric permittivity. GPR could provide a very precise depth approximation about the interfaces between different underground features, but the threatment of the large amount of data and the interpretation requires much effort. Therefore, the soil constitution should be estimated from a limited number of GPR profiles before the surface-covered EMI measurements can be ‘fine tuned’ to the depth between contrasting soil layers. Other applications situate in the quantification of the vertical extent of added layers with GPR, before highlighting subtle anomalies below these recent layers with EMI. This application could also release layers added after WW II, when no shells or bombs are assumed to be present in this top layer. Anomalies resulting from metal objects seen in the $\Delta ECa_{v,1}$ – signal (very sensitive for shallow metal) could be compared with the anomalies in the FEMP signal,

this to exclude anomalies from buried metal in the top layer (anomalies in both $\Delta E_{Ca_{v,1}}$ and FEMP are excluded) with the aim to decrease the costs of approaching the suspected anomalies.

Due to the fact that GPR measures reflections at boundaries with different dielectric constants, the nature of the features can only be deduced from the EMI signals. The speed with which the high-frequency electromagnetic waves penetrate in the soil is linearly related to the conductivity of the soil. Accurate depth estimations with GPR require an accurate value of this penetration speed. Therefore, conductivity measurements with EMI could be used as a proxy to determine the penetration speed of the high-frequent electromagnetic waves in the soil and improve the accuracy of the depth estimation with GPR. On high-conductive (clayey) soils and soils with a shallow groundwater table, EMI can be the only solution for prospecting the underground, because high-conductive layers and a saturated soil attenuate the high-frequent GPR signal.

Another future research direction could combine multi-signal EMI with magnetometry. EMI could be used to identify zones of archaeological interest based on the complementary conductivity (paleo-landscape) and magnetic susceptibility (anthropogenic disturbance) information. High-resolution magnetometry could be used on the selected areas to detect subtle archaeological disturbances by recording slight changes in the Earth's magnetic field. Magnetic susceptibility and magnetometry exhibit similar patterns, but although magnetometry is more sensitive, interpretation is not easy due to the 'dipole' character of the anomalies. MSA anomalies can create a clear picture of underground phenomena. Therefore, both techniques are able to complement each other.

For metal prospecting, magnetometry proves to be more effective than EMI because of its higher sensitivity for ferrous metallic objects. However, EMI gives indications of both ferrous and non-ferrous objects. The depth of investigation for metal objects (1.2 m) is less than for magnetometry (± 3 m) for bombs, but EMI is less sensitive to metal disturbances in the surrounding.

To conclude, the future direction for archaeological, pedological and quaternary-geomorphological investigation involves the simultaneous employment of multiple multi-signal sensors to enhance the understanding of the subsoil features. Depending on the required objective and resolution, different systems need to be designed, software developed and people educated to interpret the collected geophysical data. Nevertheless, it is crucial to assess the value of the extra information from the application of multiple sensors in economic terms against the additional costs associated with data collection and the more complicated data processing and fusion.

References

- Abdu, H., Robinson, D.A., Jones, B., 2007. Comparing bulk soil electrical conductivity determination using the DUALEM-1S and EM38-DD electromagnetic induction instruments. *Soil Science Society America Journal*, 71: 189-196.
- Adamchuk, V.I., Hummel, J.W., Morgan, M.T., Upadhyaya, S.K., 2004. On-the-go soil sensors for precision agriculture. *Computers and Electronics in Agriculture*, 44: 71-91.
- Ameryckx, J.B., Verheye, W., Vermeire, R., 1995. *Bodemkunde: bodemvorming, bodemeigenschappen, de bodems van België, bodembehoud en –degradatie, bodembeleid en bodempolitiek*.
- Amezketta, E., 2006. An integrated methodology for assessing soil salinization, a pre-condition for land-desertification. *Journal of Arid Environments*, 67: 594-606.
- Amezketta, E., 2007. Use of an electromagnetic technique to determine sodicity in saline-sodic soils. *Soil Use Management*, 23: 278-285.
- Baeteman, C., 1991. Chronology of coastal plain development during the Holocene in West Belgium. *Quaternaire*, 2: 116-125.
- Baeteman, C., 1999. The Holocene depositional history of the IJzer palaeovalley (Western Belgian coastal plain) with reference to the factors controlling the formation of intercalated peat beds. *Geologica Belgica*, 2: 39-72.
- Baeteman, C., 2008. Radiocarbon-dated sediment sequences from the Belgian coastal plain: testing the hypothesis of fluctuating or smooth late-Holocene relative sea-level rise. *The Holocene*, 18: 1219-1228.
- Baeteman, C., Beets, D.J., Van Strydonck, M., 1999. Tidal crevasse splays as the cause of rapid changes in the rate of aggradation in the Holocene tidal deposits of the Belgian coastal plain. *Quaternary International*, 56: 3-13.
- Baeteman, C., Declercq, P.-Y., 2002. A synthesis of early and middle Holocene coastal changes in the western Belgian lowlands. *Belgeo*, 2: 77-107.
- Batte, A., Muwanga, A., Owor, M., 2008. Vertical electrical sounding as an exploration technique to improve on the certainty of groundwater yield in the fractured crystalline basement aquifers of eastern Uganda. *Hydrogeology Journal*, 16: 1683-1693.
- Bersezio, R., Giudici, M., Mele, M., 2007. Combining sedimentological and geophysical data for high-resolution 3-D mapping of fluvial architectural elements in the Quaternary Po plain (Italy). *Sedimentary Geology*, 202: 230-248.
- Bertrand, S., Baeteman, C., 2005. Sequence mapping of Holocene coastal lowlands: the application of the Streif classification system in the Belgian coastal plain. *Quaternary International*, 133-134: 151-158.

- Bevan, B., 1983. Geophysical exploration for archaeology: An introduction to geophysical exploration. Midwest Archaeological Center Special Report 1.
- Boll, J., van Rijn, R.P.G., Weiler, K.W., Ewen, J.A., Daliparthi, J., Herbert, S.J., Steenhuis, T.S., 1996. Using ground-penetrating radar to detect layers in a sandy field soil. *Geoderma*, 70: 117-132.
- Boorman, B.J., 1990. Assessing the ability of ground penetrating radar to delineate subsurface fluvial lithofacies. Master thesis University of Calgary, Calgary, Canada.
- Bork, E.W., West, N.E., Doolittle, J.A., Boettinger, J.L., 1998. Soil depth assessment of sagebrush grazing treatments using electromagnetic induction. *Journal of Range Management*, 51: 469-474.
- Bossuet, G., Camerlynck, C., Brehonnet C., Petit, C., 2001. Magnetic prospecting of diachronic structures (antiquity to First World War) on the site of the sanctuary of Ribemont-sur-Ancre (Somme, France). *Archaeological Prospection*, 8: 67-77.
- Boucneau, G., Van Meirvenne, M., Thas, O., Hofman, G., 1998. Integrating properties of soil map delineations into ordinary kriging. *European Journal of Soil Science*, 49: 213-229.
- Brenning, A., Koszinski, S., Sommer, M., 2008. Geostatistical homogenization of soil conductivity across field boundaries. *Geoderma*, 143: 254-260.
- Brevik, E.C., Fenton, T.A., Lazari, A., 2006. Soil electrical conductivity as a function of soil water content and implications for soil mapping. *Precision Agriculture*, 7: 393-404.
- Callegary, J.B., Ferré, Ty P.A., Groom, R.W., 2007. Vertical spatial sensitivity and exploration depth of low-induction-number electromagnetic-induction instruments. *Vadose Zone Journal*, 6: 158-167.
- Carroll, Z.L., Oliver, M.A., 2005. Exploring the spatial relationships between soil physical properties and apparent electrical conductivity. *Geoderma*, 128: 354-374.
- Casey K.F., Baertlein B.A., 1999. An overview of electromagnetic methods in subsurface detection. In: C.E. Baum (Editor) *Detection and identification of visually obscured objects* (ed. C.E. Baum), Taylor & Francis, London, Great Britain, pp. 9-46.
- Cockx, L., Ghysels, G., Van Meirvenne, M., Heyse, I., 2006. Prospecting frost-wedge pseudomorphs and their polygonal network using the electromagnetic induction sensor EM38DD. *Permafrost and Periglacial Processes*, 17: 163-168.
- Cockx, L., Van Meirvenne, M., De Vos, B., 2007. Using the EM38DD soil sensor to delineate clay lenses in a sandy forest soil. *Soil Science Society of America Journal*, 71: 1314-1322.
- Cockx, L., 2010. High resolution soil inventory using a dual signal electromagnetic induction sensor. PhD thesis, Ghent University.

- Corwin, D.L., Lesch, S.M., 2003. Application of soil electrical conductivity to precision agriculture: theory, principles and guidelines. *Agronomy Journal*, 95: 455-470.
- Corwin, D.L., Lesch, S.M., 2004. Apparent soil electrical conductivity measurements in agriculture. *Computers and Electronics in Agriculture*, 46: 11-43.
- Corwin, D.L., Lesch, S.M., 2005. Characterizing soil spatial variability with apparent electrical conductivity: I. Survey protocols. *Computers and Electronics in Agriculture*, 46: 103-133.
- Cosandey, A.-C., Guenat, C., Bouzelboudjen, M., Maître, V., Bovier, R., 2003. The modelling of soil-process functional units based on three-dimensional soil horizon cartography, with an example of denitrification in a riparian zone. *Geoderma*, 112: 111-129.
- Domsch, H., Giebel, A., 2004. Estimation of soil textural features from soil electrical conductivity recorded using the EM38. *Precision Agriculture*, 5: 389-409.
- Doolittle, J.A., Sudduth, K.A., Kitchen, N.R., Indorante, S.J., 1994. Estimating depth to clays using electromagnetic induction methods. *Journal of Soil and Water Conservation*, 49: 572-575.
- Doolittle, J.A., Collins, M.E., 1998. A comparison of EM induction and GPR methods in areas of karst. *Geoderma*, 85: 83-102.
- Dualem Inc., 2007. DUALEM-21S user's manual. Dualem Inc., Milton, Canada.
- Duffera, M., White, J.G., Weisz, R., 2007. Spatial variability of Southeastern U.S. Coastal Plain soil physical properties: Implications for site-specific management. *Geoderma*, 137: 327-339.
- Ervynck, A., Baeteman, C., Demiddelde, H., Hollevoet, Y., Pieters, M., Schelvis, J., Tys, D., Van Strydonck, M., Verhaege, F., 1999. Human occupation because of a regression, or the cause of a transgression? A critical review of the interaction between geological events and human occupation in the Belgian coastal plan during the first millenium AD. *Probleme der Küstenforschung im südlichen Nordseegebiet*, 26: 97-121.
- FAO/ISRIC/ISSS. 1998. World reference base for soil resources. World soil resources report. FAO, Rome.
- Forte, E., Pipan, M., 2008. Integrated seismic tomography and ground-penetrating radar (GPR) for the high-resolution study of burial mounds (*tumuli*). *Journal of Archaeological Science*, 35: 2614-2623.
- Frischknecht, F.C., Labson, V.F., Spies, B.R., Anderson, W.L., 1991. Profiling methods using small sources. In: M.N. Nabighian (Editor), *Electromagnetic methods in applied geophysics volume 2*. Society of Exploration geophysics, United States of America, pp. 105-269.

-
- Gaffney, C., Hughes, G., Gater, J., 2005. Magnetic Susceptibility Survey at King Lobengula's Palace KoBulawayo, Zimbabwe. *Archaeological Prospection*, 12: 31-49.
- Gaffney, C., Gater, J., 2003. *Revealing the buried past: Geophysics for Archaeologists*. Tempus Publishing Ltd., Gloucestershire, Great Britain.
- Garten Jr., C.T., Kang, S., Brice, D.J., Schadt, C.W., Zhou, J., 2007. Variability in soil properties at different spatial scales (1 m – 1 km) in a deciduous forest ecosystem. *Soil Biology & Biochemistry*, 39: 2621-2627.
- Gebbers, R., Lück, E., Heil, K., 2007. Depth sounding with the EM38-detection of soil layering by inversion of apparent electrical conductivity measurements. p. 95-102. In: J.V. Stafford (Editor) *Precision Agriculture '07*. Wageningen Academic Publishers, Wageningen, The Netherlands, pp. 95-102.
- Geotomo Software, 2007. RES2DINV ver. 3.56. Rapid 2-D Resistivity & IP inversion using the least-squares method.
- Gillijns, K., Poesen, J., Deckers, J., 2005. On the characteristics and origin of closed depressions in loess-derived soils in Europe — a case study from central Belgium. *Catena*, 60: 43-58.
- Goossens, D., 1984. *Geologie en geomorfologie van België*. Enschede, Uitgeverij van de Berg.
- Goovaerts, P., 1997. *Geostatistics for Natural Resources Evaluation*, Oxford University Press, New York.
- Gustavsson, M., Kolstrup, E., Seijmonsbergen, A.C., 2006. A new symbol-and-GIS based detailed geomorphological mapping system: Renewal of a scientific discipline for understanding landscape development. *Geomorphology*, 77: 90-111.
- Henderson, B.L., Bui, E.N., Moran, C.J., Simon, D.A.P., 2005. Australia-wide predictions of soil properties using decision trees. *Geoderma*, 124: 383-398.
- Hendrickx, J.M.H., Borchers, B., Corwin, D.L., Lesch, S.M., Hilgendorf, A.C., Schlue, J., 2002. Inversion of soil conductivity profiles from electromagnetic induction measurements. *Soil Science Society of America Journal*, 66: 673-685.
- Hendrickx, J.M.H., Kachanoski, R.G., 2002. Indirect measurement of solute concentration: Nonintrusive electromagnetic induction. In: J.H. Dane and G.C. Topp (Editors), *Methods of soil analysis. Part 4. SSSA Book Ser. 5*. SSSA, Madison, WI.
- Hengl, T., Heuvelink, G.B.M., Stein, A., 2003. A generic framework for spatial prediction of soil variables based on regression-kriging. *Geoderma*, 120: 75-93.
- Hillel, D., 1998. *Environmental Soil Physics*. Academic Press, San Diego.
- Huang, H., SanFilipo, B., Oren, A., Won, I.J., 2007. Coaxial coil towed EMI sensor array for UXO detection and characterization. *Journal of Applied Geophysics*, 61: 217-226.

- Hubert, P., 1976. Verklarende tekst bij het kaartblad: Zwevegem 97E. Hoste-Staelens, Gent.
- Huth, N.I., Poulton, P.L., 2007. An electromagnetic induction method for monitoring variation in soil moisture in agroforestry systems. *Australian Journal of Soil Research*, 45: 63-72.
- Inman, D.J., Freeland, R.S., Ammons, J.T., Yoder., R.E., 2002. Soil investigations using electromagnetic induction and ground-penetrating radar in southwest Tennessee. *Soil Science Society of America Journal*, 66: 206-211.
- Iriondo, M.H., Kröhling, D.M., 2007. Non-classical types of loess. *Sedimentary Geology*, 202: 352-368.
- Jenson, S., Domingue, J., 1988. Extracting topographic structure from digital elevation data for geographic information system analysis. *Photogrammetric Engineering and Remote Sensing*, 54: 1593-1600.
- Karg, F., 2005. Consideration of toxic metabolites from explosives & chemical warfare agents on polluted military and armament sites for health risk assessments. In: O. Uhlmann, G. Annokkée and F. Arendt (Editors), *Consoil 2005 Proceedings*, Forschungszentrum Karlsruhe (distributed as .pdf files on CD), Germany, pp. 710-720.
- Kaufmann, O., Cerak, Y.Q., 2001. An application of cone penetration tests and combined array 2D electrical resistivity tomography to delineate cover-collapse sinkhole prone areas. In: B.F. Beck and J.G. Herring (Editors), *Geotechnical and environmental applications of karst geology and hydrology*. Swets & Zeitlinger Publishers, Lisse, The Netherlands, pp. 359-364.
- Kerry, R., Oliver, M., 2007. Comparing sampling needs for variograms of soil properties computed by the method of moments and residual maximum likelihood. *Geoderma*, 140: 383-396.
- Kværnø, S.H., Haugen, L.E., Børresen, T., 2007. Variability in topsoil texture and carbon content within soil map units and its implications in predicting soil water content for optimum workability. *Soil and Tillage Research*, 95: 332-347.
- Lee, B.D., Jenkinson, B.J., Doolittle, J.A., Taylor, R.S., Tuttle, J.W., 2006. Electrical conductivity of a failed septic system soil absorption field. *Vadose Zone Journal*, 5: 757-763.
- Lehouck, A., 2010. Het verdwenen landschap en de etymologie van Koksijde. Een landschaps-historische benadering op basis van plaatsnamen, In: J. De Caluwe and J. Van Keymeulen (Editors), *Artikelen voor Magda Devos bij haar afscheid van de Universiteit Gent*, Academia Press, Gent, Belgium, pp. 397-419.

- Lesch, S.M., Herrero, J., Rhoades, J.D., 1998. Monitoring for temporal changes in soil salinity using electromagnetic induction techniques. *Soil Science Society of America Journal*, 62: 232-242.
- Leverington, D.W., Teller, J.T., Mann, J.D., 2002. A GIS method for reconstruction of late Quaternary landscapes from isobase data and modern topography. *Computers and Geosciences*, 28: 631-639.
- Loke, M.H., 2001. RES1D ver. 1.0. 1-D Resistivity, IP & SIP Inversion and forward modelling.
- Loke, M.H., Acworth, I., Dahlin, T., 2003. A comparison of smooth and blocky inversion methods in 2D electrical imaging surveys. *Exploration Geophysics*, 34: 182-187.
- Lowe, J.J., Walker, M.J.C., 1997. *Reconstructing Quaternary environments*. Pearson Education Limited, Essex.
- Lück, E., Callmer, J., Skånberg, T., 2003. The house of Bailiff of Sövestad, Sweden – a multi-method geophysical case-study. *Archaeological Prospection*, 10: 143-151.
- Lunt, I.A., Bridge, J.S., Tye, R.S., 2004. A quantitative three-dimensional model of gravelly braided rivers. *Sedimentology*, 51: 377–414.
- Maréchal, R., 1992. De geologische structuur. In: J. Denis (Editor), *Geografie van België*. Gemeentekrediet, Brussel, Belgium, pp. 39-86.
- Maréchal, R., Laga, P., 1988. *Voorstel lithostratigrafische indeling van het Paleogeen*. Commissie Tertiair, Nationale Commissie voor Stratigrafie, Brussel.
- Marquardt, D., 1963. An algorithm for least-squares estimation of nonlinear parameters. *SIAM Journal of Applied Mathematics*, 11: 431-441.
- Masters, P., Stichelbaut, B., 2009. From the air to beneath the soil – revealing and mapping Great War trenches at Ploegsteert (Comines – Warneton), Belgium. *Archaeological prospection*, 16: 279-285.
- McBratney, A., Minasny, B., Whelan, B.M., 2005. Obtaining ‘useful’ high-resolution soil data from proximally-sensed electrical conductivity/resistivity (PSEC/R) surveys. In: J.V. Stafford (Editor), *Precision agriculture '05*. Wageningen Academic Publishers, Wageningen, The Netherlands, pp. 503-510.
- McCutcheon, M.C., Farahani, H.J., Stednick, J.D., Buchleiter, G.W., Green, T.R., 2006. Effect of soil water on apparent soil electrical conductivity and texture relationships in a dryland field. *Biosystems Engineering*, 94: 19-32.
- McKenzie, N.J., Grundy, M.J., Webster, R., Ringrose-Voase, A.J., 2008. *Guidelines for surveying soil and land resources*. Australian soil and land survey handbook series, CSIRO publishing, Colingwood Victoria, Australia.

-
- McNeill J.D., 1980a. Electrical conductivity of soils and rocks. Technical Note TN-5, Geonics Limited, Mississauga, ON, Canada.
- McNeill, J.D., 1980b. Electromagnetic terrain conductivity measurement at low induction numbers. Technical Note TN-6, Geonics Limited, Mississauga, ON, Canada.
- Minasny, B., McBratney, A.B., Whelan, B.M., 2005. VESPER version 1.62. Australian Centre for Precision Agriculture, McMillan Building A05, The University of Sydney, NSW 2006. (<http://www.usyd.edu.au/su/agric/acpa>)
- Moghadas, D., André, F., Vereecken, H., Lambot, S., 2010. Efficient loop antenna modelling for zero-offset, off-ground electromagnetic induction in multilayered media. *Geophysics*, 75: 125-134.
- Moorman, B.J., 1990. Assessing the ability of ground penetrating radar to delineate subsurface fluvial lithofacies, MSc. Thesis, The University of Calgary.
- Moran, M.S., Inoue, Y., Barnes, E.M., 1997. Opportunities and limitations for image-based remote sensing in precision crop management. *Remote Sensing of Environment*, 61:319-346.
- Monteiro Santos, F.A., Triantafyllis, J., Bruzgulis, K.E., Roe, J.A.E., 2010. Inversion of DUALEM-421 profiling data using a 1-D laterally constrained algorithm. *Vadose Zone Journal*, 9: 117-125.
- Morris, E.R., 2009. Height-above-ground effects on penetration depth and response of electromagnetic induction soil conductivity meters. *Computers and Electronics in Agriculture*, 68: 150-156.
- Myers, D.B., Kitchen, N.R., Sudduth, K.A., Grunwald, S., Miles, R.J., Sadler, E.J., Udawatta, R.P., 2010. Combining proximal and penetrating soil electrical conductivity sensors for high-resolution digital soil mapping. In: R. Viscara-Rossel and A. McBratney (Editors), *Proximal Soil Sensing for High Resolution Soil Mapping*, Chapter 19, 10 p.
- Nemes, A., Wösten, J.H.M., Lilly, A., Oude Voshaar, J.H., 1999. Evaluation of different procedures to interpolate particle-size distributions to achieve compatibility within soil databases. *Geoderma*, 90: 187-202.
- Neubauer, W., Eder-Hinterleitner, A., Seren, S., Melichar, P., 2002. Georadar in the Roman civil town Carnuntum, Austria: an approach for archaeological interpretation of GPR data. *Archaeological Prospection*, 9: 135-156.
- Pasion, L.R., 1999. Detecting unexploded ordnance with time domain electromagnetic induction. Master thesis, The University of British Columbia, Vancouver, Canada.
- Pasion, L.R., Oldenburg, D.W., 2001. A discrimination algorithm for UXO using time domain electromagnetics. *Journal of Environmental & Engineering Geophysics*, 6: 91-102.

- Pellerin, L., Wannamaker, P.E., 2005. Multi-dimensional electromagnetic modelling and inversion with application to near-surface earth investigations. *Computers and Electronics in Agriculture*, 46: 71-102.
- Persson, K., Olofsson, B., 2004. Inside a mound: Applied geophysics in archaeological prospecting at the Kings' Mounds, Gamla Uppsala, Sweden. *Journal of Archaeological Science*, 31: 551-562.
- Prentiss, A.M., 1937. *Chemicals in War: A Treatise on Chemical Warfare*. McGraw-Hill, New York.
- Reynolds, J.M., 1997. *An introduction to applied and environmental geophysics*. John Wiley & Sons Ltd., Chichester, England.
- Rhoades, J.D., Van Schilfgaarde, J., 1976. An electrical conductivity probe for determining soil salinity. *Soil Science Society of America Journal*, 40: 647-651.
- Rhoades, J.D., Manteghi, N.A., Shouse, P.J., Alves, W.J., 1989. Soil electrical conductivity and soil salinity: new formulations and calibrations. *Soil Science Society of America Journal*, 53: 433-439.
- Richards, L.A., 1954. *Diagnosis and Improvement of saline and alkali soils*. Agricultural Handbook no. 60, USDA.
- Robinson, D.A., Lebron, I., Lesch, S.M., Shouse, P., 2004. Minimizing Drift in Electrical Conductivity Measurements in High Temperature Environments using the EM-38. *Soil Science Society of America Journal*, 71: 189 - 196.
- Rodrigues, S.I., Porsani, J.L., Santos, V.R.N., DeBlasis, P.A.D., Giannini, P.C.F., 2009. GPR and inductive surveys applied in three coastal sambaqui (shell mounds) archaeological sites in Santa Catarina state, South Brazil. *Journal of Archaeological Science*, 36: 2081-2088.
- Saey, T., Simpson, D., Vitharana, U., Vermeersch, H., Vermang, J., Van Meirvenne, M., 2008. Reconstructing the paleotopography beneath the loess cover with the aid of an electromagnetic induction sensor. *Catena*, 74: 58-64.
- Saey, T., Simpson, D., Vermeersch, H., Cockx, L., Van Meirvenne, M., 2009a. Comparing the EM38DD and DUALEM-21S Sensors for Depth-to-Clay Mapping. *Soil Science Society of America Journal*, 73: 7-12.
- Saey, T., Van Meirvenne, M., Vermeersch, H., Ameloot, N., Cockx, L., 2009b. A pedotransfer function to evaluate the soil profile textural heterogeneity using proximally sensed apparent electrical conductivity. *Geoderma*, 150: 389-395.
- Samouëlian, A., Cousin, I., Tabbagh, A., Bruand, A., Richard, G., 2005. Electrical resistivity survey in soil science: a review. *Soil and Tillage Research*, 83: 173-193.

- Sass, O., 2007. Bedrock detection and talus thickness assessment in the European Alps using geophysical methods. *Journal of Applied Geophysics*, 62: 254-269.
- Schollenberger, C.J., Simon, R.H., 1945. Determination of exchange capacity and exchangeable bases in soils – ammoniumacetate method. *Soil Science*, 59: 13-24.
- Sheets, K.R., Hendrickx, J.M.H., 1995. Non-invasive soil water content measurement using electromagnetic induction. *Water Resources Research*, 31: 2401-2409.
- Simpson, D., Lehouck, A., Van Meirvenne, M., Bourgeois, J., Thoen, E., Vervloet, J., 2008. Geoarchaeological prospection of a medieval manor in the dutch polders using an electromagnetic induction sensor in combination with soil augerings. *Geoarchaeology*, 23: 305-319.
- Simpson, D., 2009. Geoarchaeological prospection with multi-coil electromagnetic induction sensors. PhD thesis, Ghent University.
- Simpson, D., Lehouck, A., Verdonck, L., Vermeersch, H., Van Meirvenne, M., Bourgeois, J., Thoen, E., Docter, R., 2009a. Comparison between electromagnetic induction and fluxgate gradiometer measurements on the buried remains of a 17th century castle. *Journal of Applied Geophysics*, 68: 294-300.
- Simpson, D., Van Meirvenne, M., Saey, T., Vermeersch, H., Bourgeois, J., Lehouck, A., Cockx, L., Vitharana, U.W.A., 2009b. Evaluating the multiple coil configurations of the EM38DD and DUALEM-21S sensors to detect archaeological anomalies. *Archaeological Prospection*, 16: 91-102.
- Sinegani, A.A.S., Mahboobi, A.A., Nazarizadeh, F., 2005. The effect of agricultural practices on the spatial variability of arbuscular mycorrhiza spores. *Turkish Journal of Biology*, 29: 149-153.
- Slavich, P.G., Petterson, G.H., 1990. Estimating average rootzone salinity for electromagnetic (EM-38) measurements. *Australian Journal of Soil Research*, 28: 453-463.
- Sloan, S.D., Tsoflias, G.P., Steeples, D.W., Vincent, P.D., 2007. High-resolution ultra-shallow subsurface imaging by integrating near-surface seismic reflection and ground-penetrating radar data in the depth domain. *Journal of Applied Geophysics*, 62: 281-286.
- Smirnoff, A., Paradis, S.J., Boivin, R., 2008. Generalizing surficial geological maps for scale change: ArcGis tools vs. cellular automata model. *Computers and Geosciences*, 34: 1550-1568.
- Smith, M.J., Rose, J., Booth, S., 2006. Geomorphological mapping of glacial landforms from remotely sensed data: An evaluation of the principal data sources and an assessment of their quality, *Geomorphology*, 76: 148-165.

-
- Spies, B.R., Frischknecht, F.C., 1991. Electromagnetic Sounding. In: M.N. Nabighian (Editor), *Electromagnetic methods in applied geophysics (volume 2, application, parts A and B)*. Society of Exploration Geophysicists, USA, pp. 285-426.
- Stroh, J.C., Archer, S., Doolittle, J.A., Wilding, L., 2001. Detection of edaphic discontinuities with ground-penetrating radar and electromagnetic induction. *Landscape ecology*, 16: 377-390.
- Sudduth, K.A., Kitchen, N.R., Bollero, G.A., Bullock, D.G., Wiebold, W.J., 2003. Comparison of electromagnetic induction and direct sensing of soil electrical conductivity. *Agronomy Journal*, 95: 472-482.
- Sudduth, K.A., Kitchen, N.R., Wiebold, W.J., Batchelor, W.D., Bollero, G.A., Bullock, D.G., Clay, D.E., Palm, H.L., Pierce, F.J., Schuler, R.T., Thelen, K.D., 2005. Relating apparent electrical conductivity to soil properties across the north-central USA. *Computers and Electronics in Agriculture*, 46: 263-283.
- Triantafilis, J., Laslett, G.M., McBratney, A.B., 2000. Calibrating an electromagnetic induction instrument to measure salinity in soil under irrigated cotton. *Soil Science Society of America Journal*, 66: 1009–1017.
- Triantafilis, J., Huckel, I.A., Odeh, I.O.A., 2003. Field-scale assessment of deep drainage risk. *Irrigation Science*, 21: 183-192.
- Triantafilis, J., Lesch, S.M., 2005. Mapping clay content variation using electromagnetic induction techniques. *Computers and Electronics in Agriculture*, 46: 203-237.
- Tromp-van Meerveld, H.J., McDonnell, J.J., 2009. Assessment of multi-frequency electromagnetic induction for determining soil moisture patterns at the hillslope scale. *Journal of Hydrology*, 368: 56-67.
- Van Meirvenne, M., Van Cleemput, I., 2005. Pedometrical techniques for soil texture mapping at a regional scale. In: S. Grunwald (Ed.), *Environmental Soil-Landscape Modelling. Geographical Technologies and Pedometrics*. CRC Press, Taylor and Francis Group, Boca Raton, FL, USA, pp. 323-341.
- Van Meirvenne, M., Meklit, T., Verstraete, S., De Boever, M., Tack, F., 2008. Could shelling in the first World War have increased copper concentrations in the soil around Ypres? *European Journal of Soil Science*, 59: 372-379.
- Vanwalleghem, T., Poesen, J., Nachtergaele, J., Verstraeten, G., 2005. Characteristics, controlling factors and importance of deep gullies under cropland on loess-derived soils. *Geomorphology*, 69: 76-91.
- Venter, M.L., Thompson, V.D., Reynolds, M.D., Waggoner Jr., J.C., 2006. Integrating shallow geophysical survey: archaeological investigations at Totógal in the Sierra de los Tuxtlas, Veracruz, México. *Journal of Archaeological Science*, 33: 767-777.

- Viscarra-Rossel, R.A., McBratney, A., Minasny, B., 2010. Proximal soil sensing. Springer, New York, USA.
- Vitharana, U.W.A., 2008. Spatial inventory techniques in support of site-specific soil management. PhD thesis, Ghent University.
- Vitharana, U.W.A., Saey, T., Cockx, L., Simpson, D., Vermeersch, H., Van Meirvenne, M., 2008a. Upgrading a 1/20,000 soil map with an apparent electrical conductivity survey. *Geoderma*, 148: 107-112.
- Vitharana, U.W.A., Van Meirvenne, M., Cockx, L., Bourgeois, J., 2006. Identifying potential management zones in a layered soil using multiple sources of ancillary information. *Soil Use and Management*, 22: 405-413.
- Vitharana, U.W.A., Van Meirvenne, M., Simpson, D., Cockx, L., De Baerdemaeker, J., 2008b. Key soil and topographic properties to delineate potential management classes for precision agriculture in the European loess area. *Geoderma*, 143: 206-215.
- Wait, J.R., 1962. A note on the electromagnetic response of a stratified earth. *Geophysics*, 27: 382-385.
- Walvoort, D.J.J., De Gruijter, J.J., 2001. Compositional kriging: a spatial interpolation method for compositional data. *Mathematical Geology*, 33: 951-966.
- Webster, R., Oliver, M.A., 2007. *Geostatistics for environmental scientists*. John Wiley & Sons Ltd, Chichester, West Sussex, England.
- WHO, 1998. *Electromagnetic fields and public health: Extremely low frequency (ELF)*. WHO, Geneva, Switzerland.
- Witten, A., 2006. *Handbook of Geophysics and Archaeology*. Equinox Publishing Ltd., London, Great Britain.
- World Reference Base, 1998. *World reference base for soil resources*, World Resources Report vol. 84, FAO, Rome, Italy.

Curriculum vitae

(I) Personal

Name: Timothy Saey
Adress: Brankardierstraat 21
9000 Gent
Date of birth: 01/08/1983
Place of birth: Gent
Nationality: Belgian
Tel.: +32 (0)485 62 54 07
E-mail: Timothy.Saey@UGent.be

(II) Education

2001-2006: BIO-ENGINEER IN LAND- AND FOREST MANAGEMENT, SOIL AND WATER
MANAGEMENT (GHENT UNIVERSITY)

Thesis: 'Influence of water absorbing polymers on the water balance and biomass
production of azalea and grass in substrate and sand'

(III) Professional experience

1 DECEMBER 2006 – 31 JULY 2009: FWO PROJECT (GHENT UNIVERSITY)

- 'Potency of electromagnetic induction for pedological, quaternary-geomorphological and archaeological prospection'
- Researcher involved with the projects:
 - Geophysical prospection: identification of archaeological and landscape-historical traces and metal objects
 - Golf 'Hof ter Hille', Koksijde
 - Rieme-Noord, Port of Ghent

- Scientific congresses: oral presentations
 - 13-18 april 2006: EGU General Assembly, Vienna, Austria: ‘Reconstructing the paleotopography at the beginning of the Weichselian glacial stage using electromagnetic induction.’
 - 26-28 august 2009: Biennial Meeting of Commission 1.5 Pedometrics, Beijing, China: ‘The inversion of simultaneous multiple electrical conductivity measurements to reconstruct the paleolandscape beneath the loess cover.’

1 AUGUST 2009 – 31 APRIL 2010: SCIENCE POPULARISATION PROJECT (GHENT UNIVERSITY)

Interactive excursion for secondary school students. Demonstration of practical applications about soil science and soil sensors, with the aim to convince students about the possibilities and the interdisciplinarity of scientific research.

1 MAY 2010 – ...: GEOPHYSICAL EXPERT (ADEDE)

Conducting GPS-based geophysical surveys with magnetometry, EMI and GPR to locate and identify buried unexploded ordnance.

(IV) Publications

- A1

- De Smedt, P., Van Meirvenne, M., Meerschman, E., Saey, T., Bats, M., Court-Picon, M., De Reu, J., Werbrouck, I., Zwertvaegher, A., Antrop, M., Bourgeois, J., De Maeyer, P., Finke, P.A., Verniers, J., Crombé, P., 20___. Reconstructing palaeochannel morphology with a mobile multi-coil electromagnetic induction sensor. *Geomorphology*, Submitted.
- Saey, T., Lehouck, A., De Smedt, P., Cockx, L., Meerschman, E., Islam, M. M., Meeuws, F., Van Meirvenne, M., 20___. EC-depth modelling with a multi-signal EMI sensor to accentuate archaeological features. *Archaeological Prospection*, Submitted.
- Saey, T., Van Meirvenne, M., Dewilde, M., Wyffels, F., De Smedt, P., Cockx, L., Meerschman, E., Islam, M. M., Meeuws, F., 2011. Combining multiple signals of an electromagnetic induction soil sensor to prospect land for metallic objects. *Near Surface Geophysics*, In Press (DOI: 10.3997/1873-0604.2010070).
- Saey, T., Van Meirvenne, M., De Smedt, P., Cockx, L., Meerschman, E., Islam, M. M., Meeuws, F., 2011. Mapping depth-to-clay using fitted multiple depth response curves of a proximal EMI sensor. *Geoderma*, Published Online (DOI: doi:10.1016/j.geoderma.2011.01.015).
- Simpson, D., Van Meirvenne, M., Lück, E., Rühlmann, J., Saey, T., Bourgeois, J., 2010. Sensitivity of multi-coil frequency domain electromagnetic induction sensors to map soil magnetic susceptibility. *European Journal of Soil Science*, 61: 469-478.
- Cockx, L., Van Meirvenne, M., Vitharana, U.W.A., Verbeke, L.P.C., Simpson, D., Saey, T., Van Coillie, F.M.B., 2009. Extracting topsoil information from EM38DD sensors data using a neural network approach. *Soil Science Society of America Journal*, 73: 1-8.
- Saey, T., Van Meirvenne, M., Vermeersch, H., Ameloot, N., Cockx, L., 2009. A pedotransfer function to evaluate soil profile heterogeneity using proximally sensed apparent electrical conductivity. *Geoderma*, 150: 389-395.
- Saey, T., Simpson, D., Vermeersch, H., Cockx, L., Van Meirvenne, M., 2009. Comparing the EM38DD and DUALEM-21S sensors for depth-to-clay mapping. *Soil Science Society of America Journal*, 73: 1-6.

Simpson, D., Van Meirvenne, M., Saey, T., Vermeersch, H., Bourgeois, J., Lehouck, A., Cockx, L., Vitharana, U.W.A., 2009. Evaluating the multiple coil configurations of the EM38DD and DUALEM-21S sensors to detect archaeological anomalies. *Archaeological Prospection*, 16: 91-102.

Vitharana, U.W.A., Saey, T., Cockx, L., Simpson, D., Vermeersch, H., Van Meirvenne, M., 2008. Upgrading a 1/20000 soil map with an apparent electrical conductivity survey. *Geoderma*, 148: 107-112.

Saey, T., Simpson, D., Vitharana, U., Vermeersch, H., Vermang, J., Van Meirvenne, M., 2008. Reconstructing the paleotopography beneath the loess cover with the aid of an electromagnetic induction sensor. *Catena*, 74: 58-64.

▪ P1

Saey, T., Van Meirvenne, M., Simpson, D., Vitharana, U.W.A., Cockx, L., Vermeersch, H., 2010. Reconstructing the paleotopography at the beginning of the Weichselian glacial stage using an electromagnetic induction sensor. In: R. Viscara-Rossel and A. McBratney (Editors), *Proximal Soil Sensing for High Resolution Soil Mapping*, Chapter 36, 14 p.